Atomistic simulations of Heat-Assisted Magnetic Recording with longitudinal degrees of freedom

David Richard Papp

Doctor of Philosophy

University of York
Physics, Engineering and Technology

September 2024

Abstract

The advent of significantly advancing computational power has brought with it a new challenge to grapple with: the amount of data being circulated, stored, and processed globally is increasing at unprecedented rates. While the demand for data storage has seen a clear rise, advancements to the magnetic recording devices utilised have also improved dramatically over the past few decades. Due to the limitations of conventional magnetic recording hard-disk drives, reducing the size of the magnetic domains used to store information has become a challenge, and is approaching a hard limit. In order to combat this, Heat Assisted Magnetic Recording (HAMR) has shown great promise in overcoming the limitation in grain-size reduction by exploiting the temperature dependent properties of materials such as FePt to approximately quintuple the data storage density by the time HAMR is fully realised. In order to more appropriately research the exact optimisations necessary for HAMR, atomistic models are employed to simulate the recording process while having full control over the inter-atomic interactions governing the process. The theoretical modelling of materials such as FePt has shown inherent complexity regarding the treatment of the Pt atoms, as its inclusion in FePt's magnetisation properties exists as an induced moment, brought on by the Fe exchange field. While the currently used atomistic model of FePt yields expected results, it fails to detail the truly atomistic nature of its behaviour, due to elimination of the Pt degrees of freedom. This thesis introduces the methods necessary to include maximal atomistic degrees of freedom in FePt, and demonstrates the viability of such a model in investigating the less looked at parts of theoretical HAMR, such as modelling the magnetisation of FePt with respect to its inherent disordering.

Table of contents

List of tables **ix**

List of figures **xi**

1 Introduction **1**

1.1 The origins of magnetic recording 1

1.2 Heat assisted magnetic recording 3

1.3 Atomistic modelling strategies 6

1.4 Thesis outline 6

2 Methods **9**

2.1 The atomistic spin Hamiltonian 9

2.1.1 Collective electron spin representation and exchange 10

2.1.2 Anisotropy energy 13

2.1.3 Two-ion anisotropy 15

2.1.4 Applied magnetic fields 15

2.1.5 The Landau expansion and longitudinal dynamics 16

2.2 Atomistic integrator schemes 18

2.2.1 The stochastic Landau-Lifshitz-Gilbert integrator 18

2.2.2 The Heun solver 19

2.2.3 Effective magnetic field 20

2.2.4 The longitudinal Landau-Liftshitz-Gilbert integrator 21

2.2.5 The fourth-order Runge-Kutta solver 24

2.2.6 The Landau-Lifshitz-Bloch integrator 25

2.2.7 The Monte-Carlo integrator 27

2.2.8 The longitudinal Monte-Carlo integrator 27

2.3 Quantifying magnetisation properties 29

2.3.1 System magnetisation 29

2.3.2 Sublattice susceptibility 30
2.4 Summary 31

3 Atomistic simulations on the effects of grain size in HAMR 33
3.1 Background 33
3.2 Theory 35
3.2.1 Atomistic Pt-modified Fe parameters 35
3.2.2 The conventional FePt Hamiltonian 37
3.3 Simulation methods 38
3.3.1 Crystal structure generation 38
3.3.2 Simulation of HAMR media 38
3.4 Results and discussion 40
3.4.1 Verifying the temperature-dependent properties of FePt 40
3.4.2 Magnetic switching of FePt grains 43
3.4.3 Fully atomistic HAMR 48
3.5 Summary 52

4 Longitudinal Spin Fluctuations in atomistic spin models 55
4.1 Motivation 55
4.2 Theory 58
4.2.1 The atomistic spin Hamiltonian 58
4.2.2 Equilibrium correction of Landau coefficients 58
4.3 Simulation methods 62
4.3.1 Temperature-dependent longitudinal dynamics 62
4.3.2 Ultrafast demagnetisation with longitudinal dynamics 63
4.4 Results and discussion 64
4.4.1 Single spin calculations 64
4.4.2 Boltzmann probability distributions 65
4.4.3 Curie and Néel temperature calculations 68
4.4.4 Ultrafast demagnetisation of Ni 71
4.5 Summary 72

5 The role of longitudinal spin fluctuations in FePt 75
5.1 Motivation 75
5.2 Longitudinal dynamics in FePt 76
5.2.1 The conventional FePt model 76
5.2.2 The FePt Landau Hamiltonian 78

5.2.3 Simulation methods 80
5.3 Néel anisotropy model 82
5.3.1 The Néel anisotropy model for FePt 82
5.3.2 Fourth-order Néel anisotropy 83
5.4 Results and discussion 85
5.4.1 Disorder-dependent FePt anisotropy 85
5.4.2 Induced Pt moment behaviour in FePt 90
5.5 Summary 92

6 Atomistic simulations of HAMR including Longitudinal Spin Fluctuations 93
6.1 Motivation 93
6.2 Single grain anisotropy energies 94
6.3 Longitudinal fluctuations in magnetic switching 96
6.4 Easy-axis dispersion in disordered grains 97
6.5 Atomistic HAMR with Pt degrees of freedom 98
6.6 Summary 103

7 Conclusions 105
7.1 Further work 107
7.1.1 Split sampling scheme in the longitudinal Monte-Carlo 107
7.1.2 Modelling further induced moments longitudinally 108
7.1.3 Composition dependent behaviour of HAMR systems 108
7.1.4 Atomistic LSF-LLB 108

References 111

List of tables

3.1 Summary of data obtained for all simulated grain sizes for K against T simulations. A distinct size dependency can be observed in the Curie temperature results obtained, which follows expected behaviour. 43

4.1 The collective simulation parameters utilised in this chapter for the materials examined. The Landau coefficients were obtained outside the scope of this thesis using methods from Pan *et al* [31]. The rest of the simulation parameters follows what was obtained in Evans *et al* [28]. 59
4.2 The temperature-dependent calculations of the tested materials, drawing a comparison between the LSF and conventional integrator schemes. F_α also shows the necessary exchange coupling adjustment applied to each system. It can be seen that good experimental agreement is obtained with this adjustment [103, 104]. 69

5.1 Summary of FePt parameters used in the LSF calculations [50, 107]. 78
5.2 Summary of anisotropy parameters used for LSF FePt simulations. 85

List of figures

1.1 A schematic representation of longitudinal versus perpendicular recording technologies. It is evident that in the perpendicular state, a more concentrated amount of bits can be utilised, leading to a larger data storage density. The soft magnetic underlayer amplifies the magnetic field via the creation of a return flux path. 2
1.2 A summarised description of the three factors competing in the magnetic recording trilemma. While it is not possible to nullify the effects from either aspect, certain grain configurations minimise their effects to a tolerable limit. 4
1.3 ASTC/ASRC defined future trends for magnetic recording technologies, showing a clear trend towards developments of thermally variable recording architectures. Source: excerpt from [20]. 5

2.1 Ferromagnetic, antiferromagnetic, and paramagnetic spin configurations. The ferromagnetic case causes parallel alignment due to $J_{ij}^{\text{1-nn}} > 0$, the antiferromagnetic case causes opposing exchange between spin sites to nullify the effective field by having $J_{ij}^{\text{1-nn}} < 0$. Finally, the paramagnetic state shows no preferential alignment direction, and thus are fully randomly oriented. 13
2.2 The LLG integrator broken down into different components, (a), (b) showing undamped precession, (c), (d) showing the effects of the damping term, and (e), (f) showing the application of stochastic thermal noise. 22
2.3 The schematic differences between the conventional transverse-only relaxation of a spin in (a) compared to the longitudinal variant in (b). The longitudinal LLG enables longitudinal degrees of freedom as well as transverse as it removes the constraint of the unit sphere. 24

2.4 An example comparison of the convergence behaviour between the (a) Heun and (b) fourth-order Runge-Kutta (RK4) solvers. The RK4's final gradient (light-blue) is calculated via an averaging of all four gradients. It is clear that the RK4 converges to its result with even larger timestep sizes, though the Heun scheme has shown effectiveness in all calculations done in this thesis. 26
2.5 Schematic diagram of allowing split Monte-Carlo moves in the LSF-MC integrator scheme. The separation of transverse and longitudinal motion would allow for independent control over both sampling functions. 29

3.1 The structure of $L1_0$ FePt consists of exclusive layers of Fe and Pt, with a high uniaxial anisotropy preferring the stacking direction. 34
3.2 (a) shows the purely visual construction of the $L1_0$ FePt unit cell, where Pt (orange) is later stripped in (b) as only Fe (blue) degrees of freedom are being considered. Additionally, the logic behind the exchange list can be seen to include Fe-Fe interactions, including for spins in neighbouring cells, via J_x, J_y, and J_z. 39
3.3 The final product of an atomistically generated grain consisting of $L1_0$ FePt. Each dot rendered corresponds to an individual atoms with its own spin degrees of freedom. 39
3.4 An example of grains generated using Voronoi tessellation used for simulating HAMR atomistically. It can be seen that the random generation creates a size variance between different grains. 40
3.5 Normalised Magnetisation against temperature curve for $L1_0$ FePt. The calculated fit using equation 3.16 gives a value of $T_C = 704.8$ K, with $L \approx 2.1$. The temperature-dependent anisotropy demonstrated is a key property of being able to use FePt for HAMR. 42
3.6 Magnetisation against time data showing unstable magnetic switching. A render was generated at 350 ps seen next to the plot showing a domain wall process, which affected the way in which magnetic switching takes place. The domain wall described occurs at the $t = 420$ ps mark, and is distinctly identified by the light area towards the middle section of the grain which is at the boundary of the blue (spins with changed magnetisation) and brown (spins with their original magnetisation). This is for a grain of size 5 nm in diameter and 10 nm in height. 45

3.7 Simulation data for a grain of 5 nm diameter and 5 nm height undergoing switching due to a thermal pulse and an applied field of 1 T. The size of the system is small enough for the thermal pulse to overcome the ordered spin state, and thus their direction reverses with the application of the field. . . . 46

3.8 Single grain ($D_{\text{grain}} = 12$ nm, $H_{\text{grain}} = 10$ nm) switching whereby the size of the system is too large for the thermal field to overcome the ordered state of the spins, and then to reverse their direction with the applied field. 47

3.9 Magnetisation against time data for grains with fixed height 5 nm, and variable diameter (labelled). It can be seen that increasing the grain size from (a) to (e) shows gradual difficulty in the ability to switch. 49

3.10 The magnetisation against time data for 10 nm height grains, and increasing diameters from (a) to (e) as labelled. It is evident that the drastically larger aspect ratio of the grains compared to the 5 nm height variant leads to the rapidly deteriorating ability to switch. 50

3.11 A render of all the full HAMR systems simulated atomistically, which consist of 3 nm to 8 nm diameter grains with a fixed height at 5 nm. The blue grains have undergone magnetic switching whereas gold grains have remained in their original magnetic state. 51

4.1 The longitudinal energy surfaces for Fe, Ni, Co, and Cr which depend on the configuration of the Landau Hamiltonian coefficients. (a) shows the purely longitudinal energy components, while (b) includes the effects of exchange energy. 60

4.2 Figures (a), (c), (e), and (g) show the material specific longitudinal energy surfaces with the temperature effects of exchange included, and (b), (d), (f), and (h) are the respective first derivatives of the total Hamiltonian with respect to $|S|$. The exchange contribution at each temperature was extracted via bulk calculations, and then analytically plotted using the total LSF Hamiltonian. 61

4.3 (a) single spin LLG dynamics, and the error between analytical and calculated results in (b). (c) shows the 0K dynamics for the LLG compared to the LSF-LLG and LSF-LLG-RK4 schemes, while (d) is the 0.1K case. It can be seen that both Heun and RK4 solvers converge to the same result appropriately. . 65

4.4 Ni longitudinal Boltzmann distribution without (a) and with (b) exchange energy included in the total Hamiltonian. It can be seen that there is a reduction in the broadening of the distribution given an exchange field, indicating a strongly polarised moment. The simulated points were fitted via equation 4.10. 66

4.5 Without the inclusion of exchange energy, the longitudinal Boltzmann distributions are shown for Fe (a), Ni (b), Co (c), and Cr (d). The width of the distributions clearly increase with larger temperatures, allowing for a larger number of unexplored longitudinal states to manifest. 67

4.6 The temperature-dependent magnetisation properties of Fe (a), Ni (b), Co (c), and Cr (d). "MC" (dark-blue) corresponds to the Monte-Carlo integrator, "LSF-MC" (light-blue and gold) corresponds to the longitudinal Monte-Carlo integrator. The "LSF-MC $|S|$" label denotes the calculated spin-length using the longitudinal Monte-Carlo. It is clear that there is a consistent underestimation of T_{C} and T_{N} given the LSF model, which leads to the conclusion that an exchange coupling adjustment is mandatory. 68

4.7 The temperature-dependent magnetisation of Ni changes drastically given the introduction of a temperature-dependent exchange adjustment. It can be seen that the appropriate T_{C} is reproduced with a necessary rescaling of the exchange coupling constant J. 70

4.8 The ultrafast demagnetisation of Ni is calculated with both the LLG and LSF-LLG integrator schemes, yielding similar results. It should be noted however that the longitudinal contributions of Ni leads to a difference between the two results. It can be seen that there is good experimental agreement. 71

5.1 A schematic representation of the LSF atomistic modelling scheme governing FePt, with the primary advantage of being able to include Pt degrees of freedom alongside Fe ones. In previous models the Pt sites were not given their own degrees of freedom according to the Fe exchange field. 77

5.2 Energy against spin length relationship for FePt. It can be seen that Fe is prominently centred around $|S| = 1$, whereas Pt starts at $|S| = 0$ without the addition of the effects of exchange. This approximation is attributed to Pt not having a magnetic moment in bulk, while Fe does. 79

5.3 The effects of the Fe exchange field on the Pt sites, shifting the energy minima going from $|S| = 0$ to $|S| = 1$. At equilibrium, the Pt longitudinal energy surface is parametrised such that the Fe exchange field gives it exactly $|S| = 1$ at $T = 0$ K. 80

5.4 Disordering can be introduced by including a probability of incorrectly swapping atomistic sites for the opposite species. 81

5.5 Comparison between second (a), (c) and fourth order (b), (d) Néel forms, showing clearly that in order to extract the cubic symmetries in disordered FePt, a fourth order Néel term must be employed, as the asymmetric second-order result does not reflect cubic symmetries appropriately. 84

5.6 Schematic of spherical polar coordinate system employed in computing spin vectors given the azimuthal and in-plane rotational angles. 85

5.7 (a), (c) Anisotropy energy varying with the azimuthal angle for an onsite anisotropy energy model. The maximal difference between the energy states was used as a reference to obtain the Néel pair anisotropy values for both Fe and Pt in (b), (d). 86

5.8 A schematic diagram showing the Néel pair bond loss process that occurs when FePt goes from an ordered to a fully disordered state. As the system tends towards a disordered lattice, the average number of spin pairs that can be described drops from $n_{\text{Néel}} = 8$ to approximately $n_{\text{Néel}} = 6$. 87

5.9 Anisotropy symmetries pertaining to the fully ordered ($L1_0$) (a), (c), (e) and fully disordered (A1) (b), (d), (f) phases of FePt. The existence of a cubic phase is realised in the disordered system and is otherwise absent in the ordered one. It should be noted that in order to extract the correct symmetries, the fourth-order Néel pair model was used for the A1 system. 88

5.10 The difference between the anisotropy energies of spin directions [001] and [100] against chemical ordering parameter s, showing clearly that increasing disordering leads to a significant penalty in uniaxial alignment. The data points calculated are in agreement with low temperature (LT) experimental data from Okamoto *et al* [32]. The room temperature calculations were collated in Wolloch *et al* [111]. 89

5.11 temperature-dependent magnetisation calculation via fully discretized atomistic dynamics of Fe and Pt moments. It can be seen that both Fe and Pt sublattices exactly overlap with regard to their temperature-dependent magnetisation values in (a), due to a compensatory increase of the Pt $|S|$ seen in (b). 91

5.12 Boltzmann distributions of Fe (a) and Pt (b) longitudinal energy states with respect to temperature. The stronger Fe moment is shown to have a much smaller distribution width, whereas Pt demonstrates drastic changes in $|S|$ as it is considered to be more easily polarised. 91

6.1 Uniaxial anisotropy energy with respect to chemical ordering parameter s varied by grain dimensions. E_{ani} was computed as the difference between the anisotropy energies when all spins are parallel and perpendicular to the easy-axis. There is good agreement between the different system sizes. . . . 95

6.2 A demonstration of the spin length changes undergone by Pt sites for a grain with $D_{\text{grain}} = 5$ nm and $H_{\text{grain}} = 5$ nm. The grains are simulated in a 300K environment, which increases via a Gaussian function to a peak of 700 K at 300 ps. The ability to switch efficiently is impacted with respect to increased disordering, as the Néel pair anisotropy interactions are reduced as disorder increases, leading to smaller uniaxial contributions at the peak temperature. 97

6.3 The easy axis distributions are shown for fixed grain size $D_{\text{grain}} = 6$ nm and $H_{\text{grain}} = 5$ nm on a magnetic recording medium. The chemical order parameter s shows the simulated level of disordering present in the grains. It can be seen that at values of $s > 0.5$, a 5° tolerance from the z-axis can be obtained, while with $s < 0.5$, the easy axis dispersion quickly diverges to $\theta = 90°$. 99

6.4 A render showing the HAMR process for grains of fixed height 5 nm, with diameter varied from 3 nm in (b) to 8 nm in (g) in 1 nm increments. The magnetic recording trilemma is represented in these calculations, showing a clear trade-off between grain size and overall error in the definition of bits. . 101

6.5 Rendered bit pattern that is imprinted on HAMR media, with fixed grain dimensions of $D_{\text{grain}} = 6$ nm and $H_{\text{grain}} = 5$ nm. Inherent disordering is also added to the system at $s = 1.0$ in (b), $s = 0.9$ in (c), $s = 0.8$ in (d), and $s = 0.7$ in (e). It can be seen that even $s = 0.9$ creates a drastic reduction in the clarity of the bits due to a smaller energy barrier required to switch their magnetisation direction. This means that random thermal fluctuations can more easily induce unwanted reversal, leading to backswitching. 102

6.6 A close up render of HAMR system with $s = 1.0$ in (a) and $s = 0.7$ in (b). The disordered grain systems create an environment which more easily accommodates for oppositely aligned spin sites, leading to more spontaneous magnetisation reversal, which significantly effects the reliability of the imprinted data being read. 103

Acknowledgements

I would like to show great appreciation to my supervisors Richard Evans and Roy Chantrell for their tireless support throughout this PhD journey. I have learnt a lot from their guidance over this time, and developed experiences, skills, and opportunities under their mentorship that will last me a lifetime. To my colleagues within the Computational Magnetism Group, Jack, Jackson, Carenza, I cherish the memorable interactions we shared as part of our wider dedication to research. Additionally, your support has meant a lot to me, and being able to discuss my work with you was significantly impactful to my research. I am also similarly grateful to Matt, Lars, Lulu, Andrea, Verena, Tim, and Oscar, who frequently provided fruitful scientific discussions.

I gratefully acknowledge Ewan, Ganping, Pin-Wei, and Wei-Heng during my time at Seagate for being more than just excellent scientists, but also for giving me guidance around research in the industry, and for the eye-opening experiences I had while there. Additionally, my thanks goes to the Advanced Storage Research Consortium (ASRC) for funding this project, and the VIKING cluster for providing the high-performance compute necessary to accomplish my research.

I wish to extend my heartfelt gratitude to friends outside of my research group, Patrick, Tim, Benji, Sean, Alex, and Josh, and countless others for being there all this time. I owe my thanks to the Taekwondo society and everyone I met there during my PhD. Eli and Elena, thank you for being stellar training partners and mentors.

I owe immense gratitude to my family, especially my parents George and Ilona, and my brother Erik. Without your support and patience this would not have been possible. Additionally, I wish to extend my sincere acknowledgement to William, and Claire, thank you for believing in me all this time, and for your help throughout this journey.

Declaration

I hereby declare that except where specific reference is made to the work of others, the contents of this thesis are original and have not been submitted in whole or in part for consideration for any other degree or qualification in this, or any other university. The majority of this thesis has been presented at various conferences by the author, some chapters being based on the following publications:

- D. R. Papp, R. F. L. Evans and R. Chantrell, "Atomistic simulations on the effects of grain size in HAMR," 2023 IEEE International Magnetic Conference - Short Papers (INTERMAG Short Papers), Sendai, Japan, 2023, pp. 1-2.
- D. R. Papp, L. Bergqvist, M. O. A. Ellis, R. Chantrell and R. F. L. Evans, "Longitudinal spin fluctuations in atomistic spin models," (manuscript in final revision, planned submission to Physical Review B.)

1

Introduction

1.1 The origins of magnetic recording

Magnetic recording is the process of storing data via harnessing magnetism in magnetic materials. This usually manifests through the utilisation of technologies that allow to imprint a set of magnetically aligned elements which translate to computational information when read back. The first example of this was by Valdemar Poulsen in 1898, more than 100 years ago [1]. The idea behind this invention was a wire that had localised magnetic regions imprinted by the electric signals produced via a telephone call. An evolution of the idea by Fritz Pfleumer in 1928 allowed for the invention of a device known as the tape recorder, specifically ones that utilised a non-magnetic tape coated in single-domain ferric oxide particles that were able to take on the magnetisation of a desired recording pattern [2]. At this point, considerations for the areal density (data stored per unit area) achievable in these devices started to gain traction, when in 1956, IBM announced the move to a magnetic recording disk storage architecture, which was used in a commercial product at the time for data storage and retrieval in computational environments [3]. The particles used in Hard-Disk Drives (HDDs) were still of a single domain nature, and composed of ferric oxide. Upon further industry-wide demand increases and need for better solutions, HDD magnetic recording technology quickly took off as a viable solution to enterprise-scale need for data storage mechanisms [4]. This follows closely with what is known as Moore's law, which defines that in a general case, the amount of transistors and resistors on computational microchips doubles every 2 years [5]. In more recent terms, it is quantified that the estimated data generated per year is 175 ZB, whereas this was 33 ZB in 2018 [6]. This is prompted by significant technological advancement in the space of larger data formats being used, more accessibility to these data formats, and an overall trend showing that companies are migrating to cloud (server) based data-storage solutions [7, 8].

The fundamental principles behind conventional magnetic recording technologies utilised in HDDs involves a hard disk, the medium upon which data is stored magnetically, which allows for data to be imprinted and read by a magnetic recording head. This style of magnetic recording allowed for a convenient read and write process, as the anisotropic magnetisation of the particles on the media would allow for reorientation via a locally produced magnetic field. From an efficiency standpoint, being able to "override" the magnetic state of the small magnetic regions allowed for less error, as the previous magnetic state does not have to be erased beforehand. Regions on the hard disk are imprinted with a magnetisation direction, which would determine whether a "1" bit, or a "0" bit is recovered from the read signal. The first iterations of HDD technology utilised an architecture known as longitudinal recording, whereby the magnetic regions were aligned in plane to the disk, producing a "left" or a "right" magnetic field to denote the two bit types [9]. This form of recording was later revised, and the currently used iteration of HDD technology utilises an architecture known as perpendicular magnetic recording (PMR). PMR was able to increase the areal density via the adjustment that the magnetic regions responsible for storing bit sequences were placed perpendicular to the plane of the disk, and thus by measuring "up" and "down" magnetic fields, more bits could be placed onto the same area. Figure 1.1 illustrates the differences between longitudinal recording and PMR [10, 11].

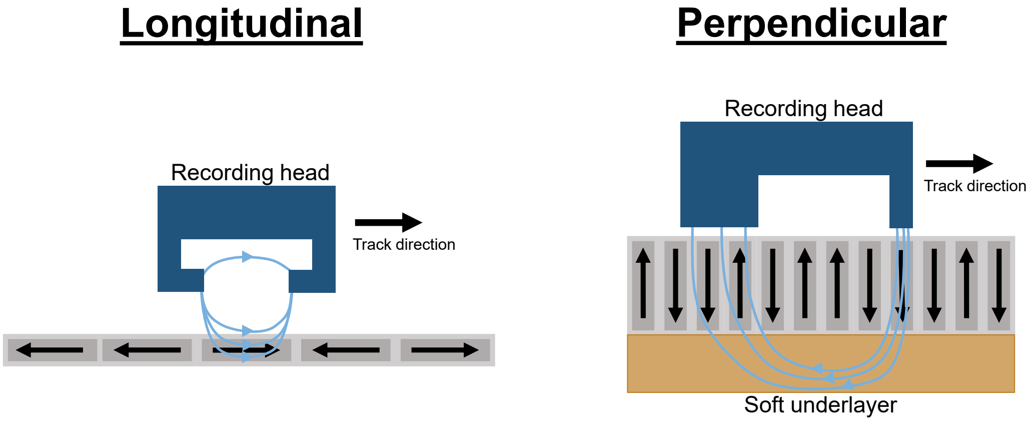

Fig. 1.1 A schematic representation of longitudinal versus perpendicular recording technologies. It is evident that in the perpendicular state, a more concentrated amount of bits can be utilised, leading to a larger data storage density. The soft magnetic underlayer amplifies the magnetic field via the creation of a return flux path.

The PMR architecture introduces a soft underlayer material below the layer containing the recording data. This is to ensure that the write field produced is able to more easily focus on precise regions (given they are now of a smaller size), and to minimise the stray field produced. An additional constraint introduced in PMR is that the grains have to contain mechanisms to prevent exchange with each other in-plane if their anisotropy field is not high enough. Minimising the exchange coupling between grains is necessary to prevent accidental clustering of multi-grain domains [12].

In order to achieve larger areal densities, the grains (small cylindrical magnetic particles forming PMR media) had to be reduced in diameter to be able to accommodate a larger density. This is limited by the following competing forces: smaller grains are susceptible to erroneous switching due to thermal fluctuations, thus require highly anisotropic behaviour to overcome detrimental thermal effects. This is quantified as KV, which refers to the anisotropy density K with relation to grain volume V. With comparison to temperature T, the relationship $KV \approx 40k_{\mathrm{B}}T$ must hold, otherwise the system is error prone to thermal effects [13]. This has an effect on the choice of recording head field strength, as now the write field has to overcome the anisotropy energy [14]. The collection of these three competing forces acting against each other illustrated in figure 1.2 and is referred to as the magnetic recording trilemma [13, 15].

In order to combat the readily approaching limits to conventional magnetic recording, research on Heat Assisted Magnetic Recording (HAMR) has had great success to further push areal density limits [16]. The introduction of thermal effects introduces another component to the conventional magnetic recording trilemma, which results in the magnetic recording quadrilemma. This is introduced in more detail in chapter 3.

1.2 Heat assisted magnetic recording

Heat Assisted Magnetic Recording (HAMR) writing process occurs by modifying the original recording head to include a near-field transducer (commonly with a Gold heating element), which applies a persistent thermal field to local grains [17]. HAMR commonly utilises FePt grains for its temperature-dependent anisotropy properties, which can be exploited by the near-field transducer. The persistent thermal field heats up the materials underneath it with the goal of reaching $T_{\mathrm{grain}} = T_{\mathrm{C}}$, at which point, the paramagnetic state of the grains makes overcoming their otherwise strong anisotropy field much easier. As the grain cools, the data remains stable in even smaller grains, as the anisotropy K of room-temperature FePt keeps the magnetisation stable beyond thermal effects [16, 18]. With advancements on HAMR, it is projected that the current areal density of $1\ \mathrm{Tb/in^2}$ is able to increase to $4\ \mathrm{Tb/in^2}$ using grain diameters of $D_{\mathrm{grain}} \approx 5$ nm with HAMR-based architecture [19]. Figure 1.3 describes the Advanced Storage Technology Consortium's projections for the implementation of HAMR as a timescale.

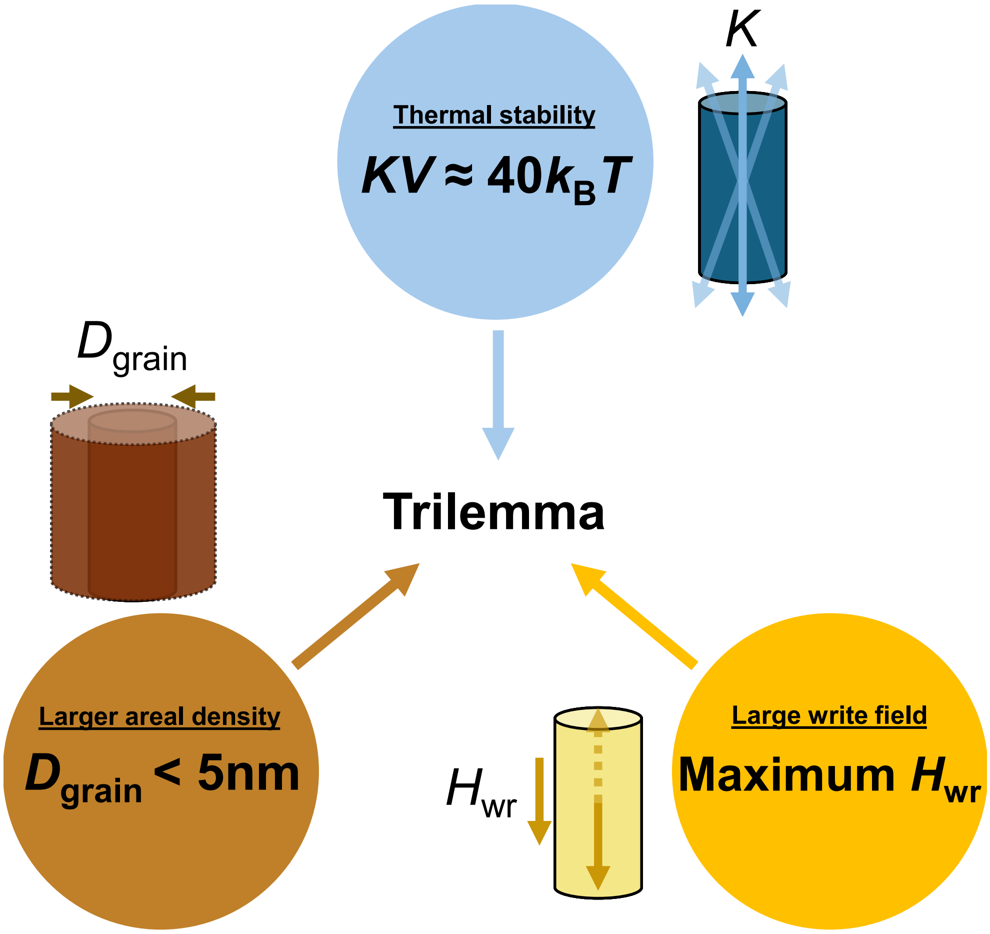

Fig. 1.2 A summarised description of the three factors competing in the magnetic recording trilemma. While it is not possible to nullify the effects from either aspect, certain grain configurations minimise their effects to a tolerable limit.

A constraint that is introduced via the thermal mechanisms of HAMR is that in practice, manufacturing recording media will introduce a variance in grain size and volume, thus creating a variance in T_C and $K(T)$ in the case of FePt [21]. This is a challenge, because if the same global temperature affects all grains in the same way, in some cases if $T_{grain} >> T_C$, the additional temperature-dependent disordering introduced causes a reduction in anisotropy, which reduces the probability for switching into the recording field direction [22, 23]. Additionally, it is expected that some clusters of disordered FePt (in the A1 phase) will form naturally as a result of the recording media manufacturing process, which will cause deviations in the natural easy-axis of the anisotropy [24]. Deviations in the natural easy-axis of grains causes the grain anisotropy fields to contribute an unexpected in-plane component, which can have consequences to the expected grain field direction when the reading process takes place.

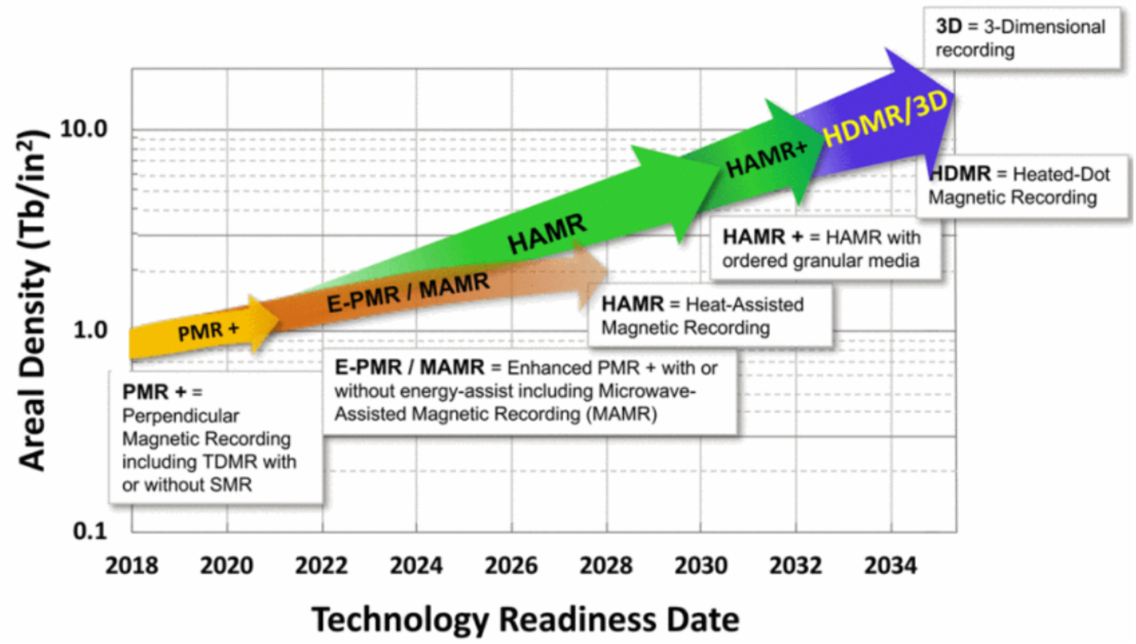

Fig. 1.3 ASTC/ASRC defined future trends for magnetic recording technologies, showing a clear trend towards developments of thermally variable recording architectures. Source: excerpt from [20].

As a means of researching and further developing the understanding of how to best achieve maximal areal density, theoretical computational models are often employed to simulate HAMR [25–27]. Due to the nanoscale complexities that arise in such technologies, atomistic modelling can be utilised as a form of discretising the HAMR process into individual atoms, and computing the necessary interactions between them. Such atomistic modelling strategies can be used to build full-scale simulations of the recording process, whereby the nanoscale physics can more easily be calculated and understood. This thesis works towards building a more locally-dependent atomistic model of HAMR, such that the physical effects arising from even minute differences in crystal structure can be accounted for and calculated. This brings the advantage of having fine control over determining properties of explicitly positioned atoms, with significantly less overhead assumptions and averaging. Atomistic modelling also brings an inherent advantage via its ability to more precisely customise the exact position of each atom with relation to the bulk system. This means that modelling effects such as disordering and alloying configurations are much more accessible, which is a crucial component of understanding the nanoscale physics of magnetic materials.

1.3 Atomistic modelling strategies

Atomistic modelling of magnetic materials is the strategy of calculating magnetic properties via the evolution of spin degrees of freedom in a system under various conditions such as variations in crystal structure, variations in temperature, or the influence of applied fields. The nature of atomistic modelling relies on the assumption that the collective spin behaviour of electrons can be approximately localised to each atomistic site in a crystal structure, and via computing the interaction properties between the atoms, a system will naturally fall into a favourable state due to correlation between the direction of the spins. By decomposing a system into its atoms as the smallest building block, parallelised computational routines can be developed that distributes the computation of spins as efficiently as possible, allowing for massively scalable architectures [28, 29]. The scalability of the frameworks used is pivotal in being able to run simulations that are larger in size and complexity to better emulate the macroscopic effects of magnetic systems via a set of atomistic interactions.

1.4 Thesis outline

The realisation of Heat Assisted Magnetic Recording (HAMR) has garnered interest in furthering its maximal potential, however in order to fully grasp the nanoscale nature of the physics underpinning the interactions that govern it, this thesis aims to enhance the currently employed methods of atomistic modelling, and to deepen physical understanding of the magnetisation dynamics that take place via the Longitudinal Spin Fluctuations (LSF) model. The development of such a model was crucial in extracting truly atomistic detail from a commonly used material for HAMR: FePt, which has posed challenges in its simulation due to the induced moment nature of the Pt sites. The level of additional detail provided by the LSF model has allowed for full-scale atomistic simulations of HAMR with all atomistic degrees of freedom, which can be used to model previously approximated factors such as Pt moment growth, inherent disordering, or the introduction of a disordered phase in the magnetic recording medium. The results of this thesis unlocks new ways to investigate stoichiometric variations in HAMR recording media, which makes the process of developing prototype HAMR technologies easier, with the aim to push the areal density limits.

Chapter 2 details the key derivations that were used in the atomistic modelling techniques used in this thesis. A description of the Heisenberg Hamiltonian is shown, with the origins of the exchange coupling interaction between spin sites which ultimately govern the correlation between the spins in a magnetic system. Additionally, the generalised anisotropy energy forms are discussed, in both uniaxial and cubic forms. The two-ion tensorial form of anisotropy is discussed, which is introduced in the context of FePt as per Mryasov *et al* [30]. The Landau expansion is highlighted, which is the basis for informing the Longitudinal Spin Fluctuations (LSF) models that are utilised in this thesis to model moment size changes via the energies determined by the material-specific Landau Hamiltonian. The integrator schemes necessary to compute longitudinal behaviour are introduced and discussed, which come in Landau-Lifshitz-Gilbert (LLG) and Monte-Carlo (MC) forms. The relation of the longitudinal integrators are highlighted against the Landau-Lifshitz-Bloch (LLB) equation of motion, which can be used to derive the LSF-LLG integrator scheme.

Chapter 3 shows the derivation and usage of the conventional FePt model, which uses the aggregate effect of the Pt as a modification to the Fe moments, which are ultimately the only degrees of freedom modelled in this formalism. Calculations were done to show the temperature-dependent behaviour of the implemented FePt model, which replicated what is expected through the experimentally measured Curie temperature and anisotropy scaling laws. Calculations are shown for the HAMR single-grain switching process of $L1_0$ FePt grains, and the consequences that different system dimensions has on switching viability. Fully atomistic HAMR was also done as a calculation with this model, showing the atomistically-determined process of magnetic recording by exploiting the variable anisotropy present in FePt systems.

Chapter 4 focuses on the initial implementation of the LSF model, where tests are done on four common magnets Fe, Ni, Co, and Cr. The Landau coefficients for the four materials were computed (acknowledgements to Lars Bergqvist) using DFT methods detailed in Pan *et al.* which allowed for appropriate moment size changes to be modelled as a dynamic parameter [31]. A justification to the adjustments made to the coefficients is also discussed, so as to satisfy the equilibrium condition of spin length quantity $|S| = 1$ at $T = 0$ K. Further to this, the implementation of the longitudinal LLG (LSF-LLG) integrator scheme is validated via the use of the Heun and the notably more accurate fourth-order Runge Kutta (RK4) solver. For the longitudinal Monte-Carlo (LSF-MC) integrator scheme, it is shown that the longitudinal Boltzmann distributions recover the exact behaviour that was described by the Landau Hamiltonian, validating the approach to using a combination of transverse and longitudinal sampling spaces. The temperature-dependent magnetisation results are highlighted, with the dependence of $|S|$ with respect to T as a contributing factor to each system's normalised magnetisation. As a means of testing the dynamics of the LSF model, a Ni system was subjected to an ultrafast laser pulse causing demagnetisation, showing excellent agreement with experimental data.

Chapter 5 builds on the implementations introduced in chapters 3 and 4 by implementing a longitudinally-dependent FePt model, which allows for the full discretisation of Pt spins. By allowing moment size changes of the Pt spins, the induced behaviour via the Fe exchange field can be computed, and thus Pt degrees of freedom are included in the magnetisation dynamics of FePt. Additionally, the conventional anisotropy model for FePt was reworked to include local stoichiometric variation by utilising the Néel pair anisotropy of second and fourth-order expansions. The variation of FePt's uniaxial easy-axis anisotropy is shown to follow the relationship measured by Okamoto *et al.* while the exact cubic symmetries are recovered at the fully disordered A1 phase [32]. The newly reworked magnetisation properties of FePt are demonstrated using the LSF model, showing the exact qualitative behaviour that Pt gains an induced moment as a result of the Fe exchange field. This was shown via system magnetisation against temperature calculations, along with the Fe and Pt longitudinal Boltzmann distributions.

Chapter 6 collates the newly-localised LSF FePt model, and places it into the context of full-scale HAMR simulations. Using the extra detail obtained allows for calculations of anisotropy symmetries of grain structures with varying levels of disordering, which were shown to scale as expected: increasing disordering leads to a clear reduction in uniaxial anisotropy. Switching dynamics are shown for FePt grains with varying levels of disorder, and it is demonstrated that the extra stoichiometric variation leads to inefficiencies in the switching process. The single-grain structures were collected into fully atomistic models of magnetic recording media, where HAMR simulations were conducted once again, this time with full degrees of freedom in FePt. Additionally, the effects of disordering on the efficiency of writing bit sequences is shown to significantly deteriorate the quality of the data written. Finally, calculations were done to determine the easy-axis relaxation profiles of grains on a magnetic recording medium with varying levels of disorder.

Chapter 7 highlights the key results obtained, from which conclusions are drawn. This also includes any potential shortcomings or future improvements that could be implemented to continue the research presented in this thesis.

2

Methods

2.1 The atomistic spin Hamiltonian

The atomistic spin Hamiltonian describes the total energies of a system via an averaged description of their collective behaviour, attributed mainly to a configuration of outer-shell electrons. A pivotal assumption is that their total spin contributions can be localised to each site in a lattice environment. In magnetic systems, this leads to modelling spin systems down to atomistic discretisation by defining a Heisenberg Hamiltonian that calculates the dependence of each spin site with another neighbour via spin vector $\mathbf{S}$. This represents a vector defining the three-dimensional components of spin where $|S| = 1$ classically, however in this thesis methods are introduced to remove this constraint on $|S|$. Resulting from this is that each spin site carries with it a net local magnetic moment μ_s based on its singly filled outer shell, meaning that in most cases this applies to d and f block elements [33]. It is well established that the moment size of an atomistic site is able to change in magnitude in various circumstances such as scaling with temperature, or inducing moments via alloying [34–36]. This leads to natural questions regarding implementing this into a spin Hamiltonian framework, while still maintaining the underlying computational assumptions of full moment locality.

This chapter investigates the framework of the atomistic Hamiltonian used to simulate magnetic materials in the conventional sense, along with a section on the longitudinally-augmented Hamiltonian. The computational implementation of this work was done in VAMPIRE, which is an open-source C++ based software package for simulating magnetic nanostructures [28, 37].

2.1.1 Collective electron spin representation and exchange

The exchange interaction arises from overlapping electron orbitals, and changes the expectation value of the position of electrons dependent on neighbouring electron wavefunctions. In order to define the exchange interaction, an example shown in [38] is utilised, whereby exchange is proven for two electrons at different positions $\mathbf{r}_1$ and $\mathbf{r}_2$. The incorporation of spin in this formalism is shown afterwards.

The joint wavefunction of two electrons in different states a and b is defined as $\psi_a(\mathbf{r}_1)\psi_b(\mathbf{r}_2)$. Exchange symmetry is disobeyed given such a definition, because the resultant particle exchange would lead to $\psi_a(\mathbf{r}_2)\psi_b(\mathbf{r}_1)$, a result which is not a multiple of the initially defined wavefunctions $\psi_a(\mathbf{r}_1)$ and $\psi_b(\mathbf{r}_2)$. In order to obey symmetry or antisymmetry in the electron wavefunction product states, one of the following equations must hold true (showing symmetric and antisymmetric products respectively):

$$\Psi(\mathbf{r}_1,\mathbf{r}_2) = \Psi(\mathbf{r}_2,\mathbf{r}_1), \tag{2.1}$$

$$\Psi(\mathbf{r}_1,\mathbf{r}_2) = -\Psi(\mathbf{r}_2,\mathbf{r}_1). \tag{2.2}$$

The Pauli exclusion principle states that no identical electron can occupy the same quantum state simultaneously. By expanding equations 2.1 and 2.2, the following is obtained:

$$\Psi_{\text{sym}}(\mathbf{r}_1,\mathbf{r}_2) = \frac{1}{\sqrt{2}}\left[\psi_a(\mathbf{r}_1)\psi_b(\mathbf{r}_2) + \psi_a(\mathbf{r}_2)\psi_b(\mathbf{r}_1)\right], \tag{2.3}$$

$$\Psi_{\text{asym}}(\mathbf{r}_1,\mathbf{r}_2) = \frac{1}{\sqrt{2}}\left[\psi_a(\mathbf{r}_1)\psi_b(\mathbf{r}_2) - \psi_a(\mathbf{r}_2)\psi_b(\mathbf{r}_1)\right]. \tag{2.4}$$

The resultant equation where two identical electron wavefunctions are defined (Ψ_{sym}) can be eliminated, as it requires an electron with position $\mathbf{r}_1$ to be in states ψ_a and ψ_b simultaneously, which is prohibited by the Pauli exclusion principle. Hence, the only possibility is Ψ_{asym}.

The Heitler-London Approximation establishes a calculation for the total energy of this two-electron system via a combination of their individual wavefunctions. This is given by

$$E_{\text{total}} = \iint \Psi^*(\mathbf{r}_1,\mathbf{r}_2)\mathscr{H}_{\text{total}}\Psi(\mathbf{r}_1,\mathbf{r}_2)\,\delta\mathbf{r}_1\,\delta\mathbf{r}_2, \tag{2.5}$$

where in this case, the Hamiltonian $\mathscr{H}_{\text{total}}$ can be decomposed into the contributions shown in the following:

$$\mathscr{H}_{\text{total}} = \mathscr{H}_1 + \mathscr{H}_2 + \mathscr{H}_{1,2}, \tag{2.6}$$

where $\mathscr{H}_1$ represents contributions for the position $\mathbf{r}_1$, $\mathscr{H}_2$ for position $\mathbf{r}_2$, and $\mathscr{H}_{1,2}$ for both positions $\mathbf{r}_1$ and $\mathbf{r}_2$, which is the effective interaction energy between the two electrons. The remainder of this derivation concerns the use of the Hamiltonian $\mathscr{H}_{1,2}$ (given interacting electrons), which can be broken into two contributions shown in the following, representing the classical Coulomb interaction and the quantum mechanical exchange interaction respectively:

$$E_{\text{Coulomb}} = \iint \psi_a^*(\mathbf{r}_1)\psi_b^*(\mathbf{r}_2)\mathscr{H}_{1,2}\psi_a(\mathbf{r}_1)\psi_b(\mathbf{r}_2), \tag{2.7}$$

$$E_{\text{exchange}} = \iint \psi_a^*(\mathbf{r}_1)\psi_b^*(\mathbf{r}_2)\mathscr{H}_{1,2}\psi_a(\mathbf{r}_2)\psi_b(\mathbf{r}_1). \tag{2.8}$$

The energy contribution responsible for the Coulomb interaction E_{Coulomb} has a purely classical basis, and thus is disregarded for the remainder of this derivation. The remaining consideration is given to the quantum mechanical exchange energy E_{exchange}, whereby exchanging the electron positions would have an immediate effect, unlike in the classical case. To introduce the effects of electron spin, the individual wavefunctions ψ_a and ψ_b can be described as the combination of two parts $\phi(\mathbf{r})$ and χ, representing spatial and spin contributions respectively:

$$\Psi_{\text{S}} = \frac{1}{\sqrt{2}}\left[\phi_a(\mathbf{r}_1)\phi_b(\mathbf{r}_2) + \phi_a(\mathbf{r}_2)\phi_b(\mathbf{r}_1)\right]\chi_{\text{S}}, \tag{2.9}$$

$$\Psi_{\text{T}} = \frac{1}{\sqrt{2}}\left[\phi_a(\mathbf{r}_1)\phi_b(\mathbf{r}_2) - \phi_a(\mathbf{r}_2)\phi_b(\mathbf{r}_1)\right]\chi_{\text{T}}. \tag{2.10}$$

This is defined such that the total wavefunction of the electron still remains antisymmetric. This is because in the case that there is spatial symmetry, the spin component is antisymmetric, and if there is spin symmetry, the spatial component is antisymmetric. These two possible combinations are labelled as S and T, which stand for singlet (symmetric spatially) and triplet (antisymmetric spatially) states. Based on the alignment of spins, the singlet state has spin quantum number $s = 0$, and the triplet state has $s = 1$. Next, the total energies for both states are defined as the following:

$$E_{\text{S}} = \iint \Psi_{\text{S}}^* \mathscr{H} \Psi_{\text{S}}\, d\mathbf{r}_1\, d\mathbf{r}_2, \tag{2.11}$$

$$E_{\text{T}} = \iint \Psi_{\text{T}}^* \mathscr{H} \Psi_{\text{T}}\, d\mathbf{r}_1\, d\mathbf{r}_2. \tag{2.12}$$

In order to consider the differences between the singlet and triplet states, the difference between them can be defined according to

$$E_{\mathrm{S}} - E_{\mathrm{T}} = 2\iint \phi_a^*(\mathbf{r}_1)\phi_b^*(\mathbf{r}_2)\mathscr{H}\phi_a(\mathbf{r}_2)\phi_b(\mathbf{r}_1)\,d\mathbf{r}_1\,d\mathbf{r}_2. \tag{2.13}$$

Defining the spin operators at sites 1 and 2 in this system as $\mathbf{S}_1$ and $\mathbf{S}_2$, they can be joined to get $(\mathbf{S}_1+\mathbf{S}_2)^2 = \mathbf{S}_1^2+\mathbf{S}_2^2+2\mathbf{S}_1\cdot\mathbf{S}_2$, with eigenvalues $S(S+1)$. By noting that the eigenvalues of both $\mathbf{S}_1$ and $\mathbf{S}_2$ is $\frac{3}{4}$ (given that $S(S+1)=\frac{1}{2}\cdot\left(\frac{1}{2}+1\right)$), in the singlet case, the product component $\mathbf{S}_1\cdot\mathbf{S}_2$ yields $\left(0-\frac{6}{4}\right)\cdot\frac{1}{2}=-\frac{3}{4}$, whereas in the triplet case $\left(2-\frac{6}{4}\right)\cdot\frac{1}{2}=\frac{1}{4}$. An effective Hamiltonian according to the singlet and triplet product components can now be written as

$$\mathscr{H} = \frac{1}{4}(E_{\mathrm{S}}+3E_{\mathrm{T}}) - (E_{\mathrm{S}}-E_{\mathrm{T}})\mathbf{S}_1\cdot\mathbf{S}_2. \tag{2.14}$$

This effective Hamiltonian follows the definition that if $\mathbf{S}_1\cdot\mathbf{S}_2=-\frac{3}{4}$ (singlet), then $\mathscr{H}=E_{\mathrm{S}}$, and vice versa for the triplet case. The first (spatial) term in equation 2.14 shows no dependency with respect to spin, and thus is treated as a constant. As for the spin dependent terms, the constant factor in front of $\mathbf{S}_1\cdot\mathbf{S}_2$ is denoted by an exchange factor J. The exchange integral can then be defined according to

$$J = \frac{E_{\mathrm{S}}-E_{\mathrm{T}}}{2} = \iint \phi_a^*(\mathbf{r}_1)\phi_b^*(\mathbf{r}_2)\mathscr{H}\phi_a(\mathbf{r}_2)\phi_b(\mathbf{r}_1)\,d\mathbf{r}_1\,d\mathbf{r}_2. \tag{2.15}$$

Finally, the effective spin Hamiltonian can be obtained by substituting equation 2.15 with equation 2.14, and removing any constants. This gives:

$$\mathscr{H}_{\text{exch}} = -2J\mathbf{S}_1\cdot\mathbf{S}_2. \tag{2.16}$$

Given a positive value of the exchange constant J, minimum energy is achieved in the triplet state ($s=1$), whereas the singlet state is the minimum for a negative J with $s=0$. The Heisenberg exchange spin Hamiltonian can then be written as the following for magnetic systems, with multiple localised interacting spin sites (with interactions up to the first nearest-neighbour):

$$\mathscr{H}_{\text{exch}} = -\sum_{i<j} J_{ij}^{\text{1-nn}}\mathbf{S}_i\cdot\mathbf{S}_j, \tag{2.17}$$

where the first nearest-neighbour exchange coupling factor $J_{ij}^{\text{1-nn}}$ is a system dependent constant for the coupling between sites i and j, with the factor-two being omitted so as to not double count. For ferromagnetic systems that minimise energy via parallel spin alignment, the exchange coupling value takes the constraint $J_{ij}^{\text{1-nn}}>0$, whereas in the antiferromagnetic case causing opposing alignment $J_{ij}^{1\text{-nn}} < 0$. Figure 2.1 summarises the differences between ferromagnetic, antiferromagnetic, and paramagnetic spin configurations assuming up to first nearest-neighbour exchange interactions.

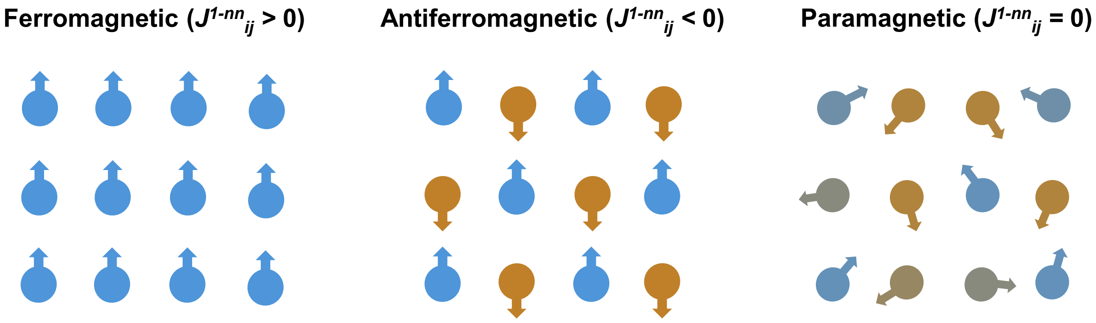
Ferromagnetic ($J^{1\text{-}nn}_{ij} > 0$)
Antiferromagnetic ($J^{1\text{-}nn}_{ij} < 0$)
Paramagnetic ($J^{1\text{-}nn}_{ij} = 0$)

Fig. 2.1 Ferromagnetic, antiferromagnetic, and paramagnetic spin configurations. The ferromagnetic case causes parallel alignment due to $J_{ij}^{1\text{-nn}} > 0$, the antiferromagnetic case causes opposing exchange between spin sites to nullify the effective field by having $J_{ij}^{1\text{-nn}} < 0$. Finally, the paramagnetic state shows no preferential alignment direction, and thus are fully randomly oriented.

In a practical case, as a means of deriving the exchange coupling factor between spins in a system, the mean-field approach applied to spin-waves was utilised [39], which describes a relationship between the T_{C} of a system and its nearest-neighbour configuration to extract a value for $J_{ij}^{1\text{-nn}}$. This is written as the following:

$$J_{ij}^{1\text{-nn}} = \frac{3k_{\mathrm{B}}T_{\mathrm{C}}}{\varepsilon z}, \tag{2.18}$$

where k_{B} is the Boltzmann constant, ε is a spin-wave correction factor, and z is the number of first nearest-neighbours [39]. ε is a factor that corrects for spin waves in the Heisenberg exchange interaction, and varies depending on the crystal structure of the system [40].

2.1.2 Anisotropy energy

With respect to the crystallographic orientation of spin sites in a lattice, a system is defined to have an anisotropy energy if there are differences in the energy states for given spin directions over others. The two main interactions governing the presence of magnetocrystalline anisotropy are spin-orbit coupling, and the crystal-field interaction. The effects of spin-orbit coupling arise from the electron spin in the presence of the crystal-field. This can be interpreted as the electrons being under the influence of a local magnetic field from their angular momentum being affected by the electric field near the atom [41]. The strongly overpowering electrostatic crystal field within the presence of a lattice structure most times leads to an insignificant orbital moment when compared to the effects of the spin moment. This reduction of orbital moment is known as quenching. This relationship between the configuration of the lattice and the inherently asymmetric electron orbital wavefunctions leads to energies dependent on direction, which is defined as magnetocrystalline anisotropy. In order to quantify and implement an anisotropic energy term from an atomistic perspective, the uniaxial (alignment along a preferred axis) case is described as

$$\mathscr{H}_{\text{uniaxial}} = -k_{\text{u}} \sum_i (\mathbf{S}_i \cdot \hat{\mathbf{e}}_i)^2, \tag{2.19}$$

whereby the energy value k_{u} regulates the anisotropic energy contribution given a reference spin $\mathbf{S}$ at site i with respect to the axis of preferential alignment (easy-axis) $\hat{\mathbf{e}}$. An easy-axis arises in $\text{L}1_0$ FePt for example due to a symmetry breaking interaction of the lattice along the z-axis, which leads to a preference of spin alignment along the stacking plane of Fe and Pt species. With respect to an azimuthal angle θ, a general form of the easy axis energies can be defined in the form $\mathscr{H}_{\text{uniaxial}} = k_{\text{u}} \sin^2(\theta)$ [42], where this energy is minimised at $\theta = 0°$ and $\theta = 180°$.

Given a cubic lattice, and no compression along the z-axis, oftentimes a cubic form of anisotropy emerges, which in the case of disordered FePt, tends to be a significantly weaker contribution than its uniaxial counterpart in an ordered state. Cubic anisotropies arise when there is symmetry along all the cubic lattice faces, and thus the system has a preferential alignment along multiple easy axes. Given a set of easy axes along [100], [010], and [001] directions, one can describe the cubic anisotropies following the form seen in Kronmüller [43]:

$$\mathscr{H}_{\text{cubic}} = -\frac{k_{\text{c}}}{2} \sum_i \gamma_i^4, \tag{2.20}$$

where k_{c} defines the cubic anisotropy energy for a sum of spins labelled by i. γ_i refers to the dot products of the spin vector with the easy axes, $\gamma_i = (\mathbf{S}_i \cdot \hat{\mathbf{e}}_{i,x}) + (\mathbf{S}_i \cdot \hat{\mathbf{e}}_{i,y}) + (\mathbf{S}_i \cdot \hat{\mathbf{e}}_{i,z})$. Given that the easy axes are orthogonal, one can use the expanded form of γ_i with equation 2.20 to get the equation governing cubic anisotropy interactions [28, 44]:

$$\mathscr{H}_{\text{cubic}} = -\frac{k_{\text{c}}}{2} \sum_i (S_{i,x}^4 + S_{i,y}^4 + S_{i,z}^4), \tag{2.21}$$

where S_x, S_y, and S_z are the directional spin components in the spin vector along the x, y, and z axes.

2.1.3 Two-ion anisotropy

The two-ion anisotropy energy arises due to a mechanism involving two different material species in the same lattice that both simultaneously contribute to the anisotropy configuration of a given atomistic site. In the case of $L1_0$ FePt, the addition of a two-ion anisotropy term was introduced in Mryasov *et al.*, and arises due to the anisotropic nature of the exchange interaction [30]. The two-ion term is important here, as it determines the Fe energy assuming Pt sites as an intermediary to this interaction. This requires a further expression from the previous onsite and single-ion term seen in section 2.1.2, which includes the tensorial form of the anisotropy energy represented by

$$\mathscr{H}_{\text{2-ion}} = -\sum_{i,j} \mathbf{S}_i^T k_{ij} \mathbf{S}_j, \tag{2.22}$$

where the summation determines the anisotropic energy via k_{ij} with relation to the spin unit vector $\mathbf{S}$ at sites i and j. k_{ij} consists of diagonal and off-diagonal components for x, y, and z directions, however according to Mryasov *et al.* in $L1_0$ FePt, the x and y directional components are zero. To construct the total anisotropy energies in the generalised case for $L1_0$ FePt, a combination of single-ion and two-ion terms are used:

$$\mathscr{H}_{\text{ani}} = -\sum_{i} k_{\text{1-ion}} (\mathbf{S}_i^z)^2 - \sum_{i,j} k_{\text{2-ion}}^z \left(\mathbf{S}_i^z \cdot \mathbf{S}_j^z \right), \tag{2.23}$$

where $k_{\text{1-ion}}$ is the uniaxial single-site dependent anisotropy constant, and $k_{\text{2-ion}}$ is the first-nearest neighbour dependent anisotropy contribution. The terms with the z superscript denote that the non-zero z-component is being considered.

2.1.4 Applied magnetic fields

Applied magnetic fields affect the preferential direction of spins. A system will seek to minimise energy by aligning spins along the direction of this applied field. To quantify the applied field energies, the following form is used [45]:

$$\mathscr{H}_{\text{applied}} = -\mu_s \sum_{i} \mathbf{B} \cdot \mathbf{S}_i, \tag{2.24}$$

where μ_s corresponds to the magnetic moment of spin $\mathbf{S}_i$ within an applied field $\mathbf{B}$. The energy minimising behaviour for a magnetic moment in an applied field is what gives rise to the atomistic modelling of Heat Assisted Magnetic Recording (HAMR), whereby this term regulates the magnetic switching process of all the affected spin sites.

2.1.5 The Landau expansion and longitudinal dynamics

A core focus of the simulation strategies developed in this thesis centre around the development of a longitudinal spin dynamics model, which aims to more appropriately describe the changes to the magnitude of the magnetic moment with temperature [46–48]. A fundamental assumption of the atomistic Heisenberg model is that moments are perfectly locally bound by lattice sites, and it fails to describe the nature of changes to the magnitude of the magnetic moment at a given site. From a more physical perspective, electrons tend to greatly vary in locality given changes to their nearest-neighbour configuration, which changes the immediate net magnetic moment associated to a site.

In order to map the material specific moment size dependence to the energies of a system, even powers of the Landau expansion are used as a basis for regulating longitudinal changes. From a general standpoint, the Landau expansion describes continuous phase-transitions with respect to a given ordering parameter. In this case, the associated ordering parameter is the quantity $|S|$, and thus the longitudinal Landau Hamiltonian is given by the equation [31, 46–50]:

$$\mathscr{H}_L = \sum_i \sum_\alpha A_\alpha |S_i|^2 + B_\alpha |S_i|^4 + C_\alpha |S_i|^6, \tag{2.25}$$

where A_α, B_α, and C_α are Landau coefficients that use α to denote their material dependence. It should be noted that the Landau Hamiltonian in this case is an even function, and thus when $|S| = 0$, the second-order coefficient will have to be $A_\alpha > 0$, so as to form a new minimum at the point where $E = 0$ [49]. As a consequence of this, when the system energy minimum is defined at $E < 0$, $A_\alpha < 0$ has to hold. It is not entirely clear if a Landau expansion including odd-powers would work, however thus far the standard convention has been to include only even powers of $|S|$.

The relationship between the scaling of $|S|$ with respect to energy is purely determined by the coefficients, which is in turn heavily informed by the system's reference energy states according to the values of $J_{ij}^{\text{1-nn}}$, and k_u. It is important to highlight that the exchange contribution is orders of magnitude larger than the anisotropy contribution in most systems. To represent these effects, the complete spin Hamiltonian with longitudinal contributions can be written as:

$$\mathscr{H}_\text{total} = \sum_i \sum_\alpha A_\alpha |S_i|^2 + B_\alpha |S_i|^4 + C_\alpha |S_i|^6 - \sum_{i<j} J_{ij}^{\text{1-nn}} \mathbf{S}_i \cdot \mathbf{S}_j - k_\text{u} \sum_i (\mathbf{S}_i \cdot \hat{\mathbf{e}}_i)^2. \tag{2.26}$$

The justification for mapping the ordering parameter using $|S|$ instead of the actual atomic spin moment quantity μ_s is natural: when calculating the magnetisation energies corresponding to a certain spin configuration, the quantity μ_s is combined with the spin vector quantity

$\mathbf{S}$, as a reflection of the magnetisation strength in a given species. Thus, varying $|S|$ while keeping the quantity μ_s constant has the intended effect, however it is numerically easier to handle given that all materials are normalised to $|S| = 1$ at equilibrium, or in the case of non-magnetic materials, they are normalised to $|S| = 0$. In order for longitudinal changes to be naturally accounted for in the form of the spin Hamiltonian, the standard spin vector which includes spin length changes is defined as $\mathbf{S} = \hat{\mathbf{S}}|S|$, whereas in the more conventional Heisenberg Hamiltonian, the vector $\mathbf{S}$ refers to a normalised unit vector quantity $\hat{\mathbf{S}}$, which explicitly forces $|S| = 1$, hence no change occurs to the moment size.

It should be highlighted that the Landau expansion is not restricted up to the sixth-order term $|S|^6$, and equivalently does not require coefficients up to the sixth-order. Each coefficient differently regulates the form of the longitudinal energy surface, and as a result different materials will require different contributions from the terms in the expansion. As an example, the C_α coefficient regulating the sixth-order term is only valid if a material requires a strictly constrained maximum of $|S|$. Additionally, although this research has found that none of the investigated materials warrant it, an $|S|^8$ term is equally applicable for a generally shallow longitudinal surface, that has an otherwise strict limitation on the growth of $|S|$ beyond a certain limit.

To quantify a material's Landau coefficients, Density of States (DOS) Density Functional Theory (DFT) calculations are employed to determine the energy with respect to moment size. While the research done in this thesis does not include the computation of the coefficients, a summary as to the general methods applied is provided. According to the Fixed Spin-Moment (FSM) method, the DOS given a constant magnetic moment can be mapped according to the Fermi energies of spin up and spin down states [51, 52]. The following two equations describe the DOS calculations for the magnetic moment and number of electrons respectively [49, 53]:

$$M = \int_{-\infty}^{\varepsilon_{\text{up}}} D(E)\,dE - \int_{-\infty}^{\varepsilon_{\text{down}}} D(E)\,dE, \tag{2.27}$$

$$N = \int_{-\infty}^{\varepsilon_{\text{up}}} D(E)\,dE + \int_{-\infty}^{\varepsilon_{\text{down}}} D(E)\,dE, \tag{2.28}$$

where M is the magnetic moment, and N is the number of d electrons. ε_{up} and $\varepsilon_{\text{down}}$ represent the spin up and spin down Fermi levels. It is natural to pose a question about the physicality of having unequal Fermi levels for the spin up and spin down states. The FSM method requires that $\varepsilon_{\text{up}} \neq \varepsilon_{\text{down}}$, as this relation is how the energy for an arbitrary spin moment magnitude can be calculated. This can be viewed as artificially constraining the spin up and spin down DOS to be able to compute energies for magnetic moment sizes that are otherwise impossible at the ground state.

Given that the Stoner model describes energy bands according to $E_{\text{total}} = E_{\text{up}} + E_{\text{down}} - \frac{1}{4}IM^2$ which is the summation of spin up and spin down electron energies, along with a Stoner parameter term I which accounts for two-body correlations between electrons, the function E_{total} can be mapped onto the Landau expansion while keeping its dependence on M, the moment size [49, 53]. This yields the equation [49]:

$$E_{\text{total}} \approx E_0(M) + aM^2 + bM^4 + cM^6, \tag{2.29}$$

where a, b, and c are coefficients that are directly proportional to A_α, B_α, and C_α. $E_0(M)$ is an energy function that arises from the exchange and anisotropy energies in the system, contributing to the total depth and position of the longitudinal energy surface. It can be seen as a result, that the reference energy states in this process directly inform the Landau coefficients. This means that variations in a system's exchange energy reference state while computing the coefficients *vs.* applying them in calculations will result in variability for the equilibrium value of $|S|$, denoted by the minimum of the longitudinal energy surface. This poses a challenge, as from a practical standpoint it is not feasible to compute a set of new coefficients for minor changes in a system's configuration. For example even changes in system size will affect the average exchange coupling between spin sites, leading to a shift away from the reference energy state the coefficients were computed with. A crucial method of verifying that a system's coefficients are valid is that at equilibrium, the value $|S| = 1$ holds, to appropriately reflect the size of its original moment μ_s.

Being able to map the moment size changes to a constrained potential energy calculation enables for atomistic simulation of moments that are more itinerant in origin. A primary focus of this thesis will be looking at the consequences of the calculation of the magnetic properties of systems, where the total magnetisation is wholly affected by changes to the spin length quantity $|S|$.

2.2 Atomistic integrator schemes

2.2.1 The stochastic Landau-Lifshitz-Gilbert integrator

Fundamentally the magnetization per unit volume, $\mathbf{M}$, under the influence of a field will tend to minimise energy via aligning its moments with the field via a torque density τ. This motion is known as Larmor precession [42]. To represent this in an undamped case, whereby the magnetic moment referenced will undergo precession, the following equation describes the time evolution [42]:

$$\frac{\partial \mathbf{M}}{\partial t} = -\gamma \tau, \tag{2.30}$$

where $\gamma = 1.76 \times 10^{11}$ $\mathrm{s}^{-1}\mathrm{T}^{-1}$, and is the gyromagnetic ratio of an electron. The torque density can be computed via the cross product of the magnetization **M** with magnetic field **B** to give

$$\frac{\partial \mathbf{M}}{\partial t} = -\gamma \mu_0 \mathbf{M} \times \mathbf{B}, \tag{2.31}$$

where μ_0 is the permeability of free space. In an undamped case, the magnetic moment is stuck in precession around a central axis determined by the field direction. This is because no energy is lost over time, and thus its motion can be maintained. Once damping considerations are introduced, an augmentation to equation 2.31 must follow, which is defined such that as $t \to \infty$, the moment will align exactly with the field direction. The following equation is known as the Landau-Lifshitz (LL) equation, which defines this damped behaviour [54]:

$$\frac{\partial \mathbf{M}}{\partial t} = -\gamma \mathbf{M} \times \mathbf{H} - \gamma \alpha \mathbf{M} \times (\mathbf{M} \times \mathbf{H}), \tag{2.32}$$

where α is the phenomenological damping constant, and the relation $\mathbf{H} = \mu_0 \mathbf{B}$ is used, where the units of the effective field **H** is Teslas. The damping parameter regulates how quickly energy is lost to the system via the inherent properties of the system such as lattice environment, or the external factors present surrounding the system such as changes in temperature. As a result of this, it is evident in the LL equation that the damping term is system dependent. It was determined by Gilbert that the dissipation term arising due to damping was not appropriately being scaled according to the time evolution of the magnetization, $\frac{\partial \mathbf{M}}{\partial t}$ [55]. As a result, the following equation was constructed, which is known as the Landau-Lifshitz-Gilbert equation:

$$\frac{\partial \mathbf{S}_i}{\partial t} = -\frac{\gamma}{(1+\lambda^2)}[\mathbf{S}_i \times \mathbf{H}_i + \lambda \mathbf{S}_i \times (\mathbf{S}_i \times \mathbf{H}_i)], \tag{2.33}$$

where a microscopic damping parameter λ is now used, and **M** can be rewritten according to the identity $\mathbf{M} = \mu_s \mathbf{S}$. Equation 2.33 is also written in the atomistic form (with reference to site i), to demonstrate its implementation into an atomistic computational framework.

2.2.2 The Heun solver

As a means of the computational implementation and overall usage of the dynamic integrator schemes detailed this thesis, a solution to the stochastic form of the equation of motion must be calculated. A key characteristic of the chosen solver is that it has to provide convergence to the true value of the solved stochastic equation within a reasonable amount of steps. The Heun scheme is a two-step second-order Runge-Kutta method, which calculates a solution to the LLG equation via a predictor and a corrector step. As opposed to the single step variant known as the Euler scheme, the computational sacrifice of committing two steps to a single calculation of the gradient is significantly outweighed when considering how much more accurate the calculated value is. This leads to the consideration that larger timestep sizes can be used, which yields quicker simulation times overall. Given an equation of motion to calculate the time evolution of a spin site, the initial predictor step defines the new intermediate direction according to [56]:

$$\mathbf{S}_i' = \mathbf{S}_i + \Delta\mathbf{S}\Delta t, \tag{2.34}$$

where Δt refers to the size of the timestep, with the change in spin vector due to the equation of motion as $\Delta\mathbf{S}$. In order to apply a correction to this within the same timestep, the following corrector step is used:

$$\mathbf{S}_i^{t+\Delta t} = \mathbf{S}_i + \frac{\Delta t}{2}\left[\Delta\mathbf{S} + \Delta\mathbf{S}'\right], \tag{2.35}$$

where $\Delta\mathbf{S}'$ now refers to the change in spin vector due to the equation of motion having used the intermediate spin position in equation 2.34. During this process, it is noted that the spin fields are recalculated once at the beginning of each timestep, and once after the predictor step. It is well established that convergence for the LLG is reasonably reached with $\Delta t = 1\text{fs}$ for the LLG-Heun integrator, however given the introduction of longitudinal dynamics in this thesis, additional confirmation is necessary for the newly implemented longitudinal LLG equation of motion [28, 57]. As a result, the fourth-order variant of the Runge-Kutta solver is also implemented.

The order of errors associated with the Heun scheme is quantifiably small: with a timestep size of $\Delta t = 1$ fs, and damping $\lambda = 0.1$, an error of magnitude 10^{-6} can be expected when computing the precession of a single spin in an effective field [28].

2.2.3 Effective magnetic field

As a further development to the derivation of the LL (and subsequently the LLG) equation, the effective field at site i given by $\mathbf{H}_i$ is a term referring to the collective effects of all fields acting on the spin sites, which is parametrised according to the energies of the total Hamiltonian. In order to compute the effective field contributions of the system's energies, the derivative with respect to spin vector $\mathbf{S}_i$ is taken. The effective field calculation takes place according to

$$\mathbf{H}_i = -\frac{1}{\mu_s}\frac{\partial \mathscr{H}}{\partial \mathbf{S}_i}. \tag{2.36}$$

While the standalone LLG equation describes a fully deterministic calculation, a stochastic thermal noise term constructs a coupling mechanism to the system via a thermal heat bath. This is based on Langevin dynamics, which in a general sense describes the effects of a random force with relation to a thermodynamic system [58]. The complete form of the effective field with the additional thermal noise term is described as

$$\mathbf{H}_i^{\text{total}} = -\frac{1}{\mu_s}\frac{\partial \mathscr{H}}{\partial \mathbf{S}_i} + \boldsymbol{\Gamma}(t)\sqrt{\frac{2\lambda k_{\text{B}} T}{\gamma \mu_s \Delta t}}, \tag{2.37}$$

where $\boldsymbol{\Gamma}(t)$ is a Gaussian distribution of mean 0 and width 1, k_{B} is the Boltzmann constant, T is the system temperature, and Δt is the timestep size. The consequence of the thermal noise term is that significantly larger random changes are made to the effective field as temperature increases, which allows for the computation of disordered states at high temperatures. At $T = 0$ K, no fluctuations are introduced to the system, and thus an ordered system prevails. The choice of using a white noise representation of the stochastic nature of energy exchange with the heat bath follows the assumption that the dissipation of energy is not correlated in time. As a result, a commitment is made to introducing this behaviour via a stochastic term [59, 60]. To visualise the relationship between the precession term, damping term, and the thermal noise term, figure 2.2 shows a visual summary.

It should be noted, that the LLG equation assumes a fixed rotation around a unit sphere ($|S| = 1$) and thus calculating the time-evolution of a system with longitudinal degrees of freedom according to the atomistic Landau Hamiltonian would not be valid, as the unconstrained spin length quantity would not be able to evolve.

2.2.4 The longitudinal Landau-Liftshitz-Gilbert integrator

In order to incorporate atomistic longitudinal dynamics into the LLG integration scheme, the phase space of the conventional LLG must be augmented such that it accounts for a variable unit sphere in the precession and dissipation terms. Ma *et al.* builds a relationship between the Langevin equation for the motion of atoms and the Langevin equation for spins [49]. Conventionally, the Langevin equation to model the motion of interacting atoms can be described by

$$\frac{d\mathbf{p}_i}{dt} = -\frac{\partial U(\mathbf{x}_i)}{\partial \mathbf{x}_i} - \lambda\frac{\mathbf{p}_i}{m} + \mathbf{f}_i, \tag{2.38}$$

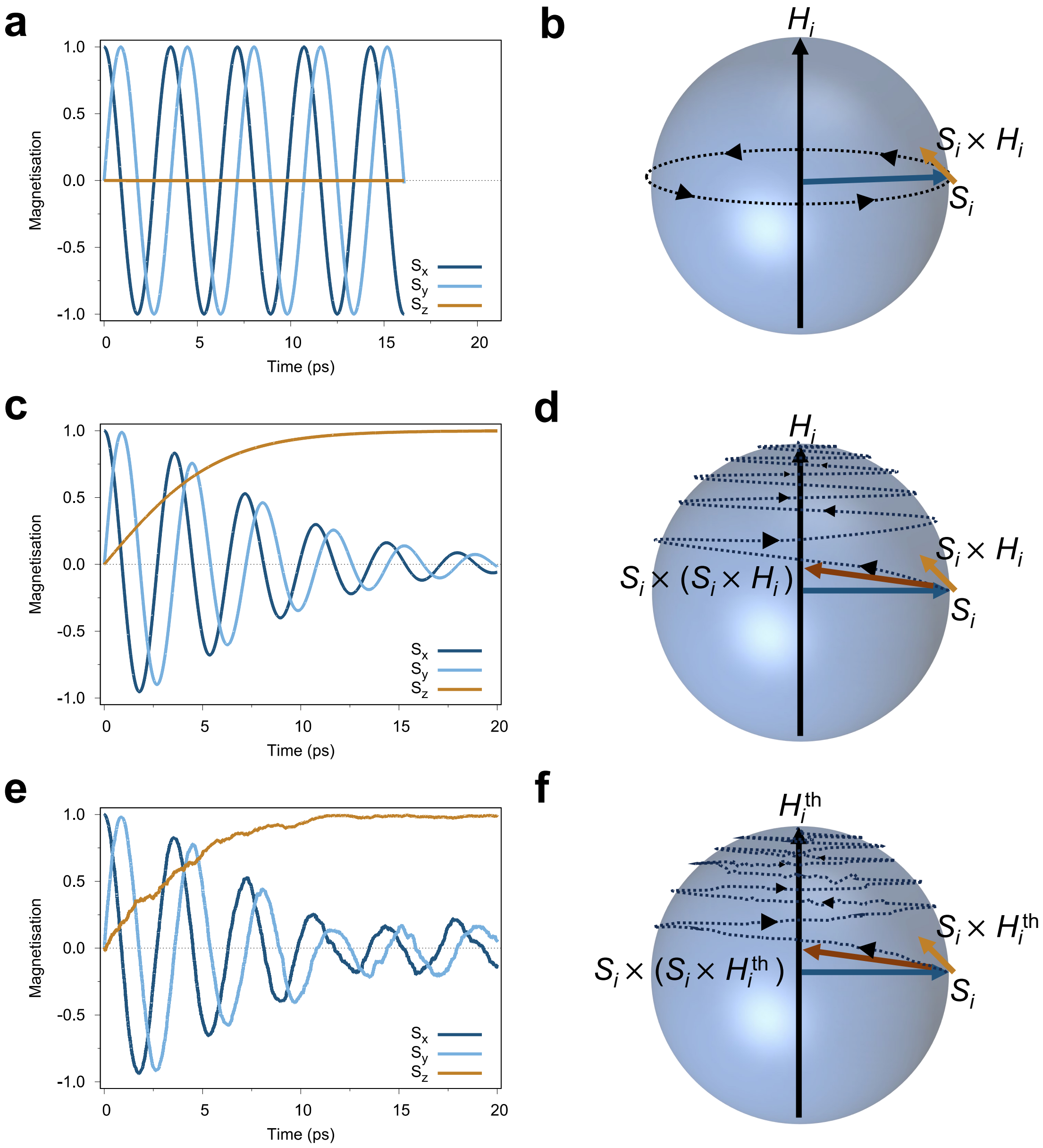

Fig. 2.2 The LLG integrator broken down into different components, (a), (b) showing undamped precession, (c), (d) showing the effects of the damping term, and (e), (f) showing the application of stochastic thermal noise.

where $\mathbf{p}_i$ represents momentum, $U(\mathbf{x}_i)$ is the potential energy between the atomistic sites, which varies with position $\mathbf{x}_i$, and $\mathbf{f}_i$ represents a force due to random fluctuations. These terms all are site dependent, in this case denoted by i. λ is the damping parameter, and m represents the mass of the atom. The first term $-\frac{\partial U(\mathbf{x}_i)}{\partial \mathbf{x}_i}$ can be identified as a deterministic force. Additionally, the second dissipative term in equation 2.38 can be rewritten as [61]

$$-\lambda \frac{\mathbf{p}_i}{m} = -\lambda \frac{\partial \mathscr{H}}{\partial \mathbf{p}_i}. \tag{2.39}$$

Using the LLG form, equation 2.38 can then be rewritten in terms of the total spin vector $\mathbf{S}_i$, and thus the following equation is obtained as follows:

$$\frac{\partial \mathbf{S}_{\mathrm{LSF}}}{\partial t} = -\gamma \left[\mathbf{S}_i \times \left(-\frac{\partial \mathscr{H}}{\partial \mathbf{S}_i} \right) \right] + \gamma\lambda \left(-\frac{\partial \mathscr{H}}{\partial \mathbf{S}_i} \right) + \boldsymbol{\xi}_i, \tag{2.40}$$

$$\frac{\partial \mathbf{S}_{\mathrm{LSF}}}{\partial t} = -\gamma(\mathbf{S}_i \times \mathbf{H}_i) + \gamma\lambda \mathbf{H}_i + \boldsymbol{\xi}_i. \tag{2.41}$$

$\boldsymbol{\xi}_i$ is a stochastic thermal noise term, whereby it is considered via addition to the overall equation of motion, rather than to the effective field vector $\mathbf{H}$. $\boldsymbol{\xi}_i$ is calculated according to [49, 50]:

$$\boldsymbol{\xi}_i = \boldsymbol{\Gamma}(t) \sqrt{\frac{2\gamma\lambda k_{\mathrm{B}} T}{\mu_s \Delta t}}. \tag{2.42}$$

The terms representing the motion of the spin with relation to dissipation due to damping in equation 2.41 assumes strictly that $\lambda_{\mathrm{transverse}} = \lambda_{\mathrm{longitudinal}}$. While it enables the construction of this equation of motion which consequently proves the fluctuation-dissipation relationship ($\mu_s = 2\lambda k_{\mathrm{B}} T$) when used with the Fokker-Planck equation found in Ma *et al.*, it is not assumed to be an accurate description of what occurs physically [49, 62]. Although the equation of motion has changed compared to the conventional LLG, it is still valid to use the same solver schemes to obtain a convergent solution when committing to calculations. This is shown in chapter 4, where tests are carried out to ensure that the results converge to the same values using both the Heun and fourth-order Runge Kutta solvers.

To extract the effective field components from the Landau Hamiltonian for use in the LSF-LLG integrator scheme, the Landau Hamiltonian has to be expressed as effective field terms. The identity $\mathbf{H}_i = -\frac{1}{\mu_s} \nabla_{\mathbf{S_i}} \mathscr{H}_L$ can be used to compute the longitudinal field contributions at each timestep. The partial is considered with respect to S_x, S_y, and S_z, spin components, as the quantity $|S|$ is defined by the S_x, S_y, and S_z components according to $|S| = \sqrt{{S_x}^2 + {S_y}^2 + {S_z}^2}$. The decomposed field terms are shown in the following equations:

$$H_x^L = -\frac{S_x}{\mu_s} \left[2A'_\alpha + 4B'_\alpha \left(S_x^2 + S_y^2 + S_z^2 \right) + 6C'_\alpha \left(S_x^2 + S_y^2 + S_z^2 \right)^2 \right], \tag{2.43}$$

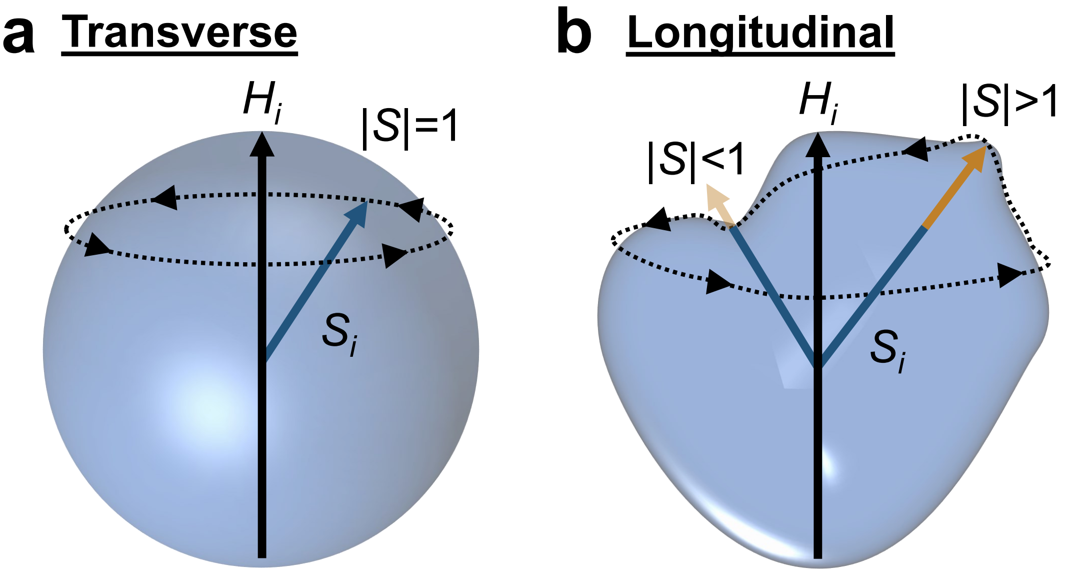

Fig. 2.3 The schematic differences between the conventional transverse-only relaxation of a spin in (a) compared to the longitudinal variant in (b). The longitudinal LLG enables longitudinal degrees of freedom as well as transverse as it removes the constraint of the unit sphere.

$$H_y^L = -\frac{S_y}{\mu_s}\left[2A'_\alpha + 4B'_\alpha\left(S_x^2+S_y^2+S_z^2\right) + 6C'_\alpha\left(S_x^2+S_y^2+S_z^2\right)^2\right], \tag{2.44}$$

$$H_z^L = -\frac{S_z}{\mu_s}\left[2A'_\alpha + 4B'_\alpha\left(S_x^2+S_y^2+S_z^2\right) + 6C'_\alpha\left(S_x^2+S_y^2+S_z^2\right)^2\right]. \tag{2.45}$$

From these identities, the effective field **H** can be augmented to include these terms, which will lead to changes in $|S|$.

Overall, figure 2.3 illustrates the allowed relaxation dynamics for conventional and longitudinal dynamics cases.

2.2.5 The fourth-order Runge-Kutta solver

The newly developed LSF-LLG uses the Heun solver, however it is important to validate its convergence to its calculated gradient within an expected number of steps. In order to do this, a naturally more accurate (though more computationally demanding) extension would be to implement the fourth-order Runge-Kutta solver, which has 4 intermediate steps as compared to the Heun scheme. The larger number of slope calculations leads to an estimate with less error in general. The RK4 yields 4 intermediate spin vectors via four calculations of the gradient at different times denoted by $\mathbf{S}'_1$, $\mathbf{S}'_2$, $\mathbf{S}'_3$, and $\mathbf{S}'_4$. The weighted sum of these newly generated intermediate vectors gives the final new spin direction of the system for a given timestep. The slopes are recalculated for every timestep, with a recalculation of the spin fields taking place at the beginning of a new timestep, between $\mathbf{S}'_1$ and $\mathbf{S}'_2$, and between $\mathbf{S}'_3$ and $\mathbf{S}'_4$. The following equations show the calculation of the four steps [57]:

$$\mathbf{S}'_1 = \Delta\mathbf{S}_1\left(\mathbf{S}_{\text{initial}}\right)\Delta t, \tag{2.46}$$

$$\mathbf{S}'_2 = \frac{1}{2}\Delta\mathbf{S}_2\left(\mathbf{S}'_1\right)\Delta t, \tag{2.47}$$

$$\mathbf{S}'_3 = \frac{1}{2}\Delta\mathbf{S}_3\left(\mathbf{S}'_2\right)\Delta t, \tag{2.48}$$

$$\mathbf{S}'_4 = \Delta\mathbf{S}_4\left(\mathbf{S}'_3\right)\Delta t. \tag{2.49}$$

$\Delta\mathbf{S}_1\left(\mathbf{S}_{\text{initial}}\right)$, $\Delta\mathbf{S}_2\left(\mathbf{S}'_1\right)$, $\Delta\mathbf{S}_3\left(\mathbf{S}'_2\right)$, and $\Delta\mathbf{S}_4\left(\mathbf{S}'_3\right)$ defines the calculation of the equation of motion as a function of the intermediate spins. The four estimates taken are then combined according to a weighted average written as the following equation:

$$\mathbf{S}_i^{t+\Delta t} = \frac{1}{3}\mathbf{S}'_1 + \frac{1}{6}\mathbf{S}'_2 + \frac{1}{6}\mathbf{S}'_3 + \frac{1}{3}\mathbf{S}'_4. \tag{2.50}$$

In order to demonstrate a visual comparison of the difference in convergence time between the two solvers, figure 2.4 shows a sample equation of motion with the equivalent solutions obtained by the Heun and RK4 methods. It can be seen that although both methods use more than one gradient estimation step, the RK4 has a noticeably smaller error than the Heun solver when looking at small timescales. To quantify, Lepadatu [63] computes this error to be of the order 10^{-10} when computing the spin vector.

2.2.6 The Landau-Lifshitz-Bloch integrator

The Landau-Lifshitz-Bloch (LLB) integrator follows the LLG equation of motion with the augmentation to allow an unconstrained unit sphere when employing the equation of motion. This was done by keeping the precession and damping terms, while adding a longitudinal motion term with its own characteristic damping parameter. This fully implies that the transverse and longitudinal processes are operational on separate timescales, unlike the longitudinal LLG form introduced in section 2.2.4 where $\lambda_{\text{transverse}} = \lambda_{\text{longitudinal}}$. While this form introduces complexities with finite-size scaling effects of magnetisation against temperature calculations, it is able to provide insight into an atomistic model that includes

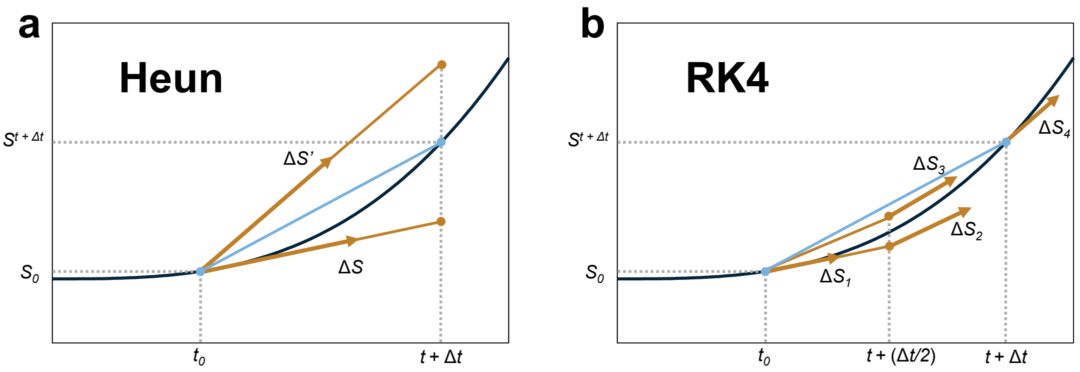

Fig. 2.4 An example comparison of the convergence behaviour between the (a) Heun and (b) fourth-order Runge-Kutta (RK4) solvers. The RK4's final gradient (light-blue) is calculated via an averaging of all four gradients. It is clear that the RK4 converges to its result with even larger timestep sizes, though the Heun scheme has shown effectiveness in all calculations done in this thesis.

longitudinal dynamics as part of its equation of motion. The atomistic LLB takes on the equation of motion described as [64–67]:

$$\frac{\partial \mathbf{S}_{\mathrm{LLB}}}{\partial t} = -\gamma(\mathbf{S}_i \times \mathbf{H}_i) + \frac{\gamma\lambda_{\mathrm{l}}}{S^2}[\mathbf{S}(\mathbf{S}_i \cdot \mathbf{H}_i)] - \frac{\gamma\lambda_{\mathrm{t}}}{S^2}[\mathbf{S}_i \times (\mathbf{S}_i \times \mathbf{H}_i^{\mathrm{total}})] + \boldsymbol{\xi}_i, \tag{2.51}$$

where an effective field $\mathbf{H}_i$ acts according to spin vector $\mathbf{S}_i$ at site i. In this case, it is seen that the LLB equation of motion distinguishes between transverse and longitudinal forms of damping denoted by λ_{t} and λ_{l} respectively. It should also be noted that the transverse component considers an effective field $\mathbf{H}_i^{\mathrm{total}}$ that has thermal white noise applied to it via methods detailed in section 2.2.3. Finally, γ is the gyromagnetic ratio, and $\boldsymbol{\xi}_i$ refers to an additive stochastic noise term detailed in section 2.2.4. It is important to note that the effective field in this case includes a zero-field equilibrium spin polarization term defined in Evans *et al.* [65], in addition to its usual definition described in section 2.2.3. The purpose of this extra effective field component is to regulate the length of the magnetic moment, playing a similar role to the Landau Hamiltonian used in this thesis.

To get to the LSF-LLG form shown in equation 2.41, the LLB equation of motion can be rewritten substituting the vector triple product form $\lambda \mathbf{H}_i = \lambda\,[\mathbf{S}(\mathbf{S}_i \cdot \mathbf{H}_i) - (\mathbf{S}_i \times \mathbf{S}_i \times \mathbf{H}_i)]/S^2$ and $\lambda_{\mathrm{t}} = \lambda_{\mathrm{l}}$, giving the following [50]:

$$\frac{\partial \mathbf{S}_{\mathrm{LSF}}}{\partial t} = -\gamma(\mathbf{S}_i \times \mathbf{H}_i) + \gamma\lambda\mathbf{H}_i + \boldsymbol{\xi}_i, \tag{2.52}$$

which consolidates the methods used to obtain the LSF-LLG equation of motion seen in section 2.2.4.

2.2.7 The Monte-Carlo integrator

The Monte-Carlo integrator utilises a process whereby random sampling will provide a new spin state within a fixed unit sphere constrained to $|S| = 1$ to every spin in a system, and based on its free energy a probability evaluation takes place to determine if the random move is taken or rejected. This follows the definition that given enough Monte-Carlo steps, the probabilistic nature of all possible spin-vector configurations will emerge, according to a Boltzmann distribution. The basis for the algorithm and the probability with which moves are computed is given by [28]:

$$P = \exp\left(-\frac{\Delta E}{k_{\mathrm{B}}T}\right). \tag{2.53}$$

ΔE is the difference in energy for the spin states $\mathbf{S}_i$ and $\mathbf{S}_i'$. The sampling algorithm to determine $\mathbf{S}_i'$ at each timestep utilises a Gaussian distribution function which is described in the following equation [28]:

$$\mathbf{S}_i' = \mathbf{S}_i + f\sigma_{\mathrm{g}}\mathbf{\Gamma}, \tag{2.54}$$

where $\mathbf{\Gamma}$ defines a Gaussian distribution that has a width of 1 and a mean of 0 as a vector with x, y, and z components. The term σ_{g} determines the sampling space of the algorithm, and adaptive factor f is a factor used to adjust the size of the step taken as the simulation takes place to ensure that the system tends to a $50:50$ accept to reject ratio. A 50% acceptance rate is crucial in ensuring that true thermal equilibrium has been reached, which is a requirement ensured by a reversible and ergodic Monte-Carlo algorithm. Reversibility is demonstrated as the Boltzmann probability is evaluated via ΔE, and thus $P(\mathbf{S}_i \rightarrow \mathbf{S}_i') + P(\mathbf{S}_i' \rightarrow \mathbf{S}_i) = 1$. Ergodicity is also demonstrated, as all the spin states within the unit sphere are explorable [28]. After every timestep, the spin lengths quantity $|S|$ is normalised in this form of the Monte-Carlo scheme, which only includes transverse spin calculations. To calculate the adaptive factor f, the following equation is used:

$$f = \frac{0.5}{R_{\mathrm{reject}}}, \tag{2.55}$$

where the rate of rejection at each timestep is redefined, and is given by R_{reject}. In order to augment this to allow for longitudinal changes to be modelled, section 2.2.8 describes methods used for a longitudinal form.

2.2.8 The longitudinal Monte-Carlo integrator

The longitudinal Monte-Carlo integrator follows discussions from Pan *et al.* and Ellis *et al.* regarding a Monte-Carlo algorithm that uses the entirety of transverse and longitudinal sampling space to generate a sequence of spin changes [31, 50]. This can be done by appending the Landau Hamiltonian which regulates longitudinal moves to the conventional one, which has terms for exchange, anisotropy and applied fields. By sampling this collective Hamiltonian, it is evident that the energies calculated to evaluate moves according to the Boltzmann probability considers both longitudinal and transverse components. An additional change that was necessary, was to lift the unit sphere sampling constraint, which in the conventional Monte-Carlo restricted the spin length quantity to $|S| = 1$ via normalisation. The longitudinal trial move function is written as:

$$\mathbf{S}_i' = \mathbf{S}_i + f\sigma_g \mathbf{\Upsilon}, \tag{2.56}$$

where $\mathbf{S}_i$ defines the spin vector at site i, and $\mathbf{\Upsilon}$ defines a uniform sampling distribution of mean 0 and width 1, which affects the width of a sampling cone σ_g that adapts according to adaptive factor f. The vector $\mathbf{\Upsilon}$ has components for x, y, and z directions. The adaptive cone width is described in section 2.2.7, whereby the general idea is to maintain an accept to reject likelihood of around 50%, thereby adjusting the width of the sampled space to more easily achieve this metric. The exact form of the longitudinal Monte-Carlo integrator is highly debated due to some complexities encountered. Utilising a Gaussian distribution term as per the conventional Monte-Carlo no longer guarantees ergodicity, namely because via this form, sampling affects both longitudinal and transverse moves at the same time (sampling the total spin vector which is the product $\hat{\mathbf{S}}|S|$). This means that if only either the longitudinal or transverse phase spaces is at one point highly variate, while the other is not, a single regulation to the width of the sampling cone will not properly realise the required moves to be evaluated. The natural solution to this would be to create a form that decouples the moves, whereby the transverse and longitudinal cone sizes can be varied and adapted independently. A schematic of this is shown in figure 2.5. Splitting sampling like this while computationally much more efficient leads to another problem: the phase space measure of the probability evaluation function is no longer valid, as the modified phase-space (partly transverse and partly longitudinal) would require an adjustment to the form seen in equation 2.53. It is currently unclear what this formalism would entail, however uncovering the phase-space metric for split moves in the longitudinal Monte-Carlo would greatly benefit its efficiency [31].

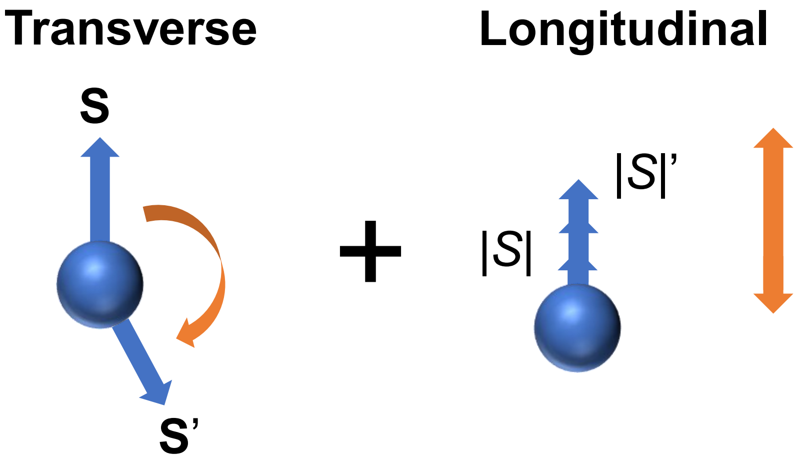

Fig. 2.5 Schematic diagram of allowing split Monte-Carlo moves in the LSF-MC integrator scheme. The separation of transverse and longitudinal motion would allow for independent control over both sampling functions.

2.3 Quantifying magnetisation properties

2.3.1 System magnetisation

The normalised macroscopic magnetisation of a system with atomistic discretisation can be quantified by summing all spin vectors and taking an average according to the equation

$$m = \frac{1}{n}\sum_{i}^{n} \mu_i \mathbf{S}_i, \tag{2.57}$$

where n is the total number of atoms in the system, and μ and $\mathbf{S}$ describes its magnetic moment and spin vector at site i. This metric is useful in obtaining the level of ordering or disordering present in a system. For example, for a ferromagnetic system approaching T_C, the summation of all spin vectors $\mathbf{S} \to 0$ occurs due to a summation of fully random $\mathbf{S}$ values from -1 to 1. Additionally, when under the influence of an effective field, a paramagnetic system would react and would accordingly lead to a change in spin direction towards $\mathbf{H}$, which can be quantified as an average of the system spin vectors. When calculating disordering due to T_C, the normalised magnetisation length quantity $|m|$ can be calculated to determine the magnetic ordering state compared to saturation using

$$|m| = \frac{|\sum_i \mu_i \mathbf{S}_i|}{\sum \mu_i}. \tag{2.58}$$

At a fully ordered state, $|m| = 1$, while for fully disordered this would yield $|m| \approx 0$. Outside of conventional cases where the length of the vector $|S|$ is not adjusted and remains as $|S| = 1$ throughout, unlocking longitudinal degrees of freedom for the spin vector quantity affects the validity of this measure. In the examples covered in chapter 4, it is shown that without the right longitudinal energy reference state, it is possible to have $|m| > 1$ at equilibrium erroneously, which would yield incorrect calibration with respect to the value at the Curie temperature.

2.3.2 Sublattice susceptibility

In order to determine a ferromagnetic system's material dependent magnetic properties past the paramagnetic regime T_C, the calculation of magnetic susceptibility is often employed. This calculation determines the tendency for the system to re-align towards a new general spin direction given a field. At the Curie temperature, this quantity peaks as the paramagnetic state overcome by high temperatures affords the possibility of re-aligning with for example an applied field, rather than orienting according to its own magnetisation. This is known as the Curie-Weiss law, and is described by

$$\chi = \frac{C}{T - T_\mathrm{C}}, \tag{2.59}$$

where χ is the material susceptibility, and C is the material specific Curie constant. This relationship determines that there is a susceptibility peak at the exact moment when $T = T_\mathrm{C}$, and is minimal in temperature regions outside of this region. In order to make use of this calculation in the atomistic regime, and to offer material-specific discretisation as to susceptibility calculations, the longitudinal sublattice susceptibility equation is employed, and is given by [68, 69]:

$$\chi_l = \frac{\sum_i \mu_i}{k_\mathrm{B} T} \left(\langle |m|^2 \rangle - \langle |m| \rangle^2 \right). \tag{2.60}$$

This form of the susceptibility calculations sums and averages the susceptibility measures in all sublattices, which is dependent on the magnetisation of the system denoted by the $|m|$ parameter. The mathematical expression used to determine this quantity follows the simple rule that the $\left(\langle |m|^2 \rangle - \langle |m| \rangle^2 \right)$ term describes the variance of magnetic states between spins, which in the paramagnetic state would be maximal due to fully random orientation. At this point, the value for χ would also be maximal. When there is minimal variance when $T < T_C$, χ also takes on a minimal value.

2.4 Summary

This chapter has covered the details surrounding the fundamental interactions of the spin calculations being taken into consideration in the atomistic frameworks required for modelling HAMR. This includes the fundamental interactions of exchange, anisotropy, applied field, and moment size contributions via the Landau Hamiltonian. While the Landau Hamiltonian allows for flexibility of customising the energy surface that regulates changes to the size of the spin length to allow for a more physical representation of magnetic moments, it comes with some disadvantages. Firstly, DFT calculations are required for computing them, and they become invalid even if the system sees small variations to its total Hamiltonian. Secondly, its currently presented form in even powers of $|S|$ is unclear to be the best approach, as in theory odd powers could also be included in the expansion.

The groundwork for the conventional integrator schemes was discussed, which allows for development of integrator schemes that are compatible with the newly introduced longitudinal dynamics model which has introduced changes to moment size via the Landau expansion. It is important to highlight that the uncertainty about these integrator schemes is the forced setting of the transverse and longitudinal damping constants to be the same. To fully investigate this effect, a comparison of the results to the LLB integrator would be useful to investigate in future work.

3

Atomistic simulations on the effects of grain size in HAMR

3.1 Background

Heat Assisted Magnetic Recording (HAMR) is a method of magnetic data recording that involves heating local grains involved in the writing process, writing a bit sequence, and then allowing it to cool. The primary advantage of this method as compared to conventional magnetic recording, where temperature-dependent magnetisation is not taken advantage of, is it allows for a reduction in grain sizes, which means constructing recording media with higher areal densities becomes viable [16, 70]. It is paramount for such technologies to be developed, as the data density limits of conventional magnetic recording are soon being realised. Additionally, increasing quantities of data are being used on a daily basis internationally, and thus HAMR exists as a way to alleviate this demand. FePt demonstrates a reduction in its uniaxial anisotropy as temperature increases, which is a crucial property to ensure that data can be written without requiring impossibly large write fields. At low temperatures, FePt maintains a high magnetocrystalline anisotropy, which ensures that erroneous magnetic switching is very unlikely to occur. When data is being written, bringing the local region to the Curie temperature T_C reduces the anisotropy and by extension its coercivity, making writing data viable [71]. In the $\mathrm{L1_0}$ phase, FePt has a tetragonal crystal structure, illustrated in figure 3.1, composed of exclusive layers of Fe and Pt sites situated on top of one another, giving it a high anisotropy of $K \approx 10^7\ \mathrm{J/m^3}$. Pt belongs to the $5d$ series of elements giving it a large spin-orbit coupling, while Fe being in the $3d$ series perturbs the Pt sublattice through exchange splitting [30]. As a general rule, a high magnetocrystalline anisotropy is achieved via similar combination of $5d$ and $3d$ elements.

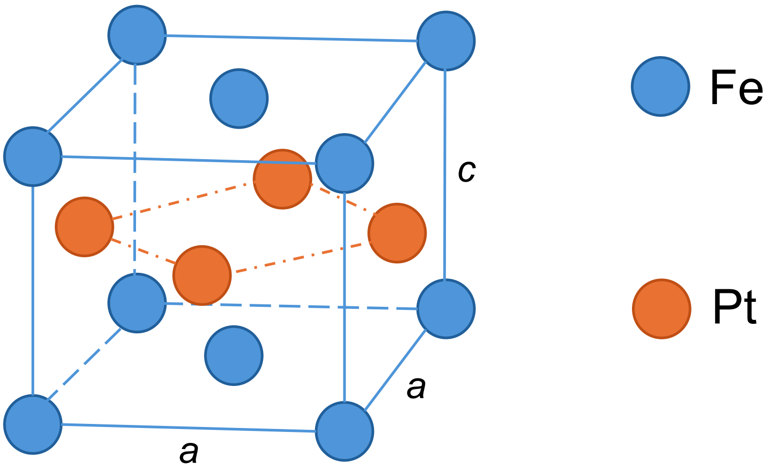

Fig. 3.1 The structure of $L1_0$ FePt consists of exclusive layers of Fe and Pt, with a high uniaxial anisotropy preferring the stacking direction.

A crucial aspect of designing magnetic recording media is to investigate how much the size of the magnetic grains can be reduced by for the largest possible areal density, before a significant loss of stable recording capability is lost. This is a fundamental issue seen in magnetic recording, and has been named as the magnetic recording trilemma (or quadrilemma when looking at HAMR) [13, 72, 73]. Small grains are needed to maximise areal density, leading to unwanted loss of magnetisation, which requires a higher anisotropy, meaning larger write fields are necessary to flip the magnetisation direction. In HAMR, it is additionally required that the high temperatures introduced do not accidentally affect the magnetic state of the grains when magnetic switching is not taking place. Identifying appropriate grain dimensions in HAMR recording media stands out as a primary area of contention, due to how many factors need to be balanced simultaneously as explained by the quadrilemma.

The research presented in this chapter aims to cover ground on the technicalities of atomistic simulations methods of HAMR, and to further investigate the use cases of $L1_0$ FePt in HAMR by demonstrating key material properties that can be exploited to aid the efficiency of such devices. Atomistic simulations have allowed preliminary investigations into temperature-dependent magnetisation calculations, which has found the Curie temperature of $L1_0$ FePt to be $T_C \approx 700$ K. Following this, it was verified that the expected exponent in

$K(T) \propto M(T)^L$ was recovered, where $L \approx 2.1$, which is a metric used to quantify temperature-dependent anisotropy, a key feature that makes $\mathrm{L1_0}$ FePt a viable candidate for HAMR purposes. Cylindrical grains of $\mathrm{L1_0}$ FePt were set up for atomistic simulations to determine switching dynamics under HAMR conditions. By replicating the effects of a laser pulse during the writing process, an applied Gaussian heat pulse raised the system temperature until the spin moments were disordered, after which a magnetic field attempted to switch the direction of the spins.

3.2 Theory

3.2.1 Atomistic Pt-modified Fe parameters

The conventional formulation used to atomistically model $\mathrm{L1_0}$ FePt was described in Mryasov *et al.*, which assumes that the Pt moments are much smaller in magnitude than the Fe ones, and thus the Hamiltonian described is done so in solely Fe degrees of freedom [30]. The behaviour of Pt can be clearly identified using the ratio of a given exchange field H normalized using its maximum in the ferromagnetic state, H_0, to give $H_{\mathrm{norm}} = H/H_0$. Increasing H_{norm} from 0 to 1 is what induces a spin moment in Pt sites, while Fe has the same persistent moment throughout. From this it can be deduced that FePt consists of localised Fe moments, and delocalized Pt sites. The Hamiltonian for the Fe sites takes the following form

$$\mathscr{H}_{\mathrm{localized}} = \sum_{i<j} J_{ij}^{\mathrm{1\text{-}nn}} \mathbf{S}_i \cdot \mathbf{S}_j - \sum_i k_{\mathrm{Fe}} (\mathbf{S}_i^z)^2. \tag{3.1}$$

Since the Pt moment varies greatly as it goes from a disordered to an ordered state, the Stoner model can be used to describe the total energy of Pt sites, and is described by [30, 74]:

$$E_{\mathrm{delocalized}} = \int_{-\infty}^{E_{\mathrm{F}}} d\varepsilon [n^{\mathrm{up}}(\varepsilon) + n^{\mathrm{down}}(\varepsilon)]\varepsilon - \frac{1}{2} I \mathbf{m}^2 \approx \tilde{I} \left(\frac{\mathbf{m}}{m_0} \right)^2, \tag{3.2}$$

where the first term represents the Stoner expression to compute the total energy based on the density of states, $\mathbf{m}$ and m_0 are the instantaneous and equilibrium moments respectively, and I is the intra-atomic exchange, while $\tilde{I} = \frac{1}{2} I (m_0)^2$. Following the *ab initio* calculations done in Mryasov *et al.*, the Pt moment can then be related to the exchange field from Fe, and the Pt susceptibility given the equation [30]:

$$\mathbf{m}_{\mathrm{Pt}} = \chi_{\mathrm{Pt}} \mathbf{H}_{\mathrm{Fe}}, \tag{3.3}$$

where χ_{Pt} refers to Pt susceptibility, and is a measure to define how easily influenced a material's magnetisation is given an effective field, in this case the effective field produced by the Fe exchange field, given by $\mathbf{H}_{\text{Fe}}$. The Pt moment can further be expressed in a normalised form according to

$$\left(\frac{\mathbf{m}}{m_0}\right) = \frac{\chi_{\text{Pt}}}{m_0}\sum_i J_i \mathbf{S}_i. \tag{3.4}$$

It is crucial to note that this form now links a relationship between the Pt spin vector and the Fe spin vector, S_i, and the Fe exchange field, J_i. The effective exchange for FePt can then be written as shown [30]:

$$J_{ij}^{\text{eff, 1-nn}} = J_{ij}^{\text{1-nn}} + \tilde{I}\left(\frac{\chi_{\text{Pt}}}{m_0}\right)^2 \sum_\nu J_{i\nu} J_{j\nu}. \tag{3.5}$$

Decomposing the anisotropy terms for both Fe and Pt, in solely Fe degrees of freedom gives a single-ion and two-ion anisotropy contribution, given by the following equations [30]:

$$d_i^{(\text{1-ion})} = k_{\text{Fe}} + k_{\text{Pt}}\left(\frac{\chi_{\text{Pt}}}{m_0}\right)^2 \sum_\nu J_{i\nu}^2, \tag{3.6}$$

$$d_i^{(\text{2-ion})} = k_{\text{Pt}}\left(\frac{\chi_{\text{Pt}}}{m_0}\right)^2 \sum_\nu J_{i\nu} J_{j\nu}, \tag{3.7}$$

where ν is a Pt site within its own sublattice. Following this, a full Hamiltonian can be constructed including a combination of all localized and delocalized terms described in the following:

$$\mathscr{H}_{\text{FePt}} = \sum_{i<j} J_{ij}^{\text{eff, 1-nn}} \mathbf{S}_i \cdot \mathbf{S}_j - \sum_i d_i^{(\text{1-ion})} (\mathbf{S}_i^z)^2 - \sum_{i<j} d_i^{(\text{2-ion})} \left(\mathbf{S}_i^z \mathbf{S}_j^z\right). \tag{3.8}$$

This spin Hamiltonian describes L1_0 FePt spin dynamics in purely Fe degrees of freedom, via incorporating the effects of the delocalized Pt moments into the coefficients. While this chapter uses this form of the Hamiltonian, a broader comparison can be drawn if the Fe and Pt moments are modelled individually in their own degrees of freedom. Further chapters in the work presented will highlight the introduction of atomistic simulations via both Fe and Pt degrees of freedom, utilising the tendancy for Pt moments to fluctuate longitudinally, rather than transversely.

3.2.2 The conventional FePt Hamiltonian

The following equation describes the energies of FePt systems with respect to the spin unit vectors $\mathbf{S}_i$ and $\mathbf{S}_j$, representing sites i and j respectively:

$$\mathscr{H} = \sum_{i<j} J_{ij}^{\text{1-nn}} \mathbf{S}_i \cdot \mathbf{S}_j - k_\text{u} \sum_i (\mathbf{S}_i \cdot \hat{\mathbf{e}}_i)^2 - \mu_s \sum_i \mathbf{B} \cdot \mathbf{S}_i, \tag{3.9}$$

where $J_{ij}^{\text{1-nn}}$ represents the Heisenberg exchange coupling, which is restricted solely to nearest neighbour interactions. k_u is the uniaxial anisotropy constant with $\hat{\mathbf{e}}_i$ representing the system's easy axis. $\mathbf{B}$ describes the energy changes with regard to an applied magnetic field, with atomic spin moment μ_s, which is quantified as $\mu_s = 3.62\ \mu_\text{B}$ per atom for the Fe sites in L1_0 FePt [28, 50]. It is important to note that this value of μ_s corresponds to the effects of both Fe and Pt, as only Fe degrees of freedom are modelled. It should be noted that dipolar fields are not considered in these calculations. The exchange energy term is defined by a coupling constant between two spin sites and originates from overlapping electron orbitals. The following describes the equation used to calculate $J_{ij}^{\text{1-nn}}$ using the mean-field approach:

$$J_{ij}^{\text{1-nn}} = \frac{3k_\text{B}T_\text{C}}{\varepsilon z}, \tag{3.10}$$

where k_B is the Boltzmann constant, T_C is the Curie temperature, ε is the spin-wave correction factor, which is given as $\varepsilon = 0.719$. z is the number of nearest neighbours, giving 6 for the calculations in this chapter, as the non-magnetic Pt sites are disregarded as a degree of freedom. Due to anisotropic exchange in FePt, solely using equation 3.10 would yield the value for exchange energy along [100] and [010] directions (corresponding to J_x and J_y). To get J_z, one must take the contributions of two-ion anisotropy into account, given by:

$$J_z = J_x - \frac{k_\text{2-ion}}{z}, \tag{3.11}$$

where $k_\text{2-ion}$ can be obtained from approximation that can be deduced from Mryasov *et al.* that $k_\text{2-ion} \approx 10k_\text{u}$ [30]. Subsequently, the following describes how k_u is calculated:

$$k_\text{u} = \frac{K_\text{u}V}{n}. \tag{3.12}$$

K_u defines the macroscopic anisotropy constant, n is the number of atoms in each unit cell, and the volume of the unit cell $V = aac$, given a compression along [001], with an otherwise uniformly spaced crystal. For L1_0 FePt this is $a = 3.861$ Å and $c = 3.788$ Å [75]. Utilising this calculation, a value of $k_\text{u} = -6.87 \times 10^{-23}$ J (given that $K_\text{u} = 10^7$ J/m^3) was obtained.

It should be highlighted that k_{u} is an in-plane anisotropy contribution, unlike $k_{2\text{-ion}}$ which is out of plane. Using equations 3.10 - 3.12, the exchange constants are calculated to be $J_x = J_y = 6.30 \times 10^{-21}$ J and $J_z = 6.42 \times 10^{-21}$ J. In these methods used, the single-ion anisotropy term is considered in the Hamiltonian via equation 3.9, and the two-ion term is deconstructed to be a modification to the isotropic exchange values. This method of incorporating the two-ion anisotropy into the exchange is purely for computational efficiency.

3.3 Simulation methods

3.3.1 Crystal structure generation

To construct grains to simulate atomistic temperature-dependent magnetisation dynamics, the system is required to have an exchange list that states the position of each spin moment relative to one another, and the exchange energies respective to their neighbours. Figure 3.2 demonstrates a schematic for how $L1_0$ FePt systems are constructed as a simulated system. Starting with a simple 4 atom structure (labelled by atoms 1-4 in (a)) a repeatable unit cell can be constructed that can be added to indefinitely until a desired system has been achieved. It should be noted that the Pt atoms exist solely for visualisation in these simulations, and otherwise manifest their influence via changes to the Fe-Fe exchange parameters. Once a simple unit cell is constructed, (b) shows the addition of neighbouring unit cells being added, and the resulting exchange interactions J_x, J_y, and J_z that occur between each Fe site with a nearest neighbour. The model employed for Heisenberg exchange for the calculations in this chapter simply extend to the first nearest neighbour, however it should be noted that it this simplification is not exactly reciprocated physically [30, 76].

Unit cells are added to the system until a cuboid with sides matching the diameter and height of the grain is reached, at which point a cylindrical shape is cut out, resulting in a single grain as seen in figure 3.3.

3.3.2 Simulation of HAMR media

To construct more large scale magnetic recording media, granular media are constructed by first starting with randomly placed points, which will be referred to as seeds. From here, the bisector between each seed point is calculated, which defines each grain's boundary. This is known as a Voronoi tessellation, and is employed as an approach to create randomised grain sequences of varying sizes. To aid with realism, the grains are spaced apart by 0.5 nm, and rounding is applied to them so they more closely resemble circular structures (when looking

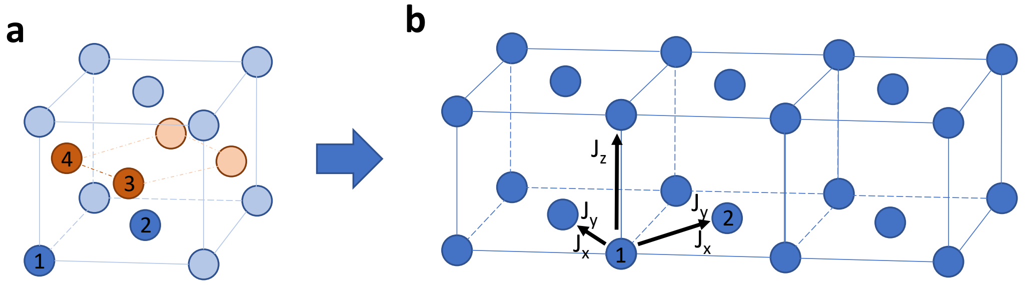

Fig. 3.2 (a) shows the purely visual construction of the $L1_0$ FePt unit cell, where Pt (orange) is later stripped in (b) as only Fe (blue) degrees of freedom are being considered. Additionally, the logic behind the exchange list can be seen to include Fe-Fe interactions, including for spins in neighbouring cells, via J_x, J_y, and J_z.

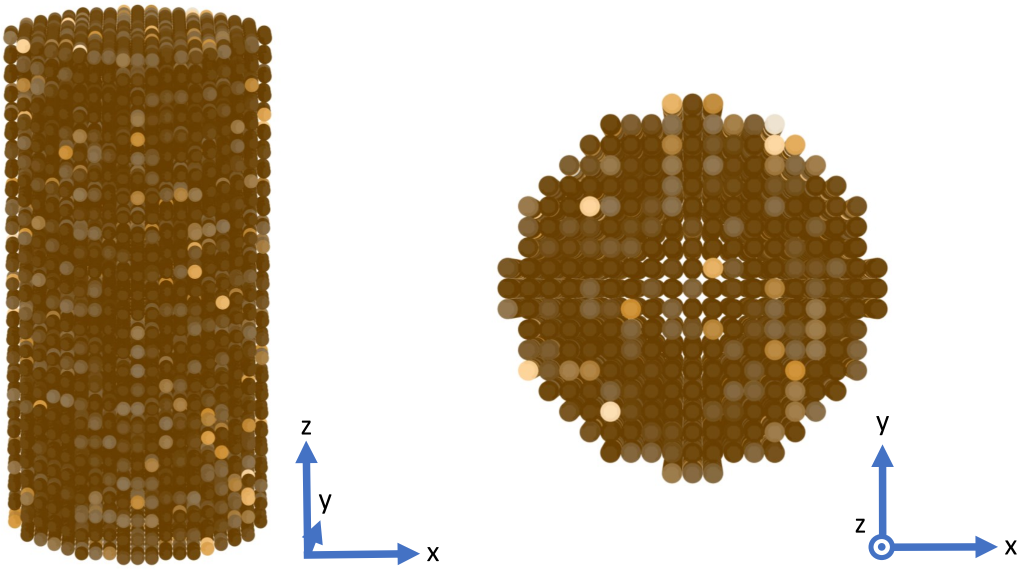

Fig. 3.3 The final product of an atomistically generated grain consisting of $L1_0$ FePt. Each dot rendered corresponds to an individual atoms with its own spin degrees of freedom.

at them from above) rather than having multiple jagged edges. Although separation between grains depends greatly on the average grain size, a separation of 0.5 nm was found to be appropriate [77, 78]. In future work, it would be useful to investigate a range of separation distances. A sample tessellation generated is shown in figure 3.4. On the granular media, a

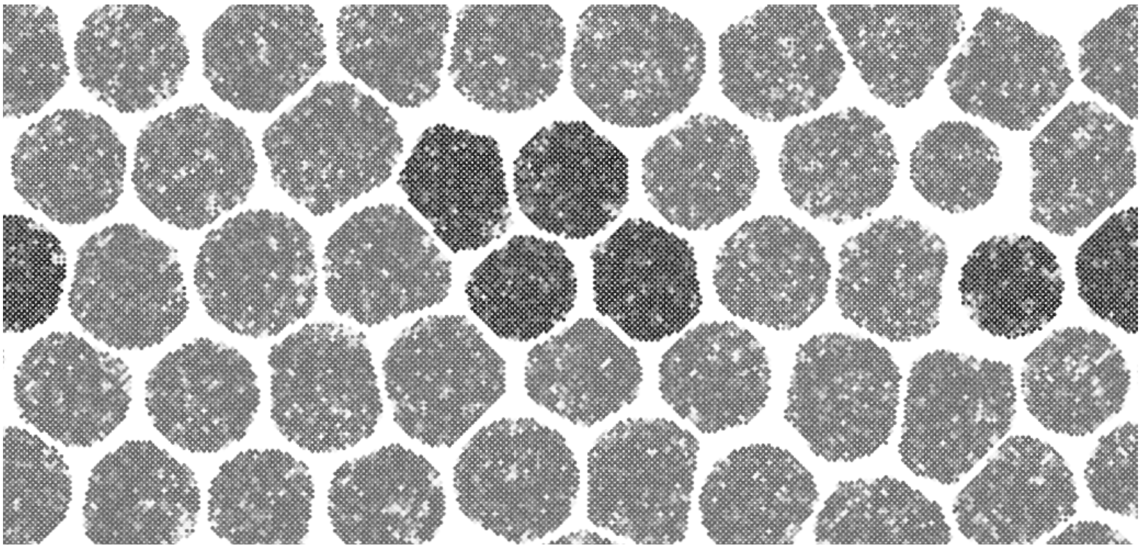

Fig. 3.4 An example of grains generated using Voronoi tessellation used for simulating HAMR atomistically. It can be seen that the random generation creates a size variance between different grains.

bit sequence of constant size per bit is then imprinted via the application of a magnetic field, and a local temperature pulse according to a Gaussian distribution. As the grains heat up, the moments become more disordered, eventually leading to a reversal in spin direction. To recognise that data has successfully been written as a result of HAMR, a cluster of contiguous grains on the media will have a net spin direction which determines the sign of the bit. The benefit of having smaller grains (and thus a larger areal density) is the ability to use grain clusters to represent a bit that are overall smaller than what can be achieved with larger sizes.

3.4 Results and discussion

3.4.1 Verifying the temperature-dependent properties of FePt

A key property required to fulfil the conditions of HAMR is the reduction of temperature-dependent anisotropy. This ensures that when the recording head produces a magnetic field, the random orientation of the moments are easily aligned with the field. Simulations that calculate normalised magnetisation and the torque of the system can be used to investigate temperature dependence.

The constrained Monte-Carlo algorithm (CMC) [79] is utilised to compute the instantaneous torque of a system with respect to temperature, which arises by setting an angular constraint on the spins. The CMC utilises a system of sampling that acts on two spins at the same time, $\hat{\mathbf{S}}_i$ and $\hat{\mathbf{S}}_j$. The compensation spin, $\hat{\mathbf{S}}_j$ is rotated such that the arbitrary constraining angle (set to $\theta = 45°$ in this case) gives rise to no change in the total magnetisation of the system. Meanwhile, spin $\hat{\mathbf{S}}_i$ is rotated as per the standard Monte-Carlo methods, which uses a normally distributed sampling space on a unit sphere. This ensures that the spin torque calculations can take place, while simultaneously keeping the normalised magnetisation against temperature relationship unchanged. The probability evaluation of the constrained Monte-Carlo according to the Boltzmann probability is calculated according to the following expression [79]:

$$P = \min\left[1, \left(\frac{M_z}{M_z'}\right)^2 \frac{|\hat{\mathbf{S}}_{jz}|}{|\hat{\mathbf{S}}_{jz}'|} \exp\left(-\frac{\Delta E}{k_\mathrm{B}T}\right)\right], \tag{3.13}$$

where $\exp(-\frac{\Delta E}{k_\mathrm{B}T})$ is the Boltzmann probability factor, which is further modified by a geometric correction dependent on the z component of the magnetisation and spin vector, M_z and $\hat{\mathbf{S}}_z$ respectively.

To compute the temperature-dependent anisotropy of FePt, simulations were done using the CMC algorithm, with the condition of the constraint angle set to $\theta = 45°$ from the easy axis, creating a torque τ. As temperature increases and the system enters an increasingly disordered state, the following equation can be used to calculate the instantaneous torque:

$$\tau = \sum_i \mu_i \mathbf{S}_i \times \mathbf{H}_i. \tag{3.14}$$

To cover a large range of grain dimensions, the temperature-dependent magnetisation dynamics were calculated on grains with diameters between 3 nm to 12 nm. For each diameter, a height of 5 nm and 10 nm was considered. The temperature dependence was introduced by varying the system temperature from 0 K to 1000 K in 5 K increments, with 50000 timesteps per temperature step. 10000 equilibration timesteps were also added before the start of each new temperature regime, to allow for the system to fully relax before recording magnetisation data. In order to more appropriately represent experimental temperature scaling, a rescaling function was used to regulate the simulated spin temperature according to an empirical constant $\alpha = 1.75$ according to [80]:

$$\frac{T_\mathrm{sim}}{T_\mathrm{C}} = \left(\frac{T_\mathrm{exp}}{T_\mathrm{C}}\right)^\alpha, \tag{3.15}$$

where T_sim is the simulated temperature, and T_exp its experimental equivalent. Figure 3.5 describes the temperature-dependent magnetisation found in $\mathrm{L1_0}$ FePt, obtaining a bulk $T_\mathrm{C} = 704.8$ K. This is the point at which the mean magnetisation length goes to zero, as the spins are in a fully disordered state. To verify the scaling in this data is appropriate, normalised anisotropy energy against magnetisation was plotted on a logarithmic scale to get back the value of $L \approx 2.1$, where $K(T) \propto M(T)^L$ [32, 81]. This data was fitted according to the following expression, which describes the temperature-dependent magnetisation via empirical constant α and fitting parameter β:

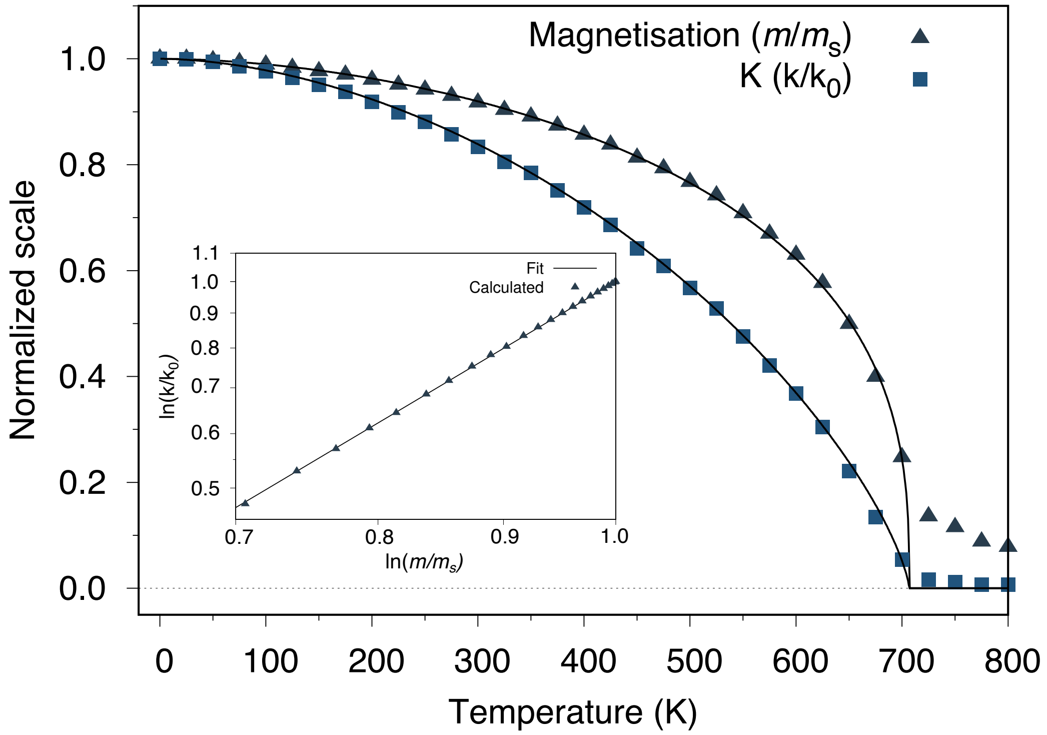

Fig. 3.5 Normalised Magnetisation against temperature curve for $L1_0$ FePt. The calculated fit using equation 3.16 gives a value of T_C = 704.8 K, with $L \approx 2.1$. The temperature-dependent anisotropy demonstrated is a key property of being able to use FePt for HAMR.

$$m(T) = \left(1 - \left(\frac{T}{T_C}\right)^{\alpha}\right)^{\beta}. \tag{3.16}$$

Table 3.1 shows the T_C and temperature-dependent anisotropy data for the variety of grain dimensions investigated. There is a clear increase in T_C as the grain diameter increases which is in expectation with the finite-size scaling law which demonstrates that larger systems will tend towards a higher T_C (where this scaling eventually falls off), as the ratio of sites on the surface to sites in the bulk decreases with increasing volume [82–85]. This is because the surface sites will always be more weakly exchange-coupled due to a lack of nearest neighbours, thus a lower exchange contribution will lead to a smaller T_C. It should be noted finite-size scaling laws compete with a factor seen in Lyberatos *et al.*, where it is shown that an additional contribution to grain T_C values is an elongation factor $H_\mathrm{grain}/D_\mathrm{grain}$ which shows that the ratio of grain height to its diameter drastically alters its temperature-dependent magnetisation scaling properties [86]. The temperature-dependent anisotropy scaling shows clearly that given a fully disordered system near T_C, the sum in equation 3.14 converges to 0, and thus a total reduction of the anisotropy component follows. In the writing process, this highlights the importance of getting to a high enough temperature so that data can be more easily imprinted before cooling begins. Finally, it was found that the anisotropy scaling value L remains stable as the dimensions of the grain increases, showing that the temperature-dependent anisotropy of the simulated L1_0 FePt systems have been implemented appropriately, as the value $L \approx 2.1$ is recovered.

Size [Diameter (nm), Height (nm)]	T_C (K)	L
3, 5	668.7	2.128
3, 10	672.8	2.173
5, 5	676.2	2.142
5, 10	678.6	2.149
7, 5	678.3	2.151
7, 10	684.6	2.154
9, 5	683.9	2.162
9, 10	686.1	2.161
12, 5	684.0	2.173
12, 10	687.3	2.169

Table 3.1 Summary of data obtained for all simulated grain sizes for K against T simulations. A distinct size dependency can be observed in the Curie temperature results obtained, which follows expected behaviour.

3.4.2 Magnetic switching of FePt grains

To gain a nanoscale understanding of the physical phenomena at play during the magnetic recording process, the atomistic simulation of single grains undergoing the switching process is presented, where the small variation in grain sizes can be more easily investigated.

At the Curie point, FePt grains lose their temperature-dependent anisotropy, and the spin moments become disordered, which allows them to easily yield to an applied field. The goal is to write data via an applied field, and to induce the spins into changing direction to that of the applied field, and for the grain to still maintain its newly defined spin configuration some time after it begins to cool. There is a competing force at play here; if the temperature-dependent anisotropy is not reduced enough, or in the case of larger system, the applied field is not large enough to reverse the direction of every spin in the system, a reversal mechanism can override the intended write direction. By atomistically modelling L1_0 FePt grains, different system dimensions can be put through the writing process to determine what sizes show the most efficient switching pathways. The calculations done in this chapter utilised the atomistic LLG integrator, which is detailed in chapter 2. It was parametrised with $\Delta t = 1$ fs, which is shown to be close to convergence for this integrator scheme [28]. As an extension to this work, it would be beneficial to compute the grains' instantaneous magnetisations after a fixed number of timesteps, while varying Δt. This would determine how small the timestep would have to be for each system in order to reach a converged result, where it should be noted that smaller timesteps tend to achieve greater accuracy.

To simulate the conditions of HAMR, a Gaussian thermal pulse is applied to induce thermal excitations. This comes in the form given by the equation

$$T(t) = T_a + [T_{\text{peak}} - T_a]F(t), \tag{3.17}$$

where $T(t)$ represents the time dependent temperature gradient, with $T_a = 300$ K, which is the ambient room temperature. The peak temperature is $T_{\text{peak}} = 700$ K, equivalent to the Curie temperature of L1_0 FePt. F(t) is represented according to equation:

$$F(t) = \exp\left[-\left(\frac{t - 3t_{\text{pulse}}}{t_{\text{pulse}}}\right)^2\right], \tag{3.18}$$

which defines a temperature maximum at $3t_{\text{pulse}}$, with a standard deviation of $\sqrt{2}t_{\text{pulse}}$ [27]. The system also assumes a persistent write field of 1 T in the [00-1] direction, which is persistent in space and time. The calculations take place over 600 ps, with peak temperature at 300 ps.

Figure 3.6 shows the temperature pulse and switching profiles for a 5 nm diameter and 10 nm height grain, which clearly demonstrates instability in the switching process. The renders of the grain at the 50 ps, 300 ps, 420 ps, and 570 ps marks shows a domain wall process occurring, whereby the grain is divided into two sections that oppose each other's magnetisation direction, leading to a fluctuating change in the overall spin direction [87–89]. In general, domain walls more consistently formed in systems with more pronounced elongation, or increased volumes. This is because larger magnetic systems have a higher chance of forming segregated spin clusters that prefer certain orientations over others. More specifically, this means that if the system size goes beyond the system's exchange length, the nucleation of domain walls becomes a possibility [90]. In order for the domain wall to be overcome, the applied field must be strong enough to re-orient the domains even after beginning to cool. It is necessary to note that these fluctuations are detrimental to the reliability of HAMR processes, as it increases the rate of error when recording is taking place. Although in this case the thermal pulse coupled with the write field was enough to eventually switch the system, using the same grain with a write head that travels faster (leading to a smaller t_{pulse}) could cause significant issues in writing data. Because of this, grain dimensions play a delicate role in striking a balance with all components of the magnetic recording quadrilemma.

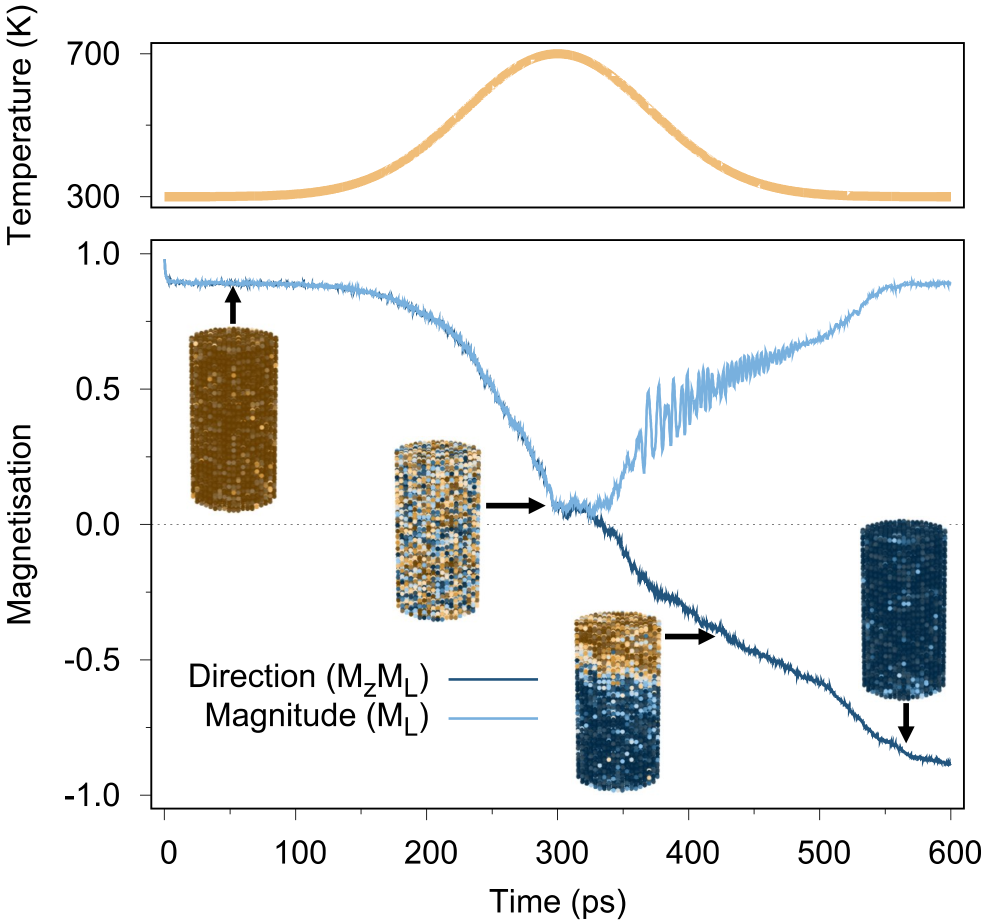

Fig. 3.6 Magnetisation against time data showing unstable magnetic switching. A render was generated at 350 ps seen next to the plot showing a domain wall process, which affected the way in which magnetic switching takes place. The domain wall described occurs at the $t = 420$ ps mark, and is distinctly identified by the light area towards the middle section of the grain which is at the boundary of the blue (spins with changed magnetisation) and brown (spins with their original magnetisation). This is for a grain of size 5 nm in diameter and 10 nm in height.

An additional rendered example is seen in figure 3.7, whereby a smaller grain ($D_{\text{grain}} = 5$ nm, $H_{\text{grain}} = 5$ nm) to what is seen in 3.6 demonstrates greater efficiency in the switching process, denoted by much shorter timescales to enter a fully switched state. The smaller spin volume also contributes via having a lower T_C, which contributes to entering the fully paramagnetic state much more quickly, leading to earlier switching.

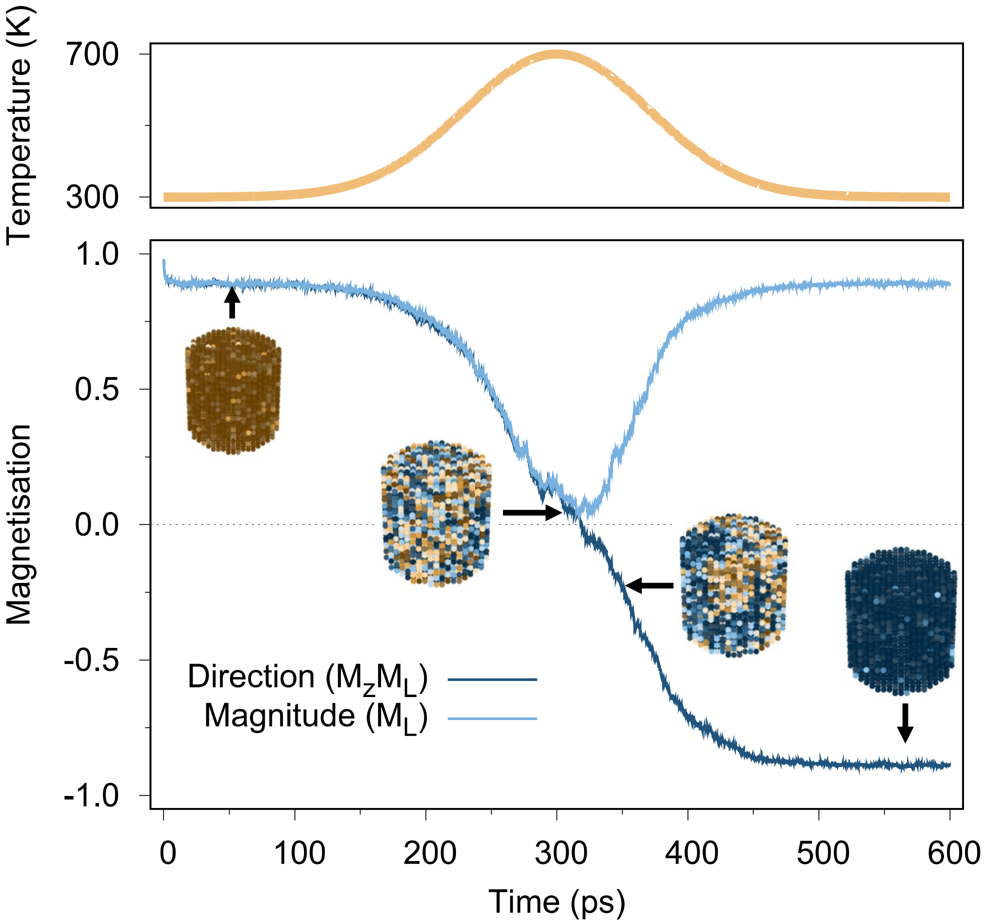

Fig. 3.7 Simulation data for a grain of 5 nm diameter and 5 nm height undergoing switching due to a thermal pulse and an applied field of 1 T. The size of the system is small enough for the thermal pulse to overcome the ordered spin state, and thus their direction reverses with the application of the field.

Figure 3.8 demonstrates the largest grain dimensions tested undergoing the effects of a thermal pulse, and a magnetic switching field in an attempt to reverse its spin orientation. In this case, the large spin volume hinders its ability to take on the new spin direction, as the proportionately smaller exchange length prevents any switching from occurring. As the system cools past the peak temperature, the temperature-dependent anisotropy recovers, solidifying its previous spin orientation once again.

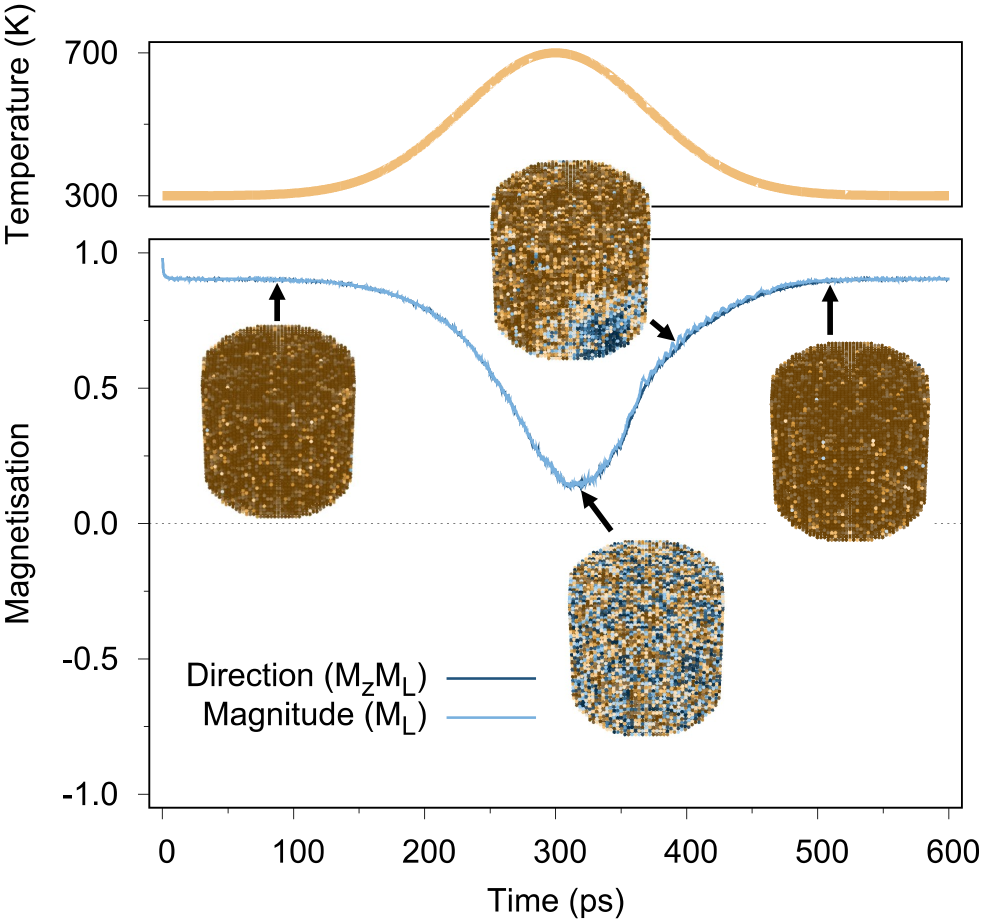

Fig. 3.8 Single grain ($D_{\text{grain}} = 12$ nm, $H_{\text{grain}} = 10$ nm) switching whereby the size of the system is too large for the thermal field to overcome the ordered state of the spins, and then to reverse their direction with the applied field.

Figures 3.9 and 3.10 shows various grains switching. In the 3-5 nm diameter variants, switching took place with a clear transition between the magnetisation directions reversing, albeit in the case where the grain aspect ratio is highly unusual at $D_{\text{grain}}/H_{\text{grain}} = 3/10$. Recalling the magnetic recording quadrilemma [73], switching occurs in systems where the temperature-dependent anisotropy scales adequately with the specifications of the laser pulse, with the system having a strong enough magnetisation as it cools that it is able to re-orient along a newly defined direction according to the applied field. For grain diameters 3-5 nm with height fixed at 5 nm, the grain size is viable such that no significant domain walls form, allowing for a straightforward switching profile. At the larger volumes and more inconsistent aspect ratios, the significant fluctuations in the grain magnetisation brought on by domain wall processes become evident. While it can be said that the 5 nm height variants for 7 nm and 9 nm diameter grains demonstrate switching capability, the timescales required for the grain to enter a completely switched state becomes problematic, as for example a faster laser pulse, or a less consistent field would in a lot of cases cause backswitching as the grain cools. This is denoted by significant fluctuations even after 200 ps post the temperature peak. In the case of the 12 nm grains, no evidence of switching was observed, and thus would not be able to facilitate HAMR. The switching process between grain sizes also depends significantly on their ability to reach a fully disordered state as measured by their T_C, thus as a general trend larger grain sizes may not enter a fully paramagnetic state as compared to their smaller counterparts.

The complexity behind the switching mechanisms of FePt grains is significant, given that the forces of the magnetic recording quadrilemma constantly influencing the temperature-dependent magnetic capabilities of the investigated systems. Additionally, from the results found it can be seen that the relative size of grains significantly influences both T_C and switching viability, given the effects of anisotropy and exchange, and the appearance of domain wall mechanisms respectively. It should be noted that in these calculations, T_max was kept constant for all grain sizes, regardless of the changes in their T_C. In reality, it would be necessary to vary T_max based on what grain geometries are being used. While the Mryasov model of re-parametrising Fe sites to have considerations of Pt sites being nearby has given significant insight into modelling HAMR atomistically, a further evolution of the treatment of Pt is required, such that the Pt degrees of freedom are also modelled. This is introduced in chapter 4, applied to FePt in chapter 5, and then used in switching and HAMR calculations in chapter 6. Finally, To gain a clearer picture of the full scale of the switching mechanism, grains were assembled into a magnetic recording medium to atomistically model the data writing process via HAMR.

3.4.3 Fully atomistic HAMR

Verifying the single grain dynamics atomistically provides crucial insight into the way in which exchange and anisotropy govern the process of switching. In order to provide a full scale result that shows the practicalities of implementing FePt grains for the purposes of reading and writing data, fully atomistic HAMR simulations were done on a variety of grain dimensions.

Figure 3.11 shows the result of a bit sequence being written onto numerous 200 nm by 50 nm recording tracks, populated with grains of fixed height 5 nm, and diameter varying between 3-8 nm. At 3 nm, the small anisotropy field is easily overcome by the temperature

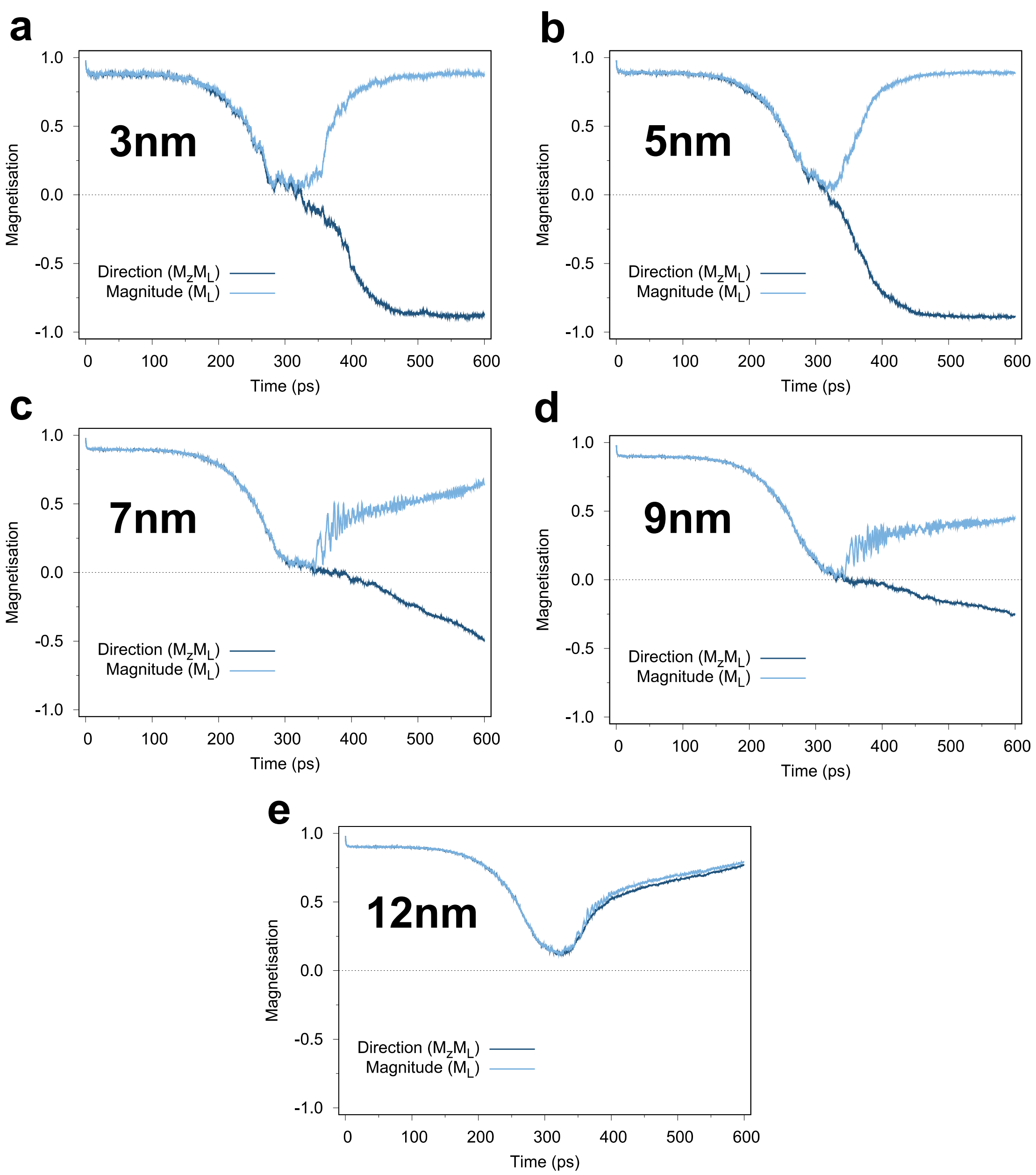

Fig. 3.9 Magnetisation against time data for grains with fixed height 5 nm, and variable diameter (labelled). It can be seen that increasing the grain size from (a) to (e) shows gradual difficulty in the ability to switch.

pulse and write field, causing a large amount of neighbouring grains to also switch erroneously. This causes error when reading bits, as the boundaries between each one is less clear. On the other hand, towards the 8 nm diameter grains, the write field does not as easily overpower the anisotropy field. Additionally, different grain dimensions require a different T_{max} in order

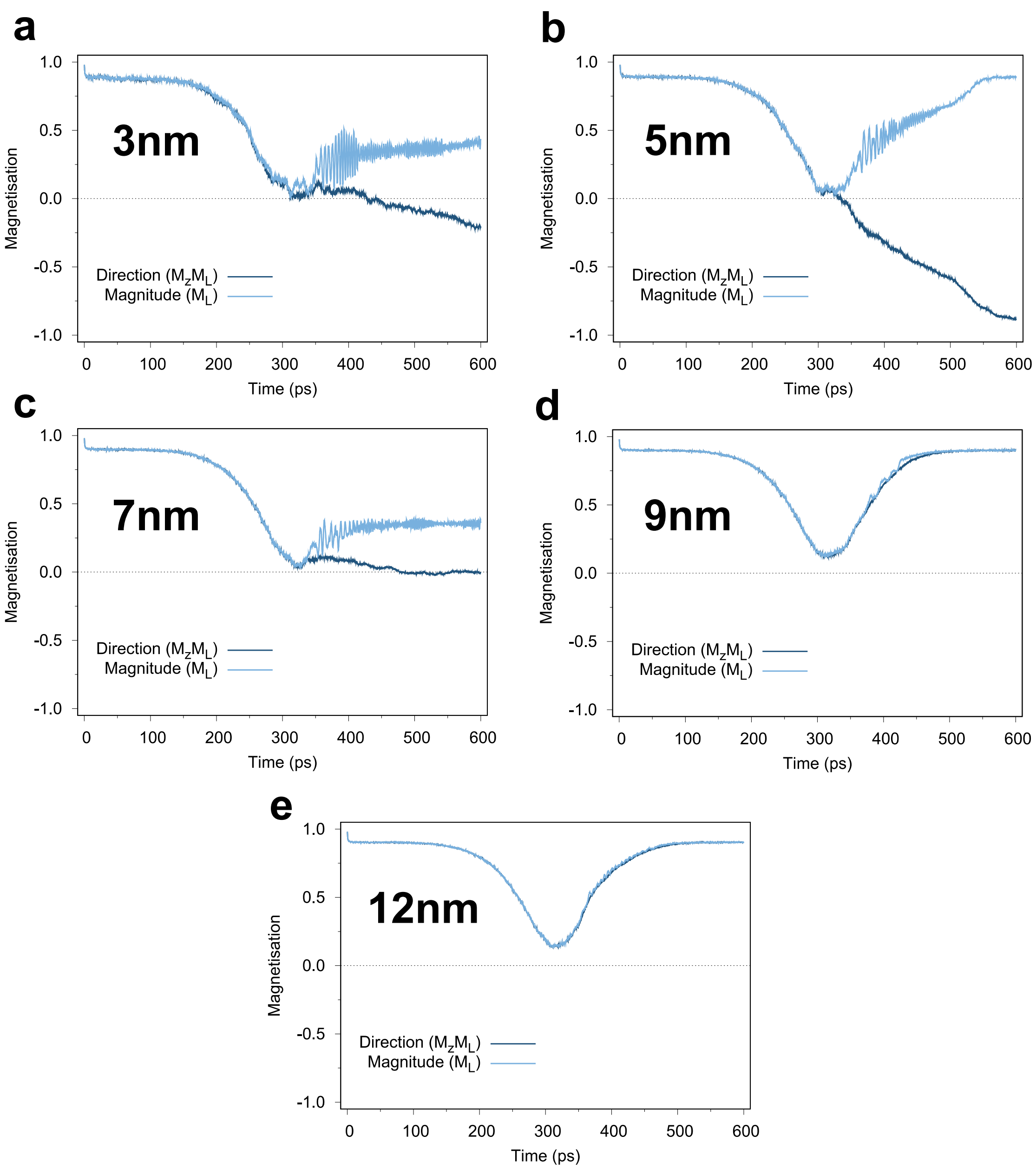

Fig. 3.10 The magnetisation against time data for 10 nm height grains, and increasing diameters from (a) to (e) as labelled. It is evident that the drastically larger aspect ratio of the grains compared to the 5 nm height variant leads to the rapidly deteriorating ability to switch.

to compensate for the variations in T_C values. Reaching the disordered state is crucial, as otherwise there is a significantly reduced probability of switching due to L1_0 FePt having high E_k below T_C. In terms of the clarity of the boundaries between each bit, 4 nm grain sizes are most clear, while still providing a significant areal density improvement from the

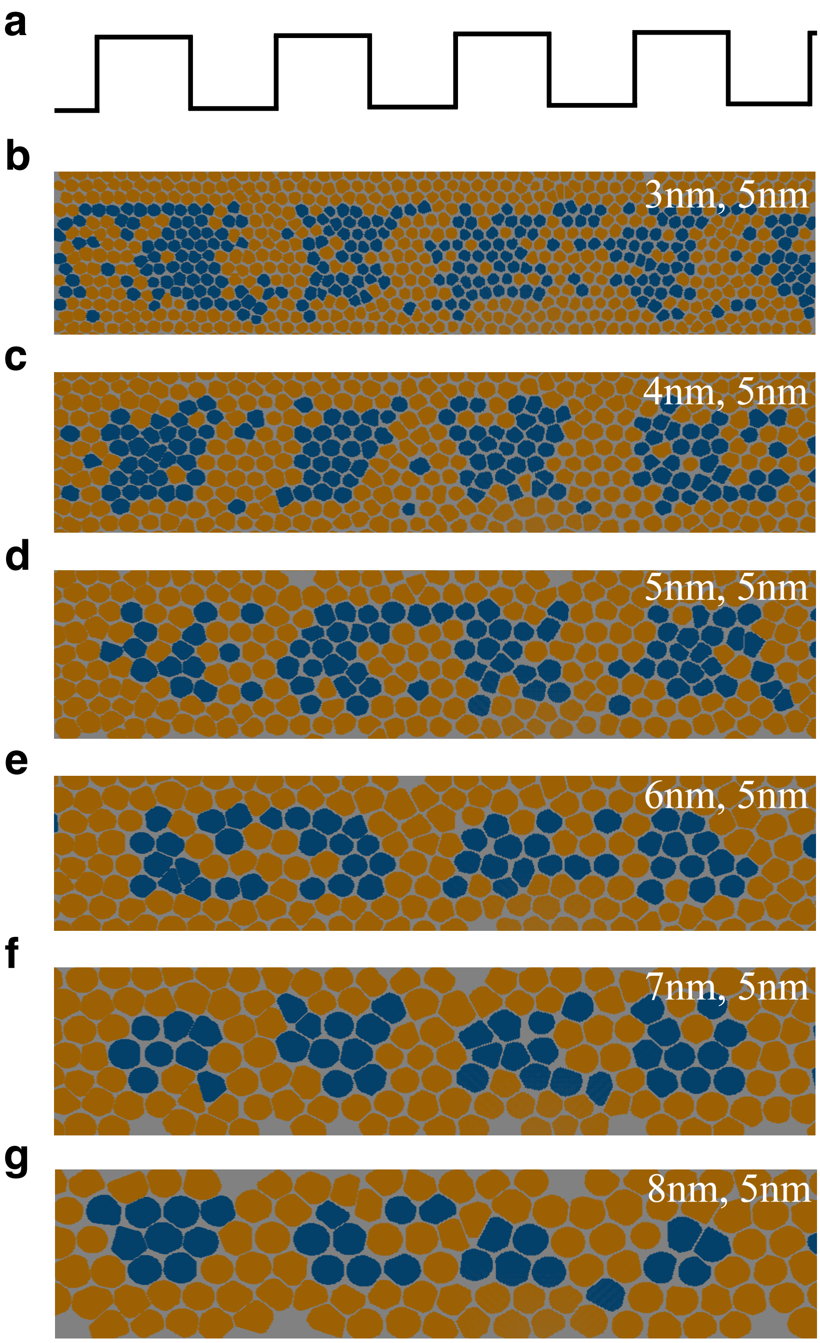

Fig. 3.11 A render of all the full HAMR systems simulated atomistically, which consist of 3 nm to 8 nm diameter grains with a fixed height at 5 nm. The blue grains have undergone magnetic switching whereas gold grains have remained in their original magnetic state.

currently used 8 nm grain sizes in traditional magnetic recording drives. It can be seen that at 3 nm, while some bits are clearer than others, there are too many accidentally switched grains near the bit boundaries. Contrarily, at the 7-8 nm grain diameters, the bit regions are not as clearly defined because it has become much more difficult to switch them under a fixed T_{max}, and the recording medium is far less discrete. In principle, the quantitative viability of these grain sizes under large-scale HAMR operations could be determined via statistical distributions across thousands of grains. This would also inform the necessary T_{max} required for a given grain geometry to switch consistently enough within a tolerable error-rate.

Overall, fully atomistic HAMR calculations reveal all the considerations of the magnetic recording quadrilemma. Smaller grain sizes are required for a higher data-storage density, which requires a larger temperature-dependent anisotropy to reduce erroneous writing. Higher anisotropies require larger write fields to have consistency in the writing process. Simultaneously it must be ensured that thermal backswitching does not erroneously undo the changes of the switched direction. All these considerations have to be taken into account, and are reflected in the results obtained for the attempted writing of the bit pattern shown in figure 3.11.

As a means of further improving the experimental reproducibility of this model, one potential improvement would be to incorporate a model of how the laser pulse thermodynamically couples to the spin sites, and calculates an atomistically local temperature gradient during the writing process. In addition to this, one could investigate the effects brought on by including dipole-dipole interactions, which are impossible to nullify in practice [91]. Finally, while qualitative conclusions can be drawn from the results presented, it would be beneficial to investigate the statistical nature of switching. For example, Meo *et al.* [27] computes the distribution of grain switching probabilities, which would lead to a more quantitative understanding of this behaviour. In the following chapters, the FePt model is expanded to include fully localised degrees of freedom, which has allowed for a re-calculation of fully atomistic FePt HAMR in a fully discretized spin-interaction framework, which allows for methods to investigate more clearly the effects of disordering and surface interactions.

3.5 Summary

This chapter covers the groundwork of investigating HAMR simulations from a fully atomistic standpoint. A detailed methodology breakdown is also provided for the spin interactions governing the behaviour of $L1_0$ FePt, and how its electronic structure provides favourable temperature-dependent anisotropy. This was modelled via the conventional atomistic parameters of FePt, whereby the two-ion anisotropy interactions were considered, so as to embed the atomistic effects of Pt being included in the bulk. A preliminary investigation was also done on the effects of T_C and temperature-dependent anisotropy with regard to grain size. It was found, that a grain height of 10 nm significantly promotes the appearance of domain walls, and in turn reduces the reliability of switching in a timely and stable manner. At 5 nm in height, the simulated grains showed viable switching behaviour up to 9 nm in diameter. A limitation of the results obtained is that the model introduced in this chapter assumes that the magnetic behaviour of Fe and Pt spins are aggregated to just the Fe sites, as the non-magnetic Pt is modelled via a modification to the standard Fe parameters, additionally, it prevents the investigation of even minor forms of species disordering, as Pt sites do not have their own degrees of freedom.

4

Longitudinal Spin Fluctuations in atomistic spin models

4.1 Motivation

Atomistic modelling of magnetic materials has always had multiple compromises in relation to a physical replication of the calculations that take place. With their reliability in being able to model real-life technologies, and an overall greater accessibility to more advanced computational strategies, atomistic modelling is being widely deployed, alongside its predecessor, micromagnetic simulations [92–94]. Because the use of atomistic modelling is varied and spans a large number of areas, specifically in the study of magnetism, the development and improvement of these models is crucial to the progress of researching new technologies for the future. In the research presented in this chapter, focus is placed on the augmentation of two currently existing and widely utilised integration schemes, the stochastic Landau-Lifshitz-Gilbert (LLG) and the Monte Carlo (MC) integrators, namely by including an additional longitudinal degree of freedom. The research into the inclusion of longitudinal fluctuations builds on the idea that currently modelling spin dynamics induces changes in the spin vector, which is constrained to a sphere of fixed size. This means that while the unit vector is allowed to vary, the system energy is being calculated in an incomplete manner as the energy changes arising from longitudinal fluctuations are neglected [95]. Khmelevskyi *et al.* [96] highlights a crucial example of the importance of including LSF, namely that the Curie temperature calculations obtained via currently used methods are unable to perfectly reproduce the correct values for Co, however upon including longitudinal dynamics, this issue was ameliorated. This problem is generally not seen as much in materials with highly localized spin structures such as Fe, but is crucially evident in situations where delocalized spin structures are present, where thermal fluctuations are responsible for representing the full contributions of their magnetic moment [95, 97]. Additionally, chapter 5 demonstrates the value of including LSF in modelling further alloys such as FePt, a notoriously complex magnetic system due to the Fe-induced Pt sites. An example of a practical use case of the LSF model is presented in chapter 6, which focuses on its importance in modelling Heat Assisted Magnetic Recording (HAMR).

A previous method of incorporating longitudinal degrees of freedom is the Landau-Lifshitz-Bloch (LLB) model, which decouples transverse and longitudinal moves in its equation of motion, and assigns different values for the critical damping parameter for both processes [65, 64]. Although it has had some success, the separation of the transverse and longitudinal timescales has lead to some unresolved complexities that arise from having a singular equation of motion with two types of moves being made [65]. For the equation of motion utilised in the LSF-LLG scheme, it is similar to the one of the LLB, with the major difference being that transverse and longitudinal damping parameters are set to be identical, which means that both types of motion effectively take place in the same instance and timescale [49, 50]. It is not fully clear as to the resultant effects this has on the accuracy of the LSF model, however this chapter goes at length to establish the validity of this computationally, by utilising the LSF-LLG under two separate solver mechanisms: the Heun scheme and the Runge-Kutta fourth-order (RK4) scheme. The two solvers implemented are both based on Runge-Kutta methods, which end on different stages. The Heun scheme is an extension of the second-order Runge-Kutta method, which is widely utilised due to its fast convergence to the desired gradient calculation, while also maintaining low computational overhead. The RK4 scheme on the other hand uses additional steps to get to its final gradient, and thus is less efficient computationally, but is the more accurate of the two [57, 98].

The LSF integrator schemes create a longitudinal variation by appending a set of spin length dependent energy terms to the conventionally used Hamiltonian. The combination of these additional terms are known as the Landau Hamiltonian, as they follow the Landau expansion with the ordering parameter being the atomistic spin length. Physically, it is uncertain to assume that longitudinal and transverse moves operate at the same timescale, which is an underlying assumption of the current LSF-LLG implementation. In order to address this challenge such that this constraint can be navigated around, one possibility would be to use the LSF-MC scheme established, and to further iterate on its formalism for fully separated sampling of longitudinal and transverse moves. In the current implementation, while much more inefficient, the moves are combined into a single sampling routine which samples a sphere of variable radius for every spin site. Decoupling this step would allow for finer control over the exact energetics and phase spaces that both transverse and longitudinal moves can occupy.

A current constraint of the LSF models developed is that with the current definition of spin length being a property of spin sites in an atomistic system, it must be defined such that at T = 0K, $|S| = 1$, in order to be calibrated with the default moment length a system begins with. In a highly controlled and uniform system, this is simply a matter of correctly parametrising the longitudinal energy surface to describe an energy minimum at $|S| = 1$. In an average situation however, contributions from nearest neighbour exchange interactions will move this initial longitudinal energy surface around, such that the equilibrium spin length condition cannot be met. This frequently arises due to stoichiometric variations that affect the exchange coupling in a system, which causes incorrect calculations of moment size changes. The implementation described in this chapter provides a means of correcting for this unwanted shift in longitudinal energy, via the re-fitting of the energy parameters, taking into account the system-dependent exchange energy configuration.

An additional highlighted challenge with the LSF model is the requirement for an exchange coupling re-adjustment. Ma *et al.* and Ellis *et al.* have clearly demonstrated that the implementation of LSF schemes has consistently brought underestimations in the value of the calculated T_{C} and T_{N} in materials. It is discussed that such models are required to have a readjustment of the exchange coupling constants, which are now perturbed by the evaluation of longitudinal energies. The idea that adding novel energy components that directly interact with the heat-bath of the system causes unwanted alterations to spin correlation has previously been shown in Böttcher *et al* [99]. As a result, we introduce a form of correcting the exchange coupling constants J with respect to temperature via a coefficient, which shows the necessity of such a correction as per the T_{C} and T_{N} results obtained.

Overall, this chapter highlights the details behind implementing the LSF model into a wide range of systems with inherently different magnetic behaviours (Fe, Ni, Co, and Cr). For each case, the exact constraint and alleviation of said constraint is shown, in order to ensure applicability to the most number of cases as possible. The first part of the results show the usage of the LSF-LLG integrator scheme with both the Heun and fourth-order Runge-Kutta solvers, which have tested the convergence limits of the newly implemented integrator scheme. Next, calculations are shown to demonstrate that the appropriate relationship of spin length against temperature is recovered as expected by the Landau Hamiltonian, via the use of longitudinal Boltzmann probability distributions. This showed clearly the dependence of the longitudinal potential well with respect to the explorable longitudinal states in a given material. The overall temperature-dependent magnetisation properties were computed, giving values for T_{C} that replicate experimental data. Additionally, the calculations show the effects of a variable spin length during the heating process for the different materials. Finally, an investigation into the ultrafast demagnetisation dynamics of Ni was conducted to determine the effectiveness of longitudinal schemes in sub-picosecond laser pulse calculations. The importance of longitudinal variation has been demonstrated experimentally, and thus was crucial to highlight as a test case in this chapter [100].

4.2 Theory

4.2.1 The atomistic spin Hamiltonian

The form of the atomistic spin Hamiltonian used in this chapter contains the energy contributions for three main components: exchange, anisotropy, and applied fields, denoted by $\mathscr{H}_{\mathrm{exc}}$, $\mathscr{H}_{\mathrm{ani}}$, and $\mathscr{H}_{\mathrm{app}}$, and is described in full detail in chapter 2.

Out of the materials investigated in this chapter, Fe, Ni, and Co are parametrised using ferromagnetic exchange coupling is denoted by exchange constants with $J^{\text{1-nn}} > 0$, whereas $J^{\text{1-nn}} < 0$ corresponds to antiferromagnetic interactions seen in Cr. To emulate the antiferromagnetic correlation of spins, Cr systems are defined as having two equivalent sublattices, with the distinction between them that their exchange constants are J within the lattice, and $-J^{\text{1-nn}}$ when interacting with the opposing lattice. It should be highlighted, that in the form presented by the conventional Hamiltonian, the spin vector utilised is specifically of a unit length meaning that the integrator schemes conventionally employed to compute spin changes explicitly normalise $|S| = 1$. In order to remove the restriction on this quantity to include longitudinal changes, the spin vector in the conventional Hamiltonian has to be adjusted to use the form $\mathbf{S} = \hat{\mathbf{S}}|S|$, as discussed in 2.1.5.

4.2.2 Equilibrium correction of Landau coefficients

In order to ensure that at equilibrium the Landau coefficients computed via DFT calculations give a spin length of $|S| = 1$, a re-adjustment of the coefficients are required. The reason for this is to ensure that the reference energy state of the calculated coefficients lines up with the reference state of the simulated system, meaning that the total exchange and anisotropy contributions have to be equal for both instances. It is assumed in the following that the Landau coefficients for a given material are generally the same between minor changes to the energy reference states that arise due to system size, or the minor addition of disordering. From this assumption, the following equation describes the re-adjustment process by introducing minor shifts to the energy surface, to redirect the energy minima to

Parameter	Fe (bcc)	Ni (fcc)	Co (hcp)	Cr (bcc)
μ_s (μ_B)	2.22	0.61	1.72	0.50
$J_{ij}^{\text{1-nn}}$ (J/link)	7.050×10^{-21}	2.757×10^{-21}	6.064×10^{-21}	2.306×10^{-21}
k_u (J/atom)	5.65×10^{-25}	5.47×10^{-26}	6.69×10^{-24}	–
A' (J)	-6.404×10^{-20}	-1.072×10^{-21}	-5.698×10^{-21}	-3.209×10^{-20}
B' (J)	3.082×10^{-20}	7.457×10^{-21}	7.499×10^{-22}	1.191×10^{-20}
C' (J)	9.641×10^{-21}	8.486×10^{-22}	1.401×10^{-20}	5.368×10^{-21}
λ	0.1	0.1	0.1	0.1

Table 4.1 The collective simulation parameters utilised in this chapter for the materials examined. The Landau coefficients were obtained outside the scope of this thesis using methods from Pan *et al* [31]. The rest of the simulation parameters follows what was obtained in Evans *et al* [28].

what was assumed by the DFT reference state:

$$\mathscr{H} = \sum_i \sum_\alpha A_\alpha \left(\frac{|S_i|}{D_\alpha}\right)^2 + B_\alpha \left(\frac{|S_i|}{D_\alpha}\right)^4 + C_\alpha \left(\frac{|S_i|}{D_\alpha}\right)^6 - \sum_{i<j} J_{ij}^{\text{1-nn}} \mathbf{S}_i \cdot \mathbf{S}_j - k_\mathrm{u} \sum_i (\mathbf{S}_i \cdot \hat{\mathbf{e}}_i)^2, \tag{4.1}$$

where the material dependent temporary coefficient D_α can be determined by analytical fitting, such that the minimum position of the Landau Hamiltonian must lie at $|S| = 1$. It is important to note, that the terms for exchange and anisotropy have been included in this definition so as to get a more complete picture of the energy reference state used to obtain the Landau coefficients. After re-adjusting the longitudinal energy surface via D_α, data points of this adjusted curve are computed, and the original Landau Hamiltonian in equation 2.25 is re-fitted to the new data via contributions solely from coefficients A_α, B_α, and C_α (omitting J and k_u as fitting parameters). This refitting process now embeds the refitting modifications introduced into the original coefficients, and thus the currently used energy reference state has been fully accounted for. The new Landau Hamiltonian with augmented coefficients is described according to the following expression, which can then be used with the LSF integrator schemes:

$$\mathscr{H}_L' = \sum_i \sum_\alpha A_\alpha' |S_i|^2 + B_\alpha' |S_i|^4 + C_\alpha' |S_i|^6, \tag{4.2}$$

where A_α', B_α', and C_α' are the equilibrium-adjusted Landau coefficients. Following readjustment, table 4.1 summarises the re-adjusted simulation parameters for the tested material species. While this rescaling method fixes the fundamental issue of not having the right equilibrium spin length, it should be highlighted that this also unintentionally affects the curvature of the potential, which may not be desirable.

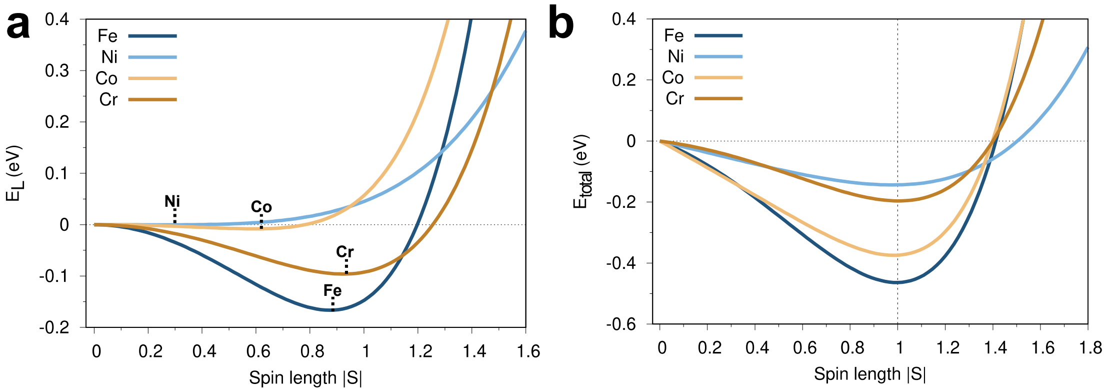

Fig. 4.1 The longitudinal energy surfaces for Fe, Ni, Co, and Cr which depend on the configuration of the Landau Hamiltonian coefficients. (a) shows the purely longitudinal energy components, while (b) includes the effects of exchange energy.

Figure 4.1 shows the longitudinal energy surfaces with and without including exchange energy contributions for the tested materials: Fe, Ni, Co, and Cr. It can be seen that there is a variety of different longitudinal energy dependencies between the different material species, which is greatly informed by the behaviour of its moment size. For example, Ni demonstrates a very shallow potential well, meaning that even small changes in energy can be expended to see drastic shifts in $|S|$. On the other hand, a material such as Fe sees very minor shifts in $|S|$ as it is prohibitively expensive energetically to undergo changes to $|S|$. This is due to the highly localised nature of Fe's *d* electrons, meaning a stiff moment is expected. Once the exchange energy contributions are factored in, the re-adjusted coefficients are brought to the appropriate spin length minima, as it can be seen that there is alignment with $|S| = 1$. This means at $T = 0$ K for example, the initial moments of all the materials are exactly their respective μ_s. It should be noted, that the Landau energies being included in the total Hamiltonian means that as the magnitude of the exchange term ceases at higher temperatures due to disordering, the amount by which the longitudinal energy surface shifts is variable, and thus the value of $|S|$ fluctuates accordingly. For example, at higher temperatures larger fluctuations of the moment size occur.

Figure 4.2 shows the overall dependence between the longitudinal energy surface and temperature, whereby it can be seen that a range of different longitudinal potentials are obtained. This exact behaviour occurs due to the contribution of the exchange term having different magnitudes with respect to temperature. A more disordered system is going to have less correlation between spins, and thus the exchange energy term is significantly less at $T \approx T_\mathrm{C}$ than at equilibrium. Therefore, with increasing temperature, the longitudinal potentials are brought back closer to their exchange-less forms. Additionally, the first order derivative of the total Hamiltonian is shown, which describes the evolution of the spin length

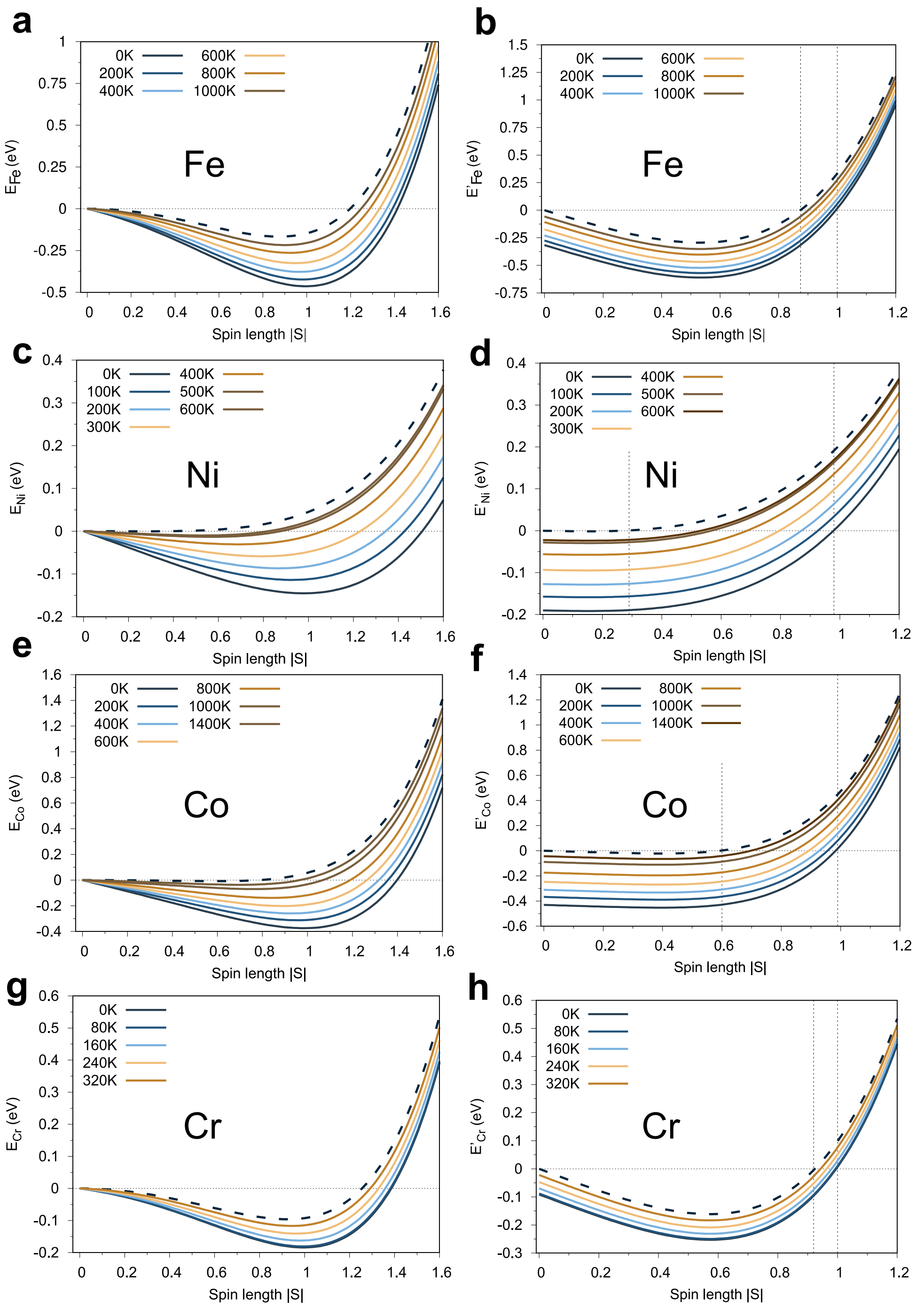

Fig. 4.2 Figures (a), (c), (e), and (g) show the material specific longitudinal energy surfaces with the temperature effects of exchange included, and (b), (d), (f), and (h) are the respective first derivatives of the total Hamiltonian with respect to $|S|$. The exchange contribution at each temperature was extracted via bulk calculations, and then analytically plotted using the total LSF Hamiltonian.

minima with temperature (at the points where $E' = 0$). Once again, this shows that different material species will exhibit different scaling behaviour of $|S|$ with respect to total energy.

4.3 Simulation methods

4.3.1 Temperature-dependent longitudinal dynamics

An area of particular interest is to be able to use the LSF model to recover the appropriate T_C and T_N values of given materials. As a result, calculations were done on Fe, Co, Ni, and Cr to compute the resultant temperature-dependent magnetisation properties while including longitudinal degrees of freedom. An important aspect to note, is that the moment size can now be modelled with respect to temperature, and thus a good indication can be obtained to show the relative moment size with respect to system disordering or temperature. The magnetisation against temperature data was calculated for 6 nm × 6 nm × 6 nm systems, using the LSF-MC scheme. At every temperature increment, 5000 equilibration timesteps were allowed, which ensured that the system reaches equilibrium before magnetisation data is recorded. From there, 35000 loop timesteps were dedicated to collecting system magnetisation data. It should be noted, that because Cr is modelled across 2 sublattices due to its antiferromagnetic nature, the magnetisation properties quantified per Cr site is the average of the two sublattices. In order to fit the T_C or in the case of Cr the T_N data, the following equation was used [28, 80]:

$$m(T) = \left(1 - \left(\frac{T}{T_\text{C}}\right)^{\alpha}\right)^{\beta}, \tag{4.3}$$

where the temperature-dependent magnetisation $m(T)$ is represented by a normalised scaling of temperature T with respect to the Curie or Néel temperatures with two fitting parameters as exponents. α is a system dependent parameter, while β is approximately 0.340 under experimental conditions [80]. In addition to this, the longitudinal sublattice susceptibility against temperature was plotted, which describes the transition to a paramagnetic state as a singular peak. This was used as a measure to ensure the correct T_C and T_N was obtained. As it was previously discussed in Ma *et al.* and Ellis *et al.* [49, 50] that an adjustment to the exchange coupling parameter J was required under the LSF model, a temperature-dependent scaling described as the following was used:

$$J_\text{modified} = J(1 - F_\alpha(T/T_\text{C})), \tag{4.4}$$

where F_α describes a material specific exchange scaling factor. The inclusion of the exchange readjustment is shown to be crucial, as it is consistent across all systems that T_C and T_N is otherwise underestimated. The form of such an adjustment leading to an increase in J is justified by the fact that the LSF model emulates a larger amount of electron mobility due to the additional longitudinal degrees of freedom.

4.3.2 Ultrafast demagnetisation with longitudinal dynamics

To compute the ultrafast magnetisation dynamics of Ni, a sub picosecond demagnetisation calculation was done via a two-temperature model to determine the effectiveness of the LSF model in appropriately replicating the experimental results obtained [101]. The simulation is set up such that a laser pulse creates temperature changes to the electron temperature T_e, which is then allowed to transfer heat to the lattice, governed by lattice temperature T_l. The two systems are coupled via a coupling factor G, which controls the rate at which energy is transferred between the two otherwise isolated systems. The equations governing the transfer of thermal energy between T_e and T_l are shown in the following [80]:

$$C_e \frac{\partial T_e}{\partial t} = -G(T_e - T_l) + \Gamma(t), \tag{4.5}$$

$$C_l \frac{\partial T_l}{\partial t} = -G(T_l - T_e), \tag{4.6}$$

where $\Gamma(t)$ is a Gaussian distribution function that has a FWHM of 60 fs, and C is the heat capacity. In this simulation, $G = 1.2 \times 10^{18}$ Wm^{-3}K^{-1}, $C_e = 8 \times 10^2$ Jm^{-3}K^{-1}, and $C_l = 4 \times 10^6$ Jm^{-3}K^{-1} [102]. This demagnetisation process was calculated for an 8 nm × 8 nm × 8 nm system of Ni, which was repeated with both the conventional LLG and LSF-LLG integrators. This is because it was important to verify the qualitative and quantitative differences brought on by the inclusion of longitudinal dynamics. An additional simulation parameter that was included was a temperature rescaling function, which ensured that the data obtained more appropriately followed experimental trends via the system dependent scaling parameter α. The equation governing the temperature rescaling relationship is described as [80]:

$$\frac{T_\mathrm{rescaled}}{T_\mathrm{C}} = \left(\frac{T_\mathrm{expt}}{T_\mathrm{C}}\right)^{\alpha}. \tag{4.7}$$

This equation ensures that the actual simulated temperature at a given point is the T_rescaled quantity, which has a re-adjusted origin. In this case, Evans *et al.* finds that $\alpha = 2.322$ for Ni [80].

4.4 Results and discussion

4.4.1 Single spin calculations

Single spin dynamics of the LLG schemes were verified by allowing a single spin to relax from starting in the [100] direction to [001] via an applied field along the z-axis of 10 T. The system was allowed to relax for 50 ps with a timestep size of $\Delta t = 1 \times 10^{-16}$ s and damping $\lambda = 0.1$, while its variation in **S** was computed. The associated error was also found via the relationship ($S_{\text{calculated}} - S_{\text{analytical}}$) using the following equations [28]:

$$S_x(t) = \operatorname{sech}\left(\frac{\lambda\gamma H}{1+\lambda^2}t\right)\cos\left(\frac{\gamma H}{1+\lambda^2}t\right), \tag{4.8}$$

$$S_z(t) = \tanh\left(\frac{\lambda\gamma H}{1+\lambda^2}t\right). \tag{4.9}$$

Validating the single-spin calculation of the time-dependent LSF-LLG integrator scheme is important to ensure that a convergent solution is obtained. As a result, both the Heun and fourth-order Runge-Kutta (RK4) forms were tested with and without thermal fluctuations ($T = 0.1$ K and $T = 0.0$ K respectively), to ensure that the timescales utilised in the magnetisation calculations were able to resolve the spin motions appropriately.

Figure 4.3 shows the single spin dynamics of the implemented LSF-LLG models, alongside the expected result computed using the LLG integrator. The LSF-LLG by default assumes the Heun solver scheme, unless otherwise stated. It can be seen that there is a deviation from the associated damping force that is visible between the LLG and LSF-LLG integrators, whereby the S_x quantity does not overlap. This was determined to be an entirely physical consequence of the LSF-LLG form, as it can be compared to what is obtained using the fourth-order Runge-Kutta solver for the same simulation. The latter is known to provide a much more accurate solution to integrating the equation of motion, and thus the difference arising from implementation differences can be eliminated. The exact nature of this apparently larger damping parameter in the LSF-LLG is attributed to the following: a reformulation of the dissipation term to include longitudinal motion now includes both transverse and longitudinal contributions, whereas the conventional LLG only considers the transverse form. This means that the longitudinally-induced damping couples to the transverse one, and thus $\lambda_{\text{LLG}} < \lambda_{\text{LSF-LLG}}$ is obvious. The nature of this behaviour is simply that to obtain the equation of motion for the LSF-LLG, one must use the identity $\lambda_{\text{transverse}} = \lambda_{\text{longitudinal}}$, which means both are treated under the same timescales

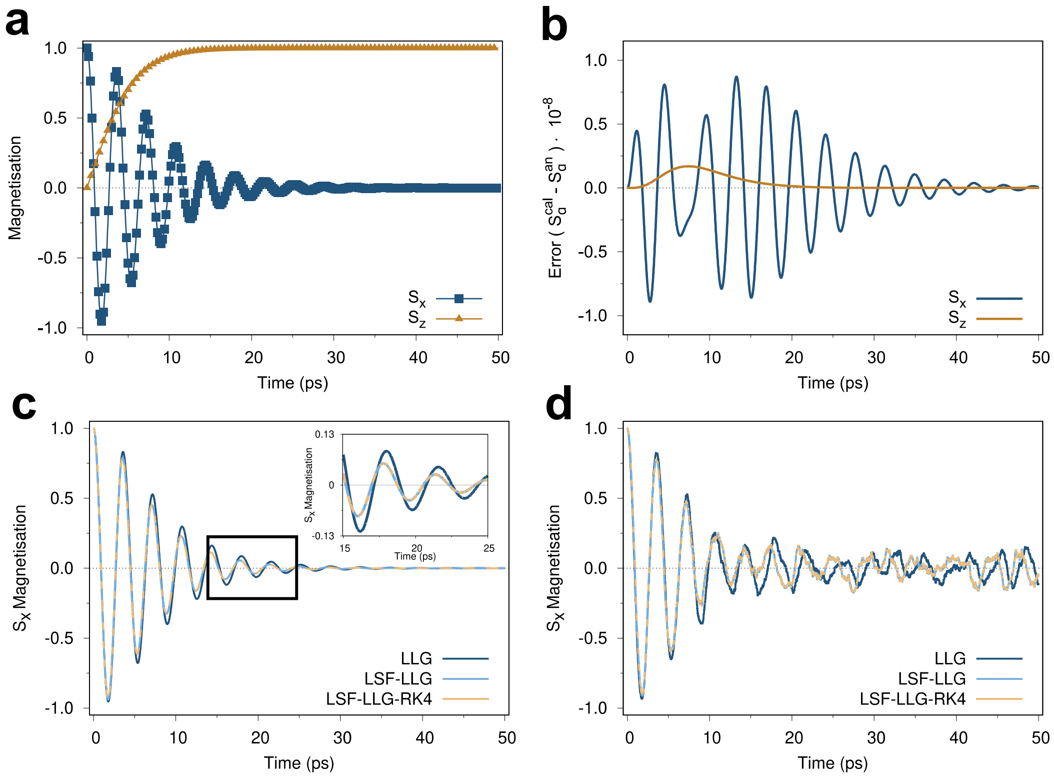

Fig. 4.3 (a) single spin LLG dynamics, and the error between analytical and calculated results in (b). (c) shows the 0K dynamics for the LLG compared to the LSF-LLG and LSF-LLG-RK4 schemes, while (d) is the 0.1K case. It can be seen that both Heun and RK4 solvers converge to the same result appropriately.

and dissipation terms. The validity of such an assumption is still unclear, and is left to future work to explore further.

4.4.2 Boltzmann probability distributions

By employing the LSF-MC integrator scheme, the longitudinal probability distributions for the tested systems can be obtained. A single spin at various temperatures will naturally equilibrate to a variation of spin lengths which is described by the total Hamiltonian of the system. Longitudinal Boltzmann probability distributions calculate the probabilities of the given states of $|S|$, which can be used to verify that the correct temperature-dependent longitudinal behaviour is attained. The $|S|$ data was binned across 5×10^6 Monte-Carlo steps, to ensure that all explorable states have been accessed. The following equation describes the

Boltzmann function that recovers the expected spin length distributions:

$$P \propto \exp\left(-\frac{\mathscr{H}}{k_{\mathrm{B}}T}\right). \tag{4.10}$$

The proportionality relation should be noted, as the exact height of the distribution will depend on the number of MC steps which determines the maximal peak of the fit.

In figure 4.4, the longitudinal Boltzmann probability states are shown for Ni, with and without the inclusion of the exchange energy term in the total Hamiltonian. The results show an excellent agreement with the expected fit according to the Boltzmann probability function, which evaluates the probability of a new spin state being explored according to the LSF-MC integrator. It is clearly shown, that without exchange, the naturally shallow Ni longitudinal energy surface tends towards a large width of $|S|$ states, as is described by its Landau coefficients. With respect to temperature, it can be seen that additional broadening of the longitudinal states occurs, whereby the system has more free energy to explore a larger range of states than what was previously available. Because Ni's moment is greatly influenced by its own exchange field, the moment exchange energy contributions are used in the total Hamiltonian, a consequently significant narrowing of the distribution occurs. Firstly, it is now centred around $|S| = 1$ at low temperatures due to the equilibrium re-adjustments made to the Landau coefficients. Secondly, the effects of the exchange energy can be seen: as $T \rightarrow T_{\mathrm{C}}^{\mathrm{Ni}}$, the exchange energy contribution follows the trend $E_{\text{exchange}} \rightarrow 0$, which then transforms the longitudinal distribution into the exchange-less form.

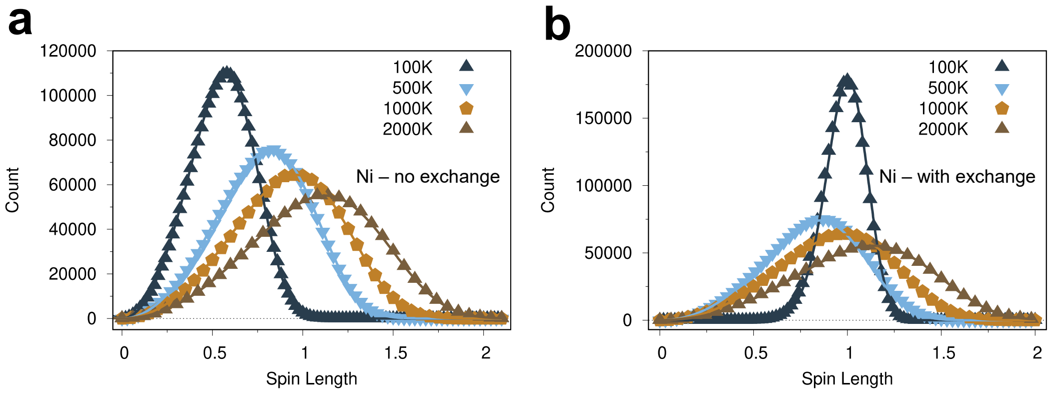

Fig. 4.4 Ni longitudinal Boltzmann distribution without (a) and with (b) exchange energy included in the total Hamiltonian. It can be seen that there is a reduction in the broadening of the distribution given an exchange field, indicating a strongly polarised moment. The simulated points were fitted via equation 4.10.

The full exchange-less Boltzmann probability distributions of the studied materials is shown in figure 4.5. A clear relationship between the stiffness of a moment and the width of the probability distribution can be observed. Systems such as Fe are tightly localised moments, which means small changes are expected in the spin length quantity $|S|$, and thus it assumes narrow distributions. Ni on the other hand has a significantly less localised moment, which shows greater distribution width, and a tendency towards much higher spin length values with increasing temperature. Co is also shown to be similarly shallow to Ni, though this is quickly changed by the fact that once the exchange interaction is included, Co quickly behaves as a stiff moment similar to what is seen in Fe. Finally, Cr is seen to be almost as stiff as Fe, with a bit more distribution width. The Boltzmann probability distributions obtained also validate the sampling algorithm used by the LSF-MC, as it can be seen that it reproduces what was expected by the Landau coefficients for the four materials, and additionally is fitted appropriately with the use of the Boltzmann probability function.

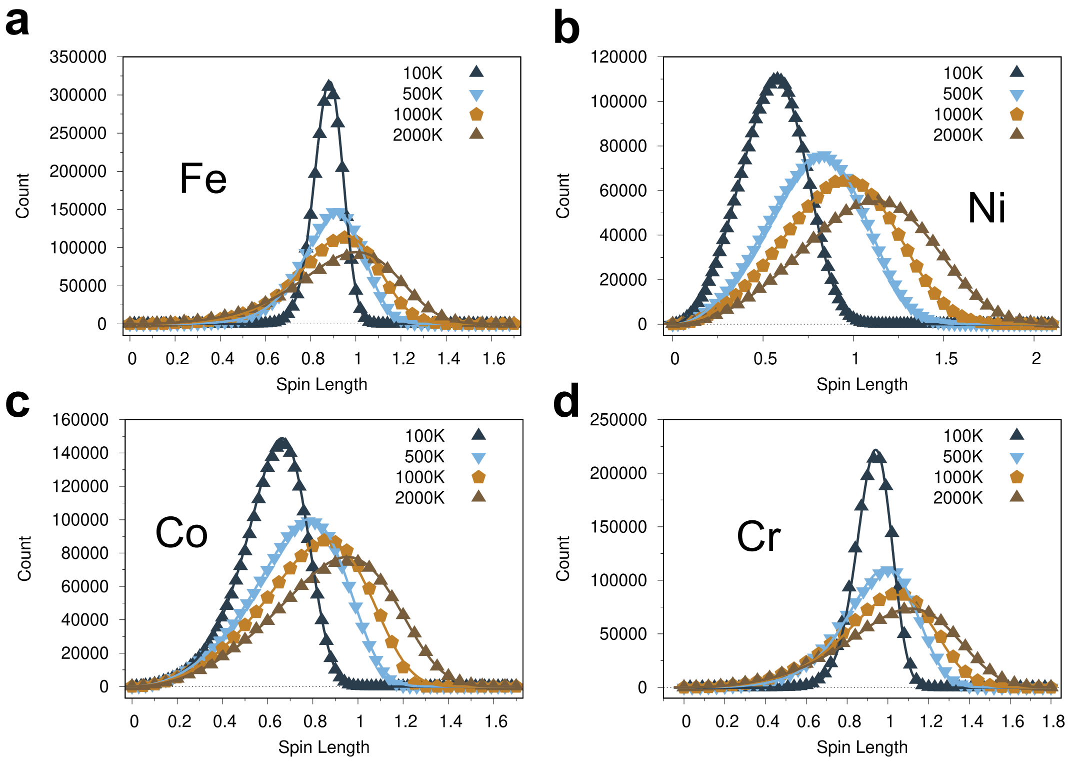

Fig. 4.5 Without the inclusion of exchange energy, the longitudinal Boltzmann distributions are shown for Fe (a), Ni (b), Co (c), and Cr (d). The width of the distributions clearly increase with larger temperatures, allowing for a larger number of unexplored longitudinal states to manifest.

4.4.3 Curie and Néel temperature calculations

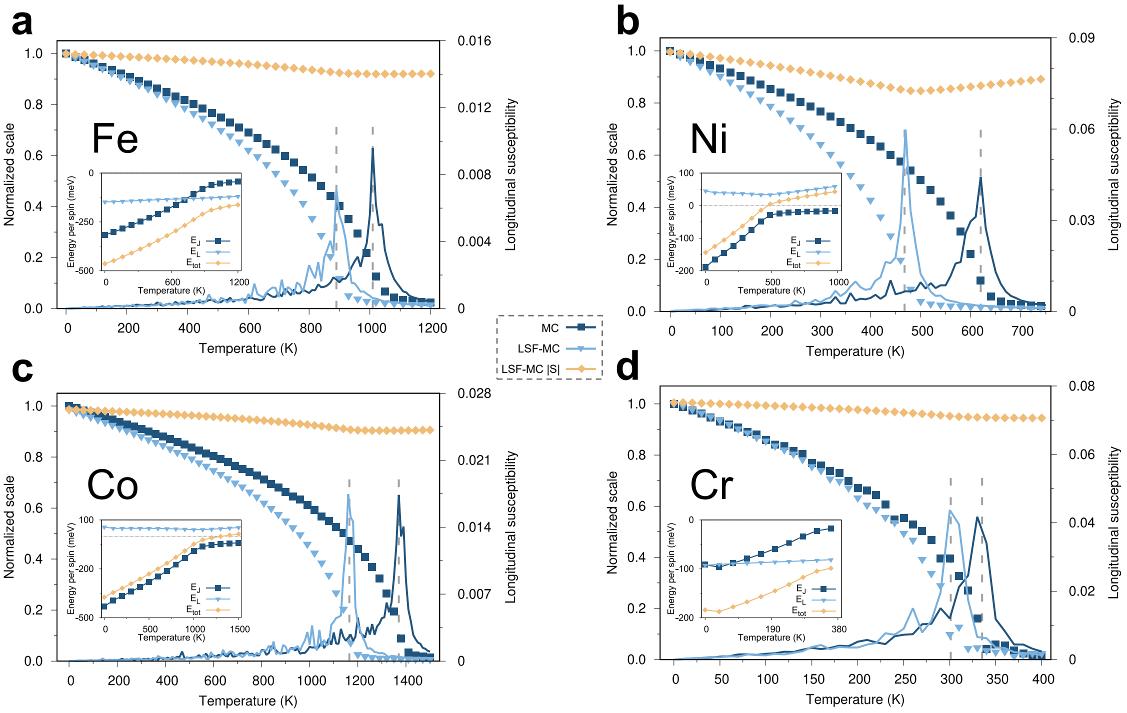

Fig. 4.6 The temperature-dependent magnetisation properties of Fe (a), Ni (b), Co (c), and Cr (d). "MC" (dark-blue) corresponds to the Monte-Carlo integrator, "LSF-MC" (light-blue and gold) corresponds to the longitudinal Monte-Carlo integrator. The "LSF-MC $|S|$" label denotes the calculated spin-length using the longitudinal Monte-Carlo. It is clear that there is a consistent underestimation of T_{C} and T_{N} given the LSF model, which leads to the conclusion that an exchange coupling adjustment is mandatory.

The temperature-dependent magnetisation calculations for Fe, Ni, Co, and Cr are shown in figure 4.6. Firstly, a direct comparison of the conventional MC and LSF-MC can be discussed. It is evident overall that without adjustment, $T_{\mathrm{C}}^{\mathrm{LSF}} < T_{\mathrm{C}}^{\mathrm{MC}}$ across all materials. This was also shown to be the case in previous implementations of similar longitudinal spin fluctuations models [49, 50]. Additionally to the normalised magnetisation metric, the value for $|S|$ can also be seen to vary with respect to temperature. Generally, the relationship for $|S|$ outside the paramagnetic regime is affected by exchange energy contributions, and thus a consistent reduction in $|S|$ can be seen until T_{C} and T_{N}. After the exchange contribution is approximately 0 beyond this temperature, $|S|$ is allowed to increase, as simply adding more energy to the Landau energy surface allows for a broader range of energies to be accessed. The case for Ni is particularly interesting, as this behaviour is amplified due to its shallow potential well. Initially, the decreasing exchange causes a reduction in $|S|$ as the spin length minima slowly returns to its equilibrium exchange-less minimum. As T increases beyond the paramagnetic transition, the system is simply allowed to explore larger $|S|$ quantities without any further perturbations. While the other materials also show similar behaviour, they are not as pronounced as in Ni. To more clearly define the value of T_C and T_N, the average sublattice susceptibility is also shown alongside the normalised magnetisation data, which shows clear peaks at the paramagnetic transition phase. For Cr, all data was an average across both of its sublattices with equal and opposite exchange coupling constants, as it is simulated in an antiferromagnetic configuration.

A summary of T_C data collected is shown in table 4.2. It can be seen that upon applying the exchange re-adjustment factor necessitated by the LSF schemes, there is good agreement with experimentally obtained values of T_C and T_N. As the results show, there is clear viability in the introduction of longitudinal degrees of freedom in determining the temperature-dependent behaviour of magnetic materials. It should be noted, that in order to obtain the exchange re-adjustment coefficients, prior knowledge as to the $M(T)$ behaviour of the material is needed. While this clearly increases the complexity of such a model, for a given lattice orientation of a material the factor F_α only has to be calculated once before it can be utilised in other simulations or systems. It should however be noted, that the value for F_α is significantly altered in the cases of alloying for example, where new material species are introduced, or drastically different temperature to system coupling methods are included. The exchange coupling interactions between the different species introduces additional complexities that are not trivial to dissect, and thus an exact treatment of exchange re-adjustment in alloyed systems is left to future work. It should be noted that the adjustment to the exchange can also be introduced via changes to the initial DFT calculations for every system. It is currently not evident what the most appropriate strategy is to introduce variability to the exchange coupling.

T_C/T_N (K) System	 Expt.	 MC	 LSF-MC	 F_α
Fe (bcc)	1043	1033	1037	0.13
Ni (fcc)	633	623	639	0.18
Co (hcp)	1388	1375	1356	0.22
Cr (bcc)	311	335	313	0.03

Table 4.2 The temperature-dependent calculations of the tested materials, drawing a comparison between the LSF and conventional integrator schemes. F_α also shows the necessary exchange coupling adjustment applied to each system. It can be seen that good experimental agreement is obtained with this adjustment [103, 104].

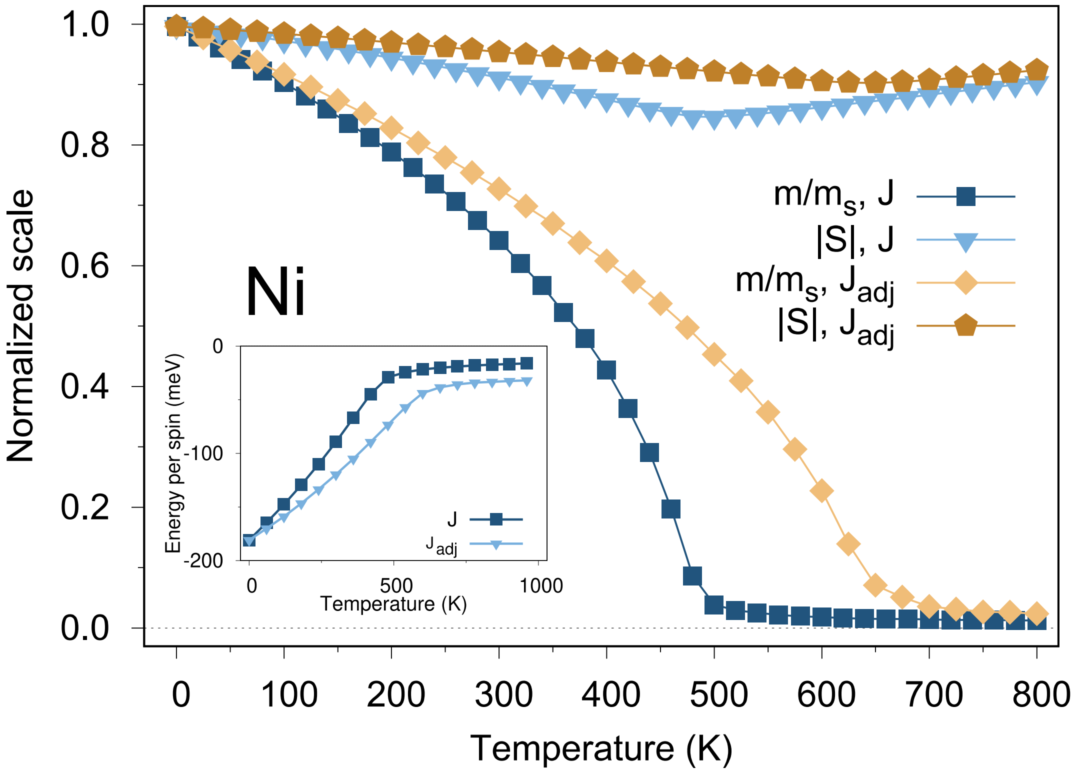

Fig. 4.7 The temperature-dependent magnetisation of Ni changes drastically given the introduction of a temperature-dependent exchange adjustment. It can be seen that the appropriate T_C is reproduced with a necessary rescaling of the exchange coupling constant J.

A crucial highlight of the exchange re-adjustment process is shown in figure 4.7. The calculations for the standard treatment of exchange and re-adjusted exchange show a significantly different scaling in terms of exchange energy against temperature, which is a requirement in including the longitudinal energy contributions according to the Landau Hamiltonian. After adjustment, the T_C of Ni is obtained to be $T_C^{LSF} = 639$ K, which is in good agreement with experimentally obtained $T_C^{expt} = 633$ K. It should be highlighted that because the exchange energy with respect to temperature goes to $J = 0$ at a slower rate, the relationship between $|S|$ against T is also affected. Appropriately, the behaviour of decreasing $|S|$ followed by its increase at the paramagnetic transition still remains as per the description of its longitudinal energy surface. It is important to validate the exchange rescaling presented in these calculations in other environments where different dynamic interactions play a role in varying a given system's magnetisation evolution. As a further area of application, the sub-picosecond demagnetisation dynamics discussed in the next section cover the application of exchange re-adjustment in Ni in a different type of calculation.

4.4.4 Ultrafast demagnetisation of Ni

Figure 4.8 shows the sub-picosecond demagnetisation of a Ni system, via the emulation of a laser pulse that regulates the temperature of the spins via a two-temperature model. This was calculated using only the LLG and LSF-LLG integrator schemes, which was a requirement as explicit time-dependence cannot be introduced into the current form of the LSF-MC. It should be noted, that a timestep size of $\Delta t = 1 \times 10^{-16}$ s was used for this calculation with $\lambda = 0.001$. The system was allowed to equilibrate at $T = 300$ K for 200000 timesteps ($t = 20$ ps), and then a laser pulse was instantaneously applied, which influenced the temperature of the system. The system was allowed to evolve for an additional 200000 timesteps after the introduction of the temperature pulse, to allow for thermal energy transfer between the electron and lattice temperatures (T_e and T_l respectively) which were coupled to each other. After about 10ps past the introduction of the laser pulse, both systems are in equilibrium with one another, and thus a constant magnetisation value is attained by

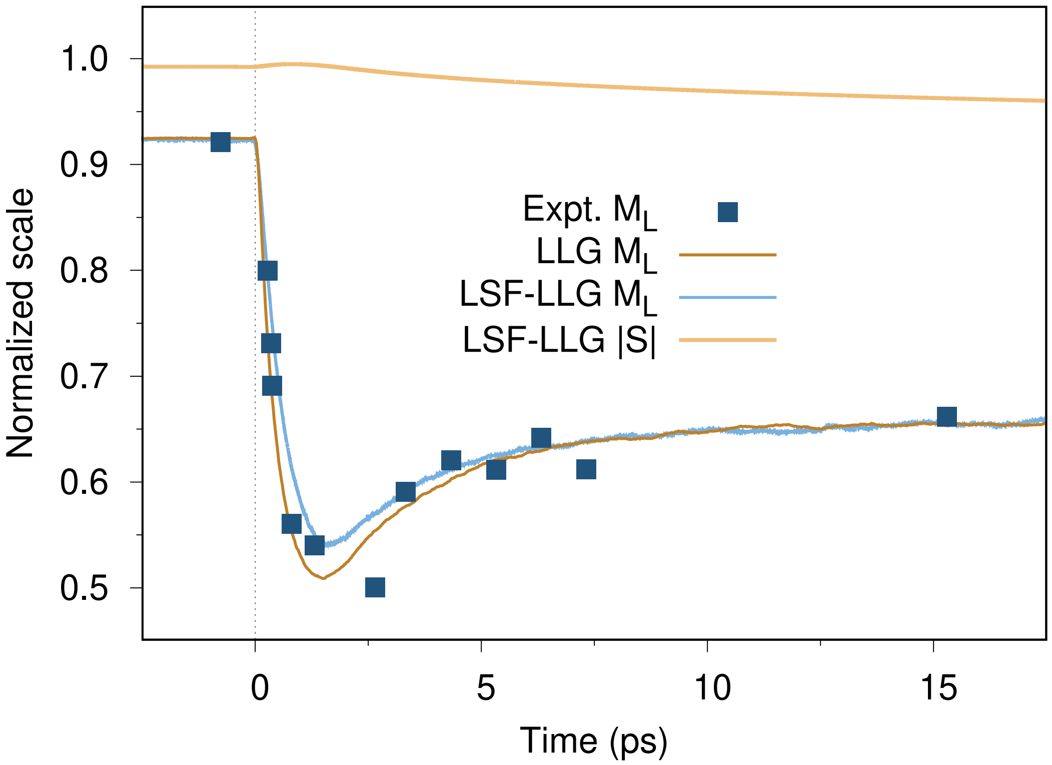

Fig. 4.8 The ultrafast demagnetisation of Ni is calculated with both the LLG and LSF-LLG integrator schemes, yielding similar results. It should be noted however that the longitudinal contributions of Ni leads to a difference between the two results. It can be seen that there is good experimental agreement.

the Ni spins. It should be highlighted, that the drastically different treatment of system temperature in this case via the two-temperature model requires the use of $F_\alpha = 0.06$ to appropriately match the magnetisation calculated via the LSF-LLG to that of the initial experimental magnitude before the pulse is applied. The demagnetisation calculation shows that there is excellent agreement between the experimentally obtained data and what is calculated by the LSF-LLG. This is attributed to the more strongly manifesting effects of the damping parameter λ as seen in figure 4.3. As a result, it can be shown that longitudinal degrees of freedom play an important role in modelling the energy dynamics that occur in demagnetisation processes of an ultrafast nature.

4.5 Summary

The idea of merging moment size changes to conventional atomistic spin models continues to show interest, given the continued development of models such as the LLB integrator. It has been shown to be important in less localised moments such as Ni, whereby the magnitude of μ_s is demonstrated to change significantly depending on the energy state of the spins. In this chapter, we have implemented three longitudinal integrator schemes, the LSF-LLG-Heun, LSF-LLG-RK4, and the LSF-MC, with each having slightly different characteristics to be able to verify their implementations, and so that they remain applicable to a wide range of calculations. In order to test the newly implemented models, the Landau Hamiltonian was constructed via an equilibrium-adjustment form that ensures an equilibrium spin length of $|S| = 1$ for Fe, Ni, Co, and Cr. Additionally, a challenge regarding the inconsistencies in the calculated T_C and T_N of all the materials were reconciled via an exchange coupling re-adjustment.

The results shown in this chapter were able to validate the implementation of the equivalent damping assumption between transverse and longitudinal moves for the dissipation term in the LSF-LLG, via the agreement of results between both the Heun and RK4 solvers in a single spin system. Afterwards, it was shown that the Boltzmann distributions recovered from the LSF-MC agreed with what was parameterised according to the Landau Hamiltonian for each material, defining the differences in behaviour for softer moments such as Ni amongst stiffer ones such as Fe. The exact temperature-dependent longitudinal spin length relationship was also shown to vary due to drastic changes in the magnitude of the exchange contribution under different temperatures. Additionally, the Boltzmann distributions verified the LSF-MC sampling routine, given that the appropriate phase-space was being sampled to recover the fitted Boltzmann probability function. The temperature-dependent magnetisation calculations further verified what was obtained by identifying the systematic T_C and T_N

discrepancy between the conventional and longitudinal integrator schemes. Additionally, the exchange re-adjustment methods were shown to give excellent agreement with T_C and T_N data measured experimentally. Finally, the ultrafast demagnetisation calculations of Ni proved that the inclusion of longitudinal dynamics is compatible in sub-picosecond calculations, giving good agreement with experimental results.

While the implementation of the LSF model has shown good agreement with expected results in this chapter, some areas of improvement remain, and are left to future work. For example, computing the Landau parameters for a larger variety of materials would aid in the general usability of the implemented calculations, as every species in general requires a recalculation of the Landau coefficients. Additionally, the LSF-MC integrator scheme is currently sampling longitudinal and transverse space collectively, via a uniform sampling scheme. This can be significantly more efficient via researching the appropriate phase-space measure to implement a split move sampling architecture, whereby both transverse and longitudinal moves can be independently tuned. Finally, while the LSF-LLG was shown to have been implemented appropriately given the Heun and RK4 solvers, it is still unclear whether the assumption of equal transverse and longitudinal damping parameters is valid.

5

The role of longitudinal spin fluctuations in FePt

5.1 Motivation

The incentive to pursue atomistic modelling of the magnetisation dynamics of FePt is important for the reason that it is a significantly used material in making magnetic recording media for the purposes of Heat Assisted Magnetic Recording (HAMR). This is in part due to its $\mathrm{L1_0}$ phase which has an exceptionally high anisotropy energy because it exists as exclusive layers of Fe and Pt stacked on top of one another. The delocalized Pt sites are strongly polarised by the localized Fe exchange field, and this unique exchange coupling arrangement contributes to this large anisotropy. The result of this is a breaking of cubic symmetry, and a preference of alignment along the stacking direction, referred to as the easy-axis [105]. The currently established atomistic modelling method employed to best replicate the collective behaviour of Fe and Pt in the same system was described by Mryasov *et al.*, where the primary assumption made is to treat the Pt sites as 'non-magnetic', and to reconstruct the effective spin Hamiltonian in Fe degrees of freedom, with adjustments to the anisotropy and exchange energies to accommodate the effects of Pt [30]. While this model proposes a reasonable approach when it comes to modelling ordered FePt structures, where it is guaranteed that every Pt site has equal access to the same amount of Fe nearest neighbours to couple with, it raises questions regarding the effectiveness of applying a blanket treatment of all Pt sites in systems where localized structure variations are random. The difficulty in modelling Pt as individual spin moments is because the currently used atomistic Landau-Lifshitz-Gilbert (LLG) and Monte Carlo (MC) integrator schemes both assume a fixed spin vector magnitude of $|S| = 1$. While this is mostly inconsequential for highly localised Fe sites, Pt sites show large degrees of delocalisation, manifesting as fluctuations in moment length. Not including the longitudinal contributions returns an incomplete picture as to the magnetisation dynamics of FePt as a whole, as the Pt degrees of freedom cannot be modelled otherwise.

The Longitudinal Spin Fluctuations (LSF) model introduced in chapter 4 was applied to FePt, which allows for moment length changes in Pt, which in turn allows for atomistic modelling of both Fe and Pt sites with their own degrees of freedom. The application of such a model to FePt is natural: Fe sites remain rather stiff longitudinally, however crucially provide a strong exchange field which polarises Pt sites, inducing longitudinal fluctuations, which account for a significant portion of its magnetisation contribution. By modelling the Pt degrees of freedom, considerations can also be made for site-dependent anisotropy calculations, via the Néel pair anisotropy model [106]. Instead of assuming a fixed anisotropy contribution determined by material species, a fully localised calculation of the anisotropy contribution dependent on nearest neighbours can be employed. This leads to more bespoke consideration of stoichiometric variations, especially at the surfaces of the simulated systems where fluctuations of the number of nearest neighbours are noticeable. Including the LSF model paves the way to atomistically modelling systems with any amount of disordering, given each system now has access to fully localised energy calculation schemes. Figure 5.1 shows a schematic of the primary differences between the Mryasov FePt model, and the LSF one.

The research presented in this chapter builds on the work in Mryasov *et al.* and makes suitable adjustments to utilise the established fundamentals of FePt to construct a model that enables the calculation of Pt degrees of freedom in order to realise a more physically appropriate representation of the system [30]. To build a fully realistic treatment of Fe and Pt, a Néel anisotropy model is derived, allowing for fully on-site calculations of anisotropy energy, moment length, and exchange contributions. The results in this chapter highlight temperature-dependent magnetisation changes that now correctly replicate T_C while also allowing Pt to behave as its own fluctuating moment. Finally, temperature-dependent magnetisation calculations for the A1 phase are shown to give an overview of one of the major strengths of the LSF model.

5.2 Longitudinal dynamics in FePt

5.2.1 The conventional FePt model

In order to build a holistic picture of the magnetic behaviour of FePt, the model introduced in Mryasov *et al.* is considered [30]. As the theory of this is covered in chapter 3, section 3.2, a recap of the key findings will be included. A crucial starting point to establishing the

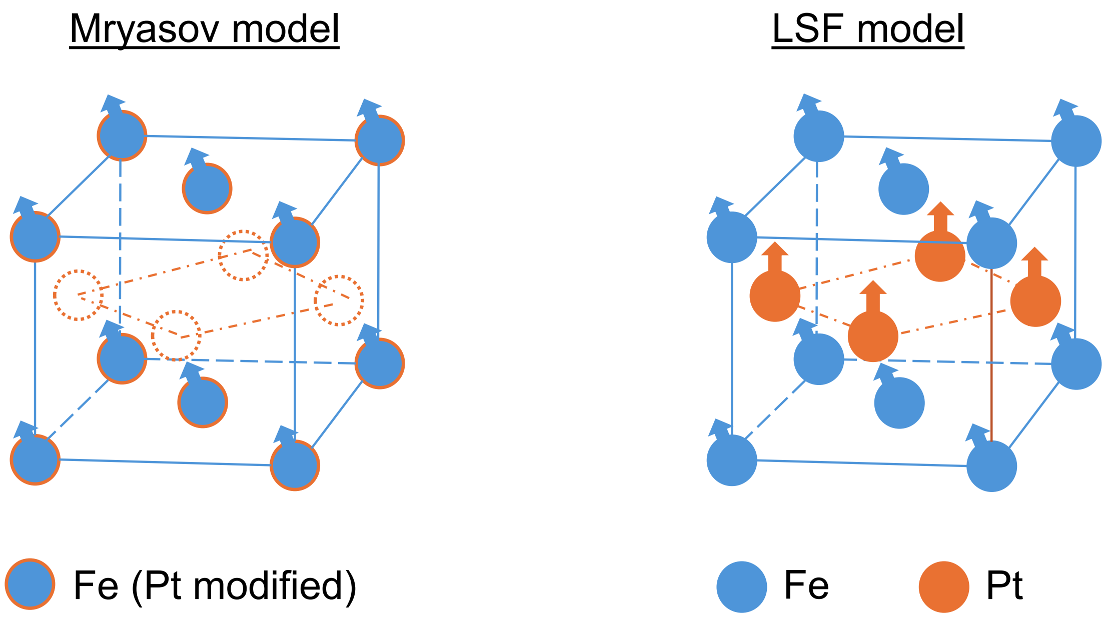

Fig. 5.1 A schematic representation of the LSF atomistic modelling scheme governing FePt, with the primary advantage of being able to include Pt degrees of freedom alongside Fe ones. In previous models the Pt sites were not given their own degrees of freedom according to the Fe exchange field.

Mryasov model for FePt begins by understanding the dichotomy of the behaviour of Fe and Pt. The strongly localized Fe sites induce a magnetic moment in the Pt sites via exchange coupling. As the Pt moments can be represented according to the effective field from the Fe sites via its susceptibility χ_{Pt} ($\mathbf{m}_{\mathrm{Pt}} = \chi_{\mathrm{Pt}}\mathbf{H}_{\mathrm{Fe}}$), the augmented effective exchange (and by extension anisotropy) parameters can be obtained by adding the Pt contribution to the Fe ones. The augmented energy terms can then be combined to construct an effective Hamiltonian that describes the energetics of $\mathrm{L1_0}$ FePt in solely Fe degrees of freedom, given by:

$$\mathscr{H}_{\mathrm{FePt}} = \sum_{i<j} J_{ij}^{\text{eff, 1nn}} \mathbf{S}_i \cdot \mathbf{S}_j - \sum_i d_i^{(\text{1-ion})} (\mathbf{S}_i^z)^2 - \sum_{i<j} d_i^{(\text{2-ion})} \left(\mathbf{S}_i^z \mathbf{S}_j^z \right). \tag{5.1}$$

It can be seen that this form of the effective Hamiltonian assumes that the Fe sites have equal access to Pt atoms, and is accounted for as simple augmentation to the Fe parameters by considering the total energy of Pt due to the Fe exchange field. This assumption is only valid in the highly ordered $\mathrm{L1_0}$ phase, and does not hold true in a disordered A1 phase. In order to deal with any form of randomisation introduced to FePt, the Pt moments have to be modelled as their own degrees of freedom, alongside the already magnetic Fe sites. In order to model Pt atoms it must be noted that Pt heavily relies on longitudinal degrees of freedom to gain a moment via the Fe exchange field. This is because under the strongly polarising Fe exchange field the otherwise non-magnetic Pt sites weakly react to directional changes in the total system, however they exhibit an increased magnetic moment to compensate. While the methods behind introducing longitudinal spin fluctuations has been introduced in detail in chapter 4, a recap of the relevant equations will be shown in the following part.

5.2.2 The FePt Landau Hamiltonian

To model longitudinal degrees of freedom, the Landau Hamiltonian for FePt and is given by the expression

$$\mathscr{H}_L' = \sum_i \sum_\alpha A'_\alpha |S_i|^2 + B'_\alpha |S_i|^4 + C'_\alpha |S_i|^6, \tag{5.2}$$

where A'_α, B'_α, and C'_α are Landau coefficients that describe a material specific relationship between system energy and an ordering parameter, which in this case is the spin length quantity $|S_i|$ at site i and material α. Given the band structure for Fe and Pt, the coefficients can be individually calculated such that they adequately replicate the changes seen to their moment length with respect to available system energy. It should be noted, that the exchange and anisotropy interactions between spin sites contributes to longitudinal changes, and thus should also be taken into consideration when forming the basis of the Landau coefficients. The summary of the total Hamiltonian parameters used are shown in table 5.1.

Parameter	Fe	Pt
μ_s (μ_B)	2.86	0.36
$J_{ij}^{\text{1-nn}}$ (Fe, Fe) (J/link)	3.30×10^{-21}	-
$J_{ij}^{\text{1-nn}}$ (Fe, Pt) (J/link)	1.07×10^{-21}	-
$J_{ij}^{\text{1-nn}}$ (Pt, Fe) (J/link)	-	1.07×10^{-21}
$J_{ij}^{\text{1-nn}}$ (Pt, Pt) (J/link)	-	2.83×10^{-23}
A' (J)	-7.91×10^{-20}	4.55×10^{-21}
B' (J)	3.03×10^{-20}	-
C' (J)	1.14×10^{-20}	-
λ	0.1	0.1

Table 5.1 Summary of FePt parameters used in the LSF calculations [50, 107].

The usually non-magnetic Pt sites are allowed to have their own degrees of freedom as a result of this model, as the direct contribution of the Fe exchange field will promote longitudinal changes to Pt that reflect moment growth proportional to that of its access to Fe nearest neighbours. As a result, the Mryasov model is extended from just modelling

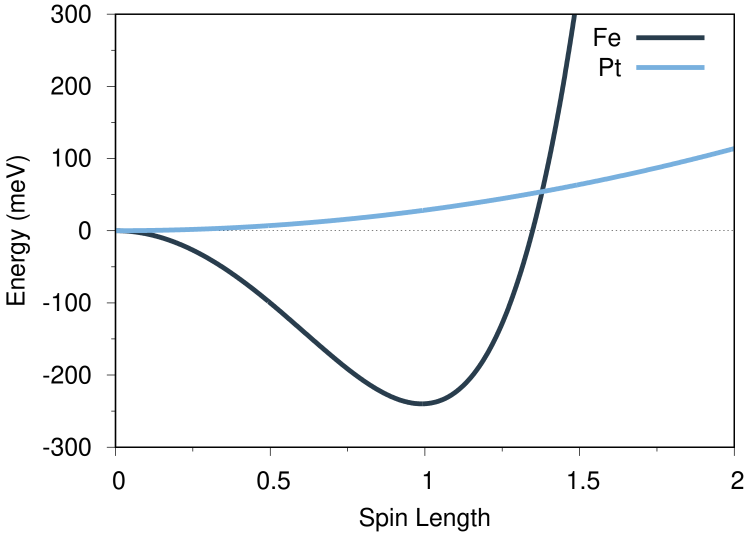

Fig. 5.2 Energy against spin length relationship for FePt. It can be seen that Fe is prominently centred around $|S| = 1$, whereas Pt starts at $|S| = 0$ without the addition of the effects of exchange. This approximation is attributed to Pt not having a magnetic moment in bulk, while Fe does.

Fe degrees of freedom with slight changes due to Pt, to being able to model both species. To visually represent the Landau coefficients used, figure 5.2 demonstrates the bulk, non-interacting longitudinal potentials for both Fe and Pt. It is evident that the Fe species remains a stiff moment, given a steep longitudinal potential well, while Pt is significantly shallow, leading to significant longitudinal changes. From a physical standpoint, this allows for the Pt potential to be perturbed by the Fe exchange field with ease. Additionally, without any interacting systems in place, Pt resorts to a moment length of $|S| = 0$ given by the energy minimum.

It is important to quantify the degree to which the Fe exchange field polarises Pt, resulting in an increase to its moment size. Due to $|S|$ being a normalised quantity ($|S| = 1$ at equilibrium), the average exchange field affecting Pt sites should modify the Pt potential accordingly. Variations in system stoichiometry will result in shifts to the equilibrium spin length values, and thus the Landau parameters should be recalculated given a deviation from the normalisation condition, with exact methods detailed in chapter 4. The joining of exchange, anisotropy, and longitudinal components allows for the coupling of all system energies to longitudinal fluctuations, which gives rise to moment length changes for both Fe and Pt species. It should also be noted that to introduce such dependence, the spin vectors $\mathbf{S}_i$ and $\mathbf{S}_j$ that configure exchange and anisotropy energies now take the form of the total spin vector $\mathbf{S} = \hat{\mathbf{S}}|S|$ rather than solely the unit vector description $\hat{\mathbf{S}}$, which assumes a constant

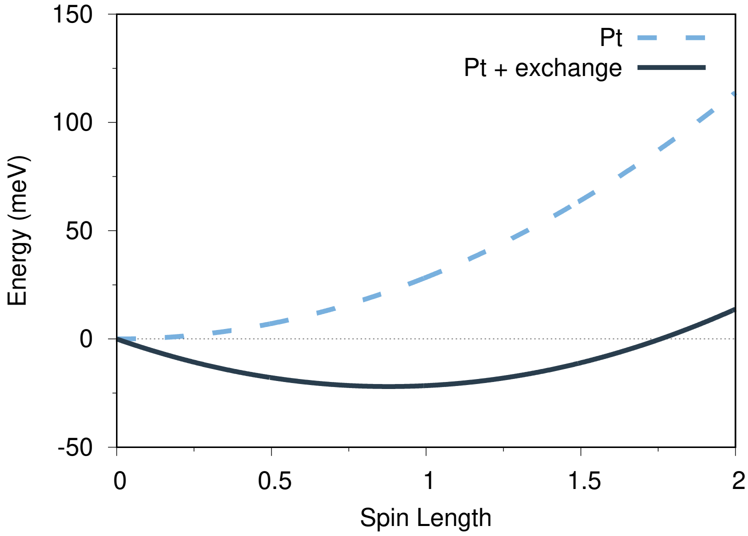

Fig. 5.3 The effects of the Fe exchange field on the Pt sites, shifting the energy minima going from $|S| = 0$ to $|S| = 1$. At equilibrium, the Pt longitudinal energy surface is parametrised such that the Fe exchange field gives it exactly $|S| = 1$ at $T = 0$ K.

spin length of $|S| = 1$. Without committing to the redefinition of the vector components, the exchange and anisotropy interactions would not be able to interact with changes to the moment length of spins, giving an incomplete depiction of the system.

To demonstrate the drastic change to longitudinal Pt energies given the presence of the Fe exchange field, figure 5.3 shows the longitudinal potential for Pt inclusive of the Fe exchange contribution. It can be seen that the normalisation condition is met, as with the exchange field from the Fe sites, the energy minimum rests at $|S| = 1$. As the system receives more available energy (via increased temperatures for example), it is allowed to explore more longitudinal configurations, leading to fluctuations in moment length. For the case of Pt, it exhibits strong fluctuations due to a shallow potential, which gives it access to a wide range of favourable states with even a small increase in energy.

5.2.3 Simulation methods

The introduction of additional degrees of freedom via modelling Pt atoms now requires re-configuring the simulated lattice environment, to accommodate the distinct features of both Fe and Pt material species independently. The crystal structure is set up using an FCC lattice, beginning with four unique sites that are initialised as Fe only. For the case of modelling $L1_0$ systems, the two sites which are not in the same plane as the reference atom are replaced with Pt, leading to exactly two Fe and two Pt in this simple unit. This is then repeated until the desired structure is generated. The flexibility of defining the system in this manner is evident once disordered phases are being investigated. In the case of the A1 phase for example, all four unique spin sites per lattice is given a 50% chance of being replaced with a Pt atom, leading to a fully random system. This also allows for slightly disordered phases, where each spin sublattice can have a percentage chance of being replaced with the opposite species. The process of generating disordered systems is shown in figure 5.4.

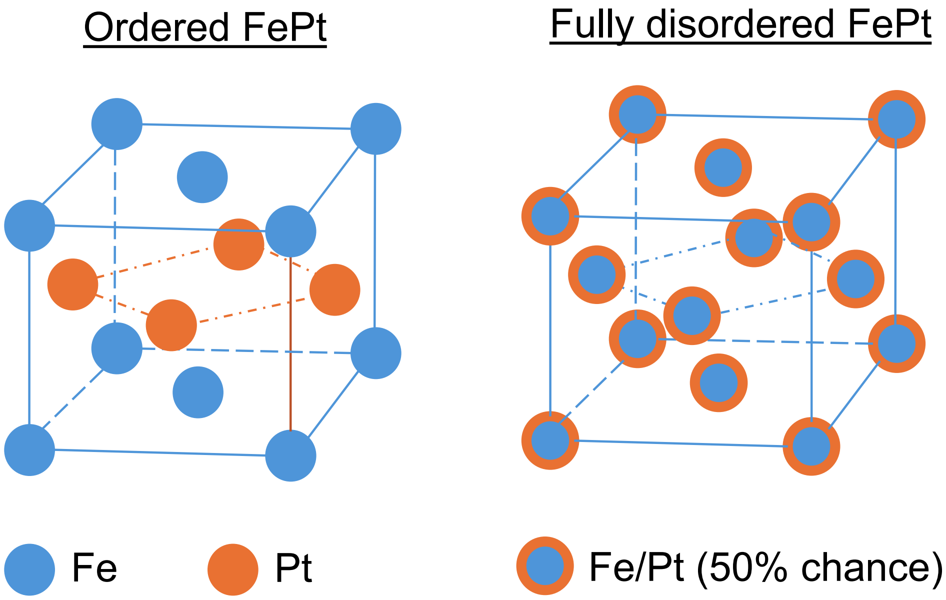

Fig. 5.4 Disordering can be introduced by including a probability of incorrectly swapping atomistic sites for the opposite species.

The pairwise exchange constants $J_{ij}^{\text{1-nn}}$ defined in such a system depend on both the reference spin site i, and the neighbouring spin site j. As a result, in a perfect bulk $\mathrm{L1_0}$ case, both Fe and Pt sites will have four in-plane neighbours of the same species, and 8 (4 above and 4 below) out-of-plane neighbours of a strictly different species. The exchange constants are implemented such that the computed T_C value replicates the experimental counterpart of $T_\mathrm{C}^\mathrm{FePt} \approx 700$ K, using values calculated in Ellis *et al.* for any Pt related interactions, and the mean-field approximation for pairwise exchange regulating Fe-Fe interactions The previously defined exchange adjustment methods in chapter 4 are not applied in this case, as this combination of exchange interactions yields an approximately correct $T_\mathrm{C} \approx 700$ K. In future work, it would be beneficial to expand on exactly what the reasoning for this from an electronic theory perspective, however given the complexity of the interactions between Fe and Pt species in this system it is left to future work.

5.3 Néel anisotropy model

In order to realise a fully localised calculation of the atomistic energies of FePt, the currently used uniaxial anisotropy energy calculation must be expanded to a more general form: utilising the nearest neighbour configuration to determine the anisotropy energies. This is a departure from the two-ion formulation devised in Mryasov *et al.* for the reason that the Pt moment has its own degree of freedom under the LSF model, and thus assumes no relationship to the Fe spins other than coupling via the standard exchange and anisotropy interactions. This becomes exceptionally crucial in magnetisation dynamics for high-temperature magnetic switching (demonstrated in chapter 6), where the anisotropy energy determines the magnetic orientation of a given system after relaxing from T_C.

5.3.1 The Néel anisotropy model for FePt

The standard uniaxial anisotropy calculation assigns an onsite anisotropy energy k_u to each material species, which has a magnitude given assumption that it will consistently have access to the same number of nearest neighbours. While in bulk L1_0 FePt this is the case, in finite systems with proportionally more surface effects this model fails to describe accurately the energetics of such a system. Additionally, any amount of disorder introduced would lead to an inconsistent number of Fe and or Pt nearest neighbours at a given site, and thus the averaged onsite anisotropy treatment is no longer valid.

The LSF model has the advantage of fully discretized treatment of individual spin sites with respect to their species, it is important to revise the anisotropy model to also come as fully localised energy calculation determined by access to nearest neighbours. This is done via the Néel model, which introduces a calculation at each spin site, summing the anisotropy energy contribution from individual neighbours. This gives rise to a variance of the anisotropy calculations in a system given positioning, disorder, and species clustering. The energy calculation according to the Néel pair anisotropy model is given by the following equation [106, 108, 109]:

$$\mathscr{H}_{\text{Néel}} = -\frac{k_{\text{Néel}}}{2}\sum_{ij}^{z_i}(\mathbf{S}_i \cdot \hat{\mathbf{e}}_{ij})^2, \tag{5.3}$$

where each spin site i has anisotropy energy from the sum of nearest neighbours j with total z_i. The value of $k_{\text{Néel}}$ describes the energy parameter associated with a single interaction of that given site with another neighbouring spin. In the case of L1_0 FePt, the Fe species contributes an in-plane anisotropy component, while proportionally Pt significantly overpowers this with an out-of-plane component. To model this behaviour, interactions going from an Fe to a

Pt site are considered to be negative, while Pt to Fe is positive. Utilising the Néel form of anisotropy calculations allows for explicit accounting of missing interactions that occur due to stoichiometric variations from site-to-site, and thus the calculations shown in this chapter focus on the new-found effects of fully discretizing an FePt system in the case of moment fluctuations, exchange coupling, and anisotropy energy.

5.3.2 Fourth-order Néel anisotropy

While equation 5.3 sufficiently describes uniaxial symmetries in systems, and retrieves the correct magnitude for cubic anisotropy cases, it fails to replicate the rotational symmetries in systems with cubic anisotropy. To verify for the disordered phases that the correct symmetry is obtained (not the magnitude), one must expand the Néel anisotropy calculation to include an additional term, defined by the following expansion [108]:

$$\mathscr{H}_{\text{Néel}} = -\frac{k_{\text{Néel}}}{2}\sum_{ij}^{z_i}\left[(\mathbf{S}_i\cdot\hat{\mathbf{e}}_{ij})^2+(\mathbf{S}_i\cdot\hat{\mathbf{e}}_{ij})^4\right]. \tag{5.4}$$

The complexity of equation 5.4 is further to that described, as introducing a fourth order term requires that the proportion of its contribution is regulated with respect to the second order form. The coefficients required are not calculated in the research presented, and is left to future work. As a result of this, the calculation of the anisotropy energy will be left to the form shown in equation 5.3, while equation 5.4 was used to verify the correct symmetries are present in a given system. The comparison of only second-order *vs.* second and fourth-order terms in a fully disordered bulk A1 FePt system is shown in figure 5.5. The data was obtained by setting the azimuthal angle $\theta = 90°$, and rotating the spins in-plane ($\phi = 0°$ to $360°$). It can be seen that the second-order form produces an in-plane easy-axis, which in the disordered case without any lattice compression should not be able to occur. The fourth-order variant of the same calculation reproduces the correct cubic symmetries, albeit with an incorrect magnitude as the calculations did not include a coefficient that regulates this additional symmetry term. Utilising the second order form in future calculations does not pose a significant unaccountable difference in the results obtained, as in practical terms the magnitude of the cubic anisotropy (as seen in the second order calculation) is significantly smaller relative to the out-of-plane term in the more ordered phases of FePt [110]. The majority of the interest with the Néel pair model applied to FePt in chapter 6 is for calculations involving Heat Assisted Magnetic Recording, which make use of the much larger uniaxial anisotropy component of FePt systems. It is worth noting, that there is a slight offset of the minimum (and maximum) energy points in both second and fourth order calculations.

This is because the exact proportion of Fe and Pt atoms is not exactly 50%, and thus some misalignment is expected.

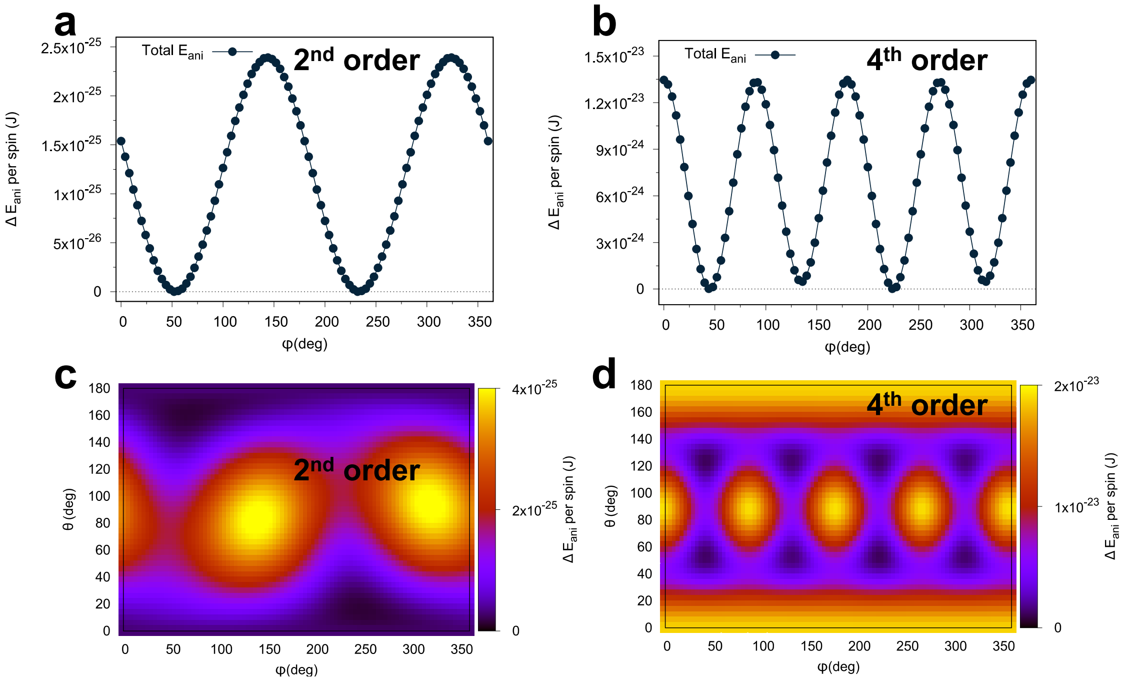

Fig. 5.5 Comparison between second (a), (c) and fourth order (b), (d) Néel forms, showing clearly that in order to extract the cubic symmetries in disordered FePt, a fourth order Néel term must be employed, as the asymmetric second-order result does not reflect cubic symmetries appropriately.

The value of $k_{\text{Néel}}$ and the 3D anisotropic symmetries for a given structure can be calculated by forcing the spins into a range of specific orientations, such that the variation of anisotropy energy against θ (azimuthal angle; between a range of 0° to 180°) and ϕ (in-plane rotational angle; between a range of 0° to 360°) are fully realised. The coordinate convention is spherical polar coordinates, and is defined in figure 5.6.

From Mryasov *et al.*, DFT calculations show that the uniaxial anisotropy constants (k_u) for Fe and Pt in FePt are -1.55×10^{-23} J/atom and 2.28×10^{-22} J/atom respectively [30]. In order to obtain the correct pairwise Néel coupling energy terms ($k_{\text{Néel}}$), the angular variation of the total anisotropy energy obtained via using the onsite terms must be equal to the same calculation using the Néel anisotropy model. From this, a value for $k_{\text{Néel}}$ can be obtained for Fe and Pt by comparing the energy configurations by material species. Figure 5.7 shows the energy differences with respect to azimuthal angle θ for both the onsite uniaxial and Néel cases, and table 5.2 summarises the $k_{\text{Néel}}$ parameters obtained. This was done for a bulk $L1_0$ FePt system. It can be seen that the calculations comparing Néel and onsite anisotropy energy variations match exactly, which shows that the Néel pair calculations given

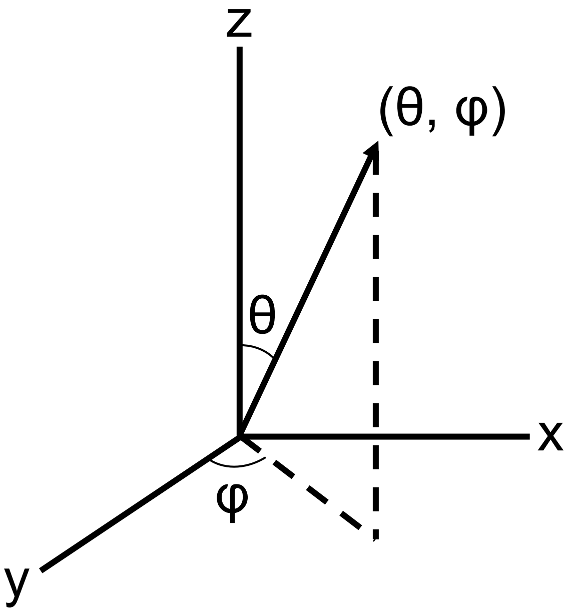

Fig. 5.6 Schematic of spherical polar coordinate system employed in computing spin vectors given the azimuthal and in-plane rotational angles.

the right coefficients exactly reproduces the findings in Mryasov *et al.* [30]. This enables the extension of the Néel anisotropy model to disordered systems, as the LSF discretization of FePt allows for consideration of all spin sites, which means a fully localised resolution of the anisotropy energy can be calculated.

Parameter	Fe	Pt
k_u (J/atom)	-1.55×10^{-23}	2.28×10^{-22}
$k_\mathrm{Néel}$ (Fe, Pt) (J/neighbour)	-7.76×10^{-24}	-
$k_\mathrm{Néel}$ (Pt, Fe) (J/neighbour)	-	1.14×10^{-22}

Table 5.2 Summary of anisotropy parameters used for LSF FePt simulations.

5.4 Results and discussion

5.4.1 Disorder-dependent FePt anisotropy

A primary interest of FePt related research is the anisotropy energy relationship against the chemical ordering parameter s, given by the expression

$$s = 1 - 2p, \tag{5.5}$$

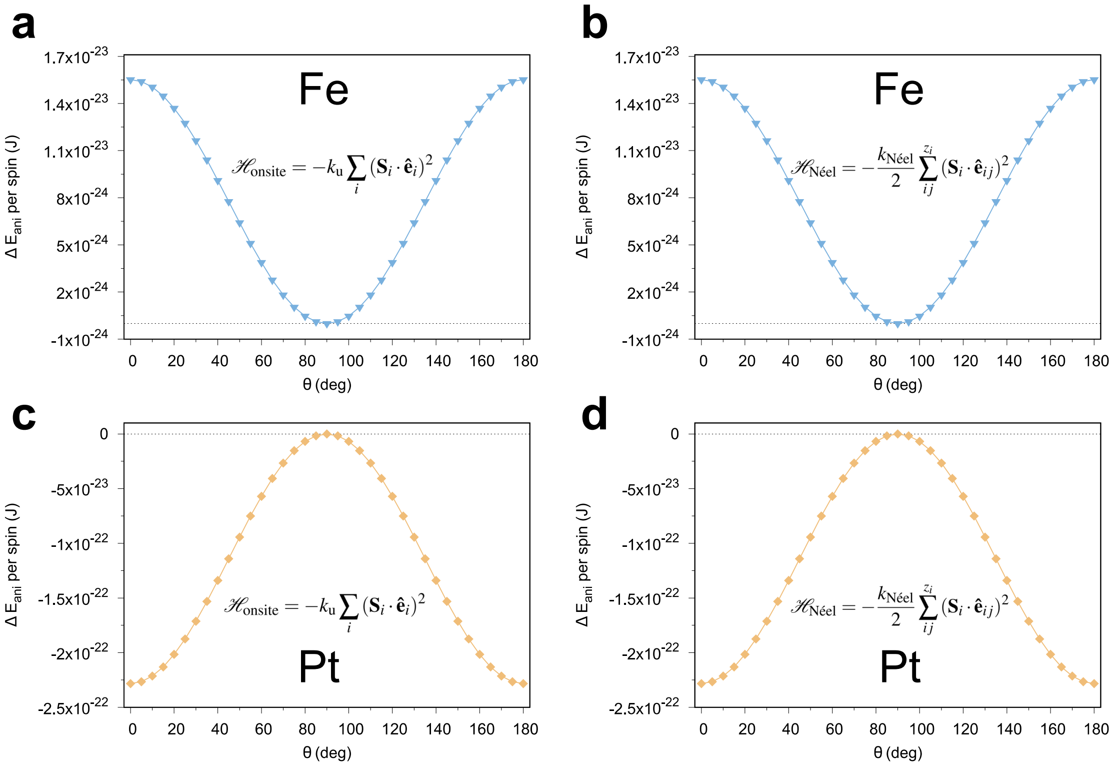

Fig. 5.7 (a), (c) Anisotropy energy varying with the azimuthal angle for an onsite anisotropy energy model. The maximal difference between the energy states was used as a reference to obtain the Néel pair anisotropy values for both Fe and Pt in (b), (d).

where p is the probability of finding a Pt atom in an Fe site, or an Fe atom at a Pt site with reference to a perfect $\text{L}1_0$ structure. This yields $s = 0$ for the fully disordered A1 state, and $s = 1$ for the fully ordered $\text{L}1_0$ state. Disorder dependent anisotropy is crucial from the practical standpoint, as it is shown that during the production of FePt media for magnetic recording purposes, naturally occurring disorder manifests in the annealing process [24]. Thus far, the level of atomistic detail achieved for FePt was heavily limited by the suppression of the Pt degree of freedom, such that the anisotropy configuration had to be considered as an effective modification of the Fe parameters. This is hindered by the underlying assumption that all Fe sites have consistent access to the same number of Pt sites. In a more localised sense, all of the uniaxial contributions in FePt occur via the Pt $\rightarrow$ Fe (Pt in the presence of Fe neighbours) Néel pair interaction, which means that there is a heavy reliance on how dispersed or concentrated certain species clusters are. The Fe $\rightarrow$ Pt interaction on the other hand provides the effective in-plane component, however this is significantly smaller than the easy out-of-plane contribution.

The $L1_0$ phase demonstrates uniaxial anisotropy because Pt is guaranteed 8 Fe neighbours (4 each, in the planes immediately above and below it) located along the z-axis. As the system tends towards a more disordered A1 structure, the guaranteed bonds are lost, along with the directional bias along an axis, thus the exclusively uniaxial behaviour is converted into cubic. Figure 5.8 illustrates this Néel bond loss process, with the number of bonds denoted by $n_{\text{Néel}}$.

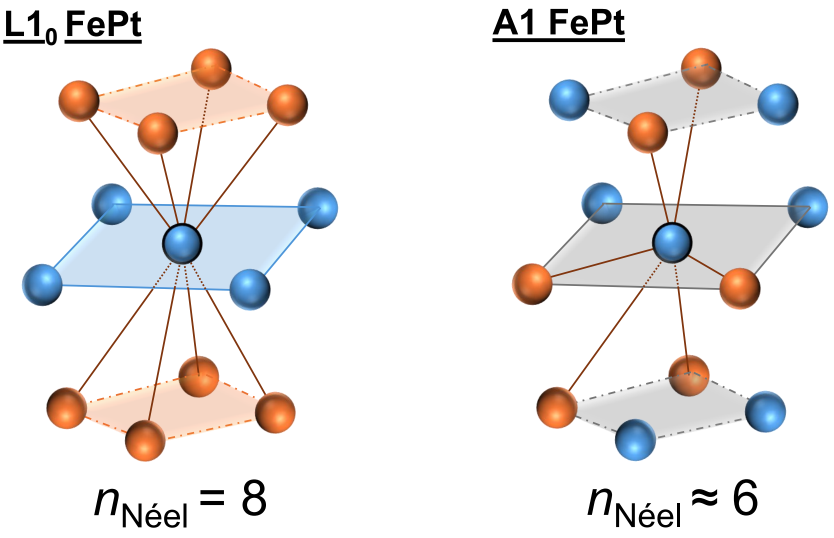

Fig. 5.8 A schematic diagram showing the Néel pair bond loss process that occurs when FePt goes from an ordered to a fully disordered state. As the system tends towards a disordered lattice, the average number of spin pairs that can be described drops from $n_{\text{Néel}} = 8$ to approximately $n_{\text{Néel}} = 6$.

Figure 5.9 realises the full energy surface symmetries using the fully atomistic Néel pair anisotropy model. This was done for a bulk system, with equal lattice constants $a = 3.861$ Å, determined in Meyer *et al.* [75]. It can be seen that the $L1_0$ form expectedly has no dependence with the angle ϕ, while the uniaxial easy-axis anisotropy manifests with respect to θ. This demonstrates correct implementation of the ordered and disordered forms of the pair anisotropy model. It should be noted that the magnitude of cubic anisotropies via using the fourth-order Néel pair anisotropy model are significant, however this has shown to not be the case in FePt, and thus the fourth-order results are simply used to verify the angle-dependent symmetries of the disordered system [110]. The rest of the calculations taking place will be solely using the second-order form, so as to obtain the expected uniaxial out-of-plane magnitudes.

Figure 5.10 shows a more detailed relationship between the anisotropic energy behaviours and s. In order to compute intermediate forms of disordering between the $L1_0$ and the A1

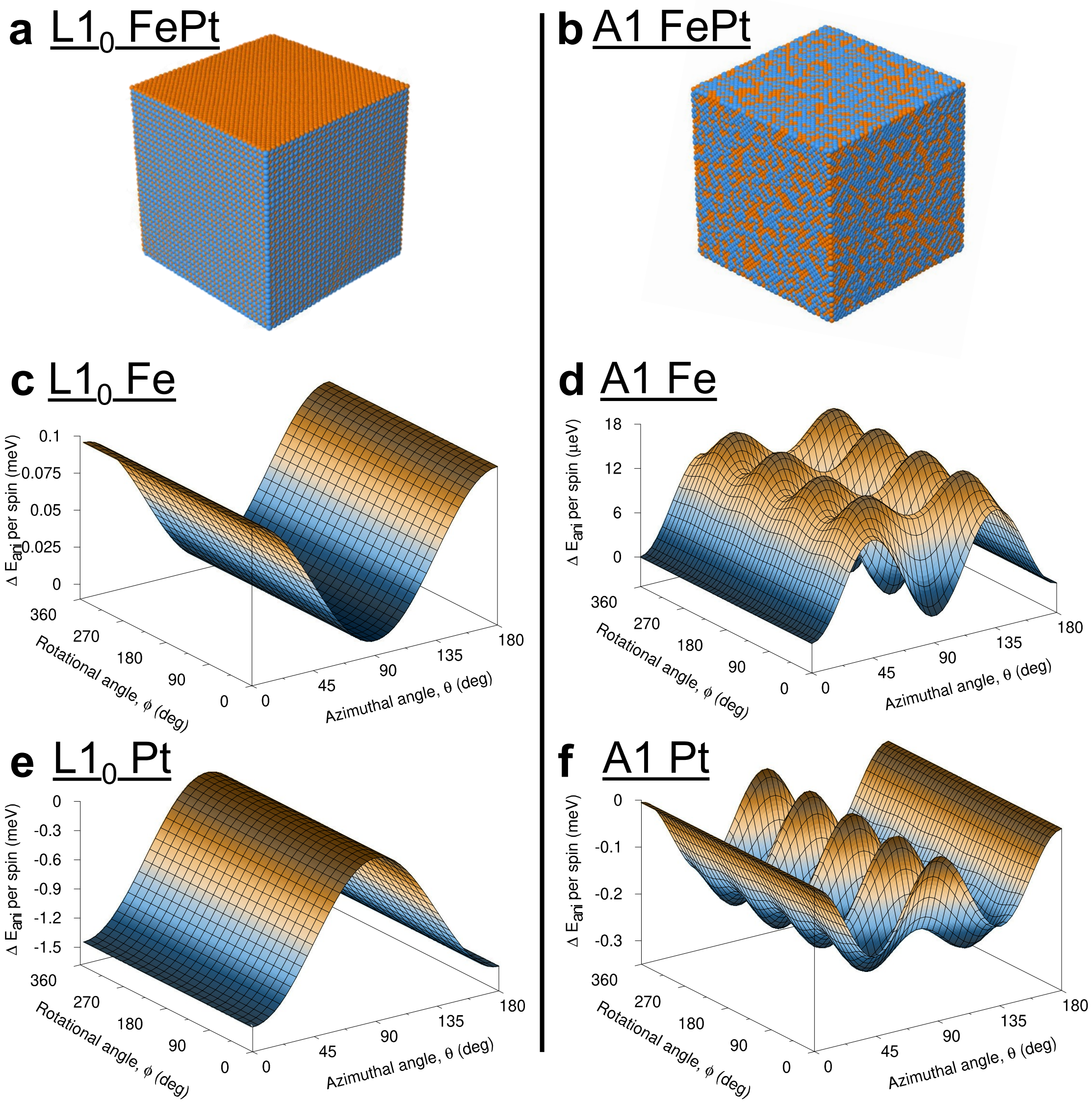

Fig. 5.9 Anisotropy symmetries pertaining to the fully ordered (L1$_0$) (a), (c), (e) and fully disordered (A1) (b), (d), (f) phases of FePt. The existence of a cubic phase is realised in the disordered system and is otherwise absent in the ordered one. It should be noted that in order to extract the correct symmetries, the fourth-order Néel pair model was used for the A1 system.

phases, bulk systems of varying s have their spin configurations varied from $\theta = 0°$ (spins aligned with the direction vector [001]) to $\theta = 90°$ ([100] direction). By computing the anisotropic energy difference between these two spin configurations, the energy per functional unit (f.u) can be extracted, which shows a clearly increasing trend going from fully disordered $s = 0$ to fully ordered $s = 1$. The resultant calculations agree well with what was obtained

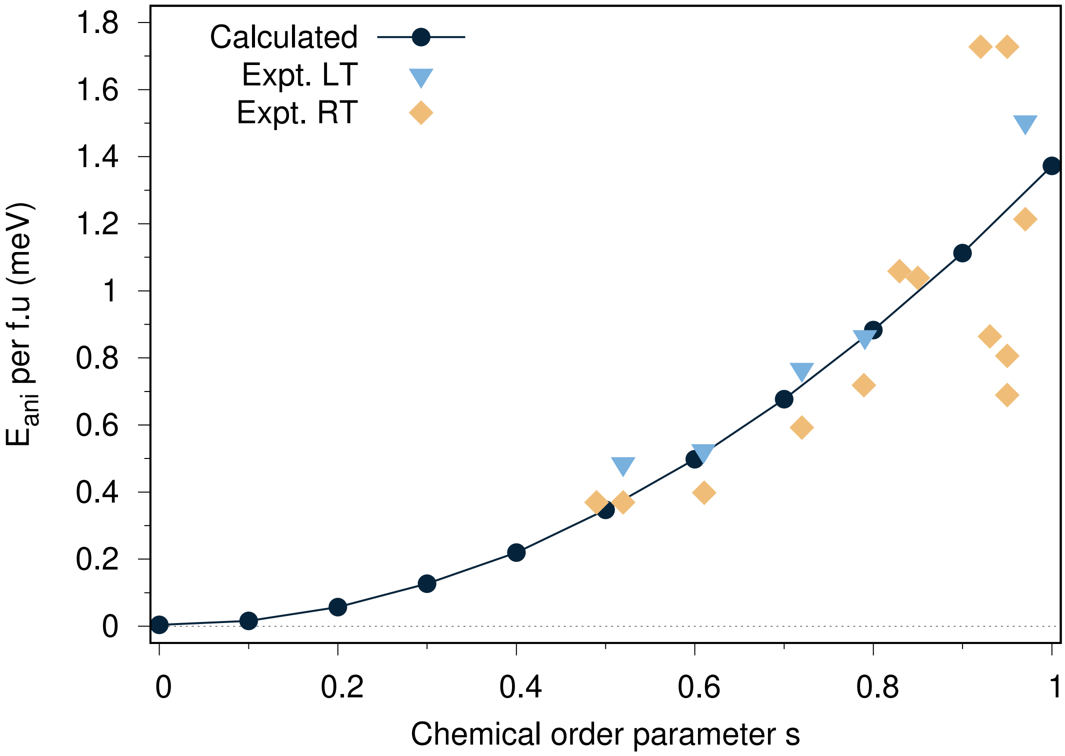

Fig. 5.10 The difference between the anisotropy energies of spin directions [001] and [100] against chemical ordering parameter s, showing clearly that increasing disordering leads to a significant penalty in uniaxial alignment. The data points calculated are in agreement with low temperature (LT) experimental data from Okamoto *et al* [32]. The room temperature calculations were collated in Wolloch *et al* [111].

experimentally by Okamoto *et al.* in the low temperature (LT; $T = 10$ K) regime [32]. Additionally, the room temperature (RT; $T \approx 300$ K) experimental calculations compiled in Wolloch *et al.* establish a reasonable trend with respect to the calculated data [111]. It should be noted that the atomistic calculations done in this thesis related to anisotropy are purely at $T = 0$ K, and thus some deviation is expected from RT measurements. It is estimated that E_{ani} per f.u decreases by approximately 20 to 30% going from LT to RT systems [111]. Verifying the experimental data from Okamoto *et al.* has been demonstrated a few times via coherent potential approximation (CPA) calculations [112, 113]. The express advantage of an atomistically resolved method demonstrated here is that it is more usable given small variations of the same general system. CPA is also limited to smaller system sizes due to computational constraints. An additional interest of research on FePt is the anisotropy dependence with respect to varying the concentration of Fe and Pt in the system [114]. With the clearly defined Néel pair anisotropy model that is in good agreement with experimental data as shown, calculations for different species concentrations can be done as an extension to what is shown in this chapter in a fully atomistic framework.

5.4.2 Induced Pt moment behaviour in FePt

Using the longitudinal spin fluctuations model, the temperature-dependent magnetisation properties of FePt can now be realised including both Fe and Pt degrees of freedom, as is shown in figure 5.11. By calculating the species-dependent normalised magnetisation against temperature for a 6 nm × 6 nm × 6 nm system using the LSF-MC integrator scheme, with 5000 equilibration timesteps and 35000 loop timesteps, the appropriate Pt behaviour is recovered. It can be seen that the Pt sublattice magnetisation follows exactly that of the Fe sublattice with respect to increasing temperature, reflecting fully the physical nature of FePt: the Fe exchange field strongly polarises the Pt sublattice, which is the source of its moment. The induced moment nature of Pt means that as a result of the spin re-orientation brought on by the disordered Fe sites, it has to grow significantly in spin length $|S|$, which leads to $M(T)_{\mathrm{Fe}} \approx M(T)_{\mathrm{Pt}}$. This behaviour is directly attributed to the longitudinal potential well of Pt described by the Landau expansion, where Pt only has an A_α coefficient for the second order spin length term $|S|^2$. This means that as the Fe sublattice disordering increases with increasing temperature, Pt loses its strong coupling to the Fe sites. As a result, the longitudinal energy curve seen in fig 5.3 reverts back to the exchange-less form, with the energy minima at $|S| = 0$. The increased system temperature however now allows more states to be explored along the potential well than compared to equilibrium, and thus the Pt spin length is forced to trend towards higher values past $|S| = 1$. It can be seen that the LSF model now exactly replicates what is expected from theory, which is that the Pt species only gains a moment according to the Fe exchange field, and this is reciprocated in the system magnetisation calculation [30]. The temperature-dependent magnetisation results obtained show good qualitative agreement with what was obtained by Ellis *et al* [50]. It should also be noted that the Landau coefficients have undergone a correction at equilibrium as per the methods highlighted in chapter 4, which is necessary as the equilibrium value for $|S|$ must be 1 to ensure a normalised reference moment.

To ensure that the LSF-MC integrator scheme fully samples the required longitudinal phase space as defined by the Landau Hamiltonian, the Boltzmann distributions of FePt were computed in figure 5.12. This was done by isolating a single-spin of either Fe or Pt with their respective Landau coefficients, and binning the evolution of their spin length states with respect to temperature. This was done for 5×10^6 Monte-Carlo moves, which was enough for all the possible states to become saturated.

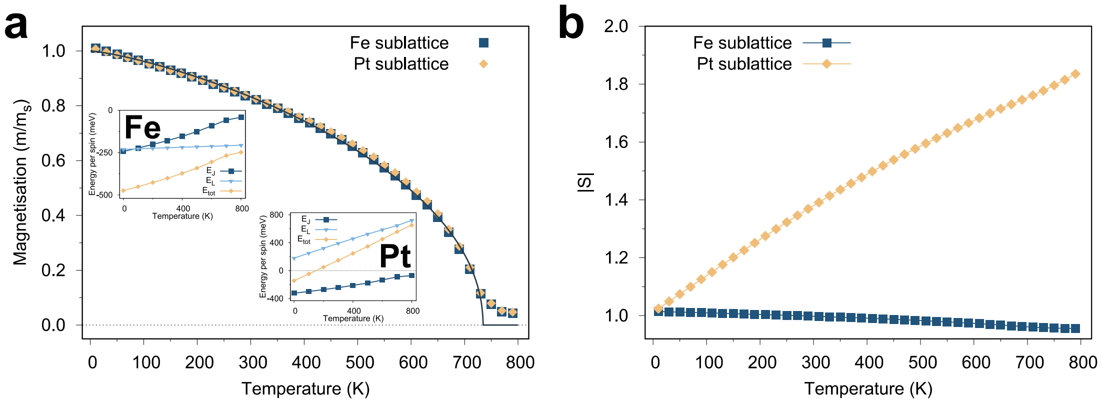

Fig. 5.11 temperature-dependent magnetisation calculation via fully discretized atomistic dynamics of Fe and Pt moments. It can be seen that both Fe and Pt sublattices exactly overlap with regard to their temperature-dependent magnetisation values in (a), due to a compensatory increase of the Pt $|S|$ seen in (b).

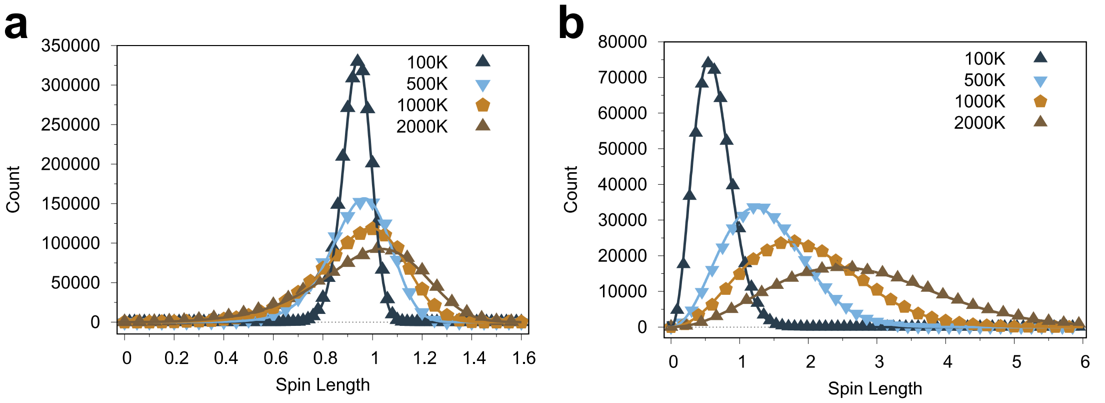

Fig. 5.12 Boltzmann distributions of Fe (a) and Pt (b) longitudinal energy states with respect to temperature. The stronger Fe moment is shown to have a much smaller distribution width, whereas Pt demonstrates drastic changes in $|S|$ as it is considered to be more easily polarised.

It can be seen that the expected temperature-dependent longitudinal behaviour is recovered exactly as per the Landau Hamiltonian, where it is seen that the steep Fe potential well prevents significant motion outside of its equilibrium spin length, whereas Pt exhibits behaviour that corresponds to low energy requirements to traverse longitudinal phase space. The significant broadening of the Pt distributions with increasing temperature is validated by the temperature-dependent calculations done in figure 5.11 (b), showing a significant increase in moment length. While broadening also occurs for the Fe distribution, it is significantly narrower than what is calculated for Pt.

The temperature-dependent calculations done under the longitudinal framework utilising the Landau Hamiltonian allows for a new look at simulations of interest relating to

Heat Assisted Magnetic Recording (HAMR). By modelling both Fe and Pt atoms and crucially being able to extract their induced moments, new insight can be obtained into the individualised contributions of Fe and Pt to the paramagnetic state at T_{C}, which is important in modelling more physically representative magnetic recording media that include defects and intermixing of layers [115]. Chapter 6 employs the longitudinal spin dynamics framework for HAMR calculations, fully realising the methods discussed in this chapter.

5.5 Summary

This chapter introduces the approaches taken to fully discretize the currently understood behaviour of FePt, by firstly defining longitudinal degrees of freedom using the Landau expansion, and secondly redefining the treatment of FePt's anisotropy framework, which relied on the two-ion form, alongside its usual inherently in-plane contribution in the case of the $\mathrm{L1_0}$ phase. The Néel form was introduced with both the second and fourth-order expansions to be able to investigate the magnitude and symmetries of more disordered phases. The Néel pair model was able to reproduce the expected symmetries in the fully disordered A1 phase via the fourth-order expansion, however it is noted that the cubic anisotropy energy reflects an incorrect magnitude due to the lack of a fourth-order coefficient. Regardless, the second-order expansion was employed to compute the uniaxial easy-axis anisotropy energy of FePt with respect to its disordering, and calculations recovered what was measured experimentally. The temperature-dependent magnetisation properties of FePt were investigated via the longitudinal spin fluctuations model, and the expected Pt behaviour was recovered, whereby its induced moment nature means it is reliant on the Fe sites to obtain a magnetic moment and thus a normalised magnetisation measure. The magnetisation against temperature calculation confirmed this overall behaviour, and the moment growth of Pt was demonstrated to have occurred according to its shallow longitudinal potential well, which is easily shifted according to the Fe disordering.

6

Atomistic simulations of HAMR including Longitudinal Spin Fluctuations

6.1 Motivation

A major constraint of HAMR in the practical capacity, is the challenges faced with ensuring the magnetic recording medium produced is as uniform in nature as possible. The annealing process required to produce $L1_0$ FePt has shown to accidentally introduce clusters of the disordered A1 phase, or of more Fe or Pt than intended, which has a significant effect on the variability of the T_C and K of grains produced [24, 114]. Calculating the atomistic resolved details of HAMR processes has garnered increasing interest over recent years, given the computational capabilities to resolve such large systems in atomistic units [28, 115]. The primary use of such simulations is to obtain information on the smallest-scale interactions that occur to cause overall emergent behaviour regarding data-storage performance. A shortcoming of currently established models for FePt recording media is the lack of a fully atomistic framework that gives full degrees of freedom to both Fe and Pt sites. Thus far in the thesis, the discussion has focused around moving away from a partly-atomistic model to a fully discretized one, with the introducing of Pt degrees of freedom using the Longitudinal Spin Fluctuations (LSF) model. The degree to which Pt gains a moment and thus contributes to the overall magnetisation state of FePt grains is determined exclusively by the number of Fe (and by extension Pt) neighbours a given site has. By including the fully localised integration schemes tested and shown in chapter 4, and further developing the localised FePt anisotropy model in chapter 5, atomistic simulations can be conducted into the macroscopic effects of more nuanced stoichiometric variations. This is of particular interest, as previous models were unable to provide this level of resolution in investigating the large-scale effects that emerge from atom-level variations in grain structure.

The investigation in this chapter begins by identifying the overall anisotropic energies seen in individual grains with varying levels of disordering. This is crucial as it is used to verify the correct finite-size implementation of the Néel pair anisotropy model implemented in chapter 5, while providing a qualitative overview of the expected evolution of the uniaxial energies with respect to system disordering. Afterwards, calculations were done to determine the type of longitudinal behaviour that FePt undergoes during the magnetic switching process, showing in particular the spin length evolution of Pt spins, as their induced moment nature has not been calculated before during the dynamics of switching. Given the significant effects that grain dimension variance has during the recording process, calculations of grain easy-axis distributions were done in this chapter [22, 23]. While the size dependence of grains has previously been investigated, HAMR systems are also strongly affected by their grain easy axis distributions [83]. This is because the readout signal during the reading process is less error-prone if there is consistently perpendicular alignment of the grains' magnetic fields. Maximising the easy-axis angle to be as close to $\theta = 0^\circ$ is important in ensuring the grains do not interact with each other's spin configurations, causing unwanted domain formation. Lastly, fully atomistic HAMR calculations with both Fe and Pt moments being modelled highlight the viability of the LSF model for use in parametrising HAMR for future practical use. An example is shown without any disordering as a verification to the bit pattern obtained in chapter 3, and a comparison is also shown between grains with different levels of disordering to determine the effects of writing data with $s < 1.0$. The investigation qualitatively ties into the aspects of the magnetic recording trilemma introduced in chapter 1, and demonstrated via HAMR calculations in chapter 3.

6.2 Single grain anisotropy energies

The Néel pair model implemented for use in the LSF FePt model is detailed prior to this chapter, however a recap of the key parameters for this model will be included here. The computation of the Fe and Pt $k_{\text{Néel}}$ parameters were done in chapter 5 by comparing the bulk uniaxial anisotropy energy per spin of both Fe and Pt for both the calculated $k_{\text{Néel}}$ values, and what was obtained via only using k_{u} from Mryasov *et al* [30]. This gave values of $k_{\text{Néel}}^{\text{Fe}\to\text{Pt}} = -7.76 \times 10^{-24}$ J/neighbour and $k_{\text{Néel}}^{\text{Pt}\to\text{Fe}} = 1.14 \times 10^{-22}$ J/neighbour. The Pt → Fe denotes that this value of $k_{\text{Néel}}$ is used when an interaction is defined to be from $i = \text{Pt}$ to $j = \text{Fe}$, and vice versa. It should be noted that this chapter only includes contributions from the second-order form of the Néel anisotropy implementation.

Figure 6.1 shows the anisotropy energy calculations of grain systems with variable diameters and heights, and additionally varied according to the chemical ordering parameter

s. The calculation was done by calculating the anisotropy energies by varying θ between 0° to 90°, and computing the anisotropic energy difference between the two states. The calculations show a strict reliance on the uniaxial energies present based on the disordering parameter, which is expected. While the uniaxial anisotropy decreases dramatically with small changes to s, the cubic symmetries are still fully present in the more disordered systems, although their magnitude and effects are not fully realised in this data. At $s \approx 0$, an effect can be seen whereby the E_{ani} per f.u data shows negative values. This was reproduced in Staunton *et al.* and occurs due to a variation in the lattice parameters used in these calculations [113]. More specifically, in chapter 5 the bulk case of FePt was considered where the lattice constant was set to be equal in all directions with the value $a = 3.861$ Å. In these finite systems, the lattice constant was assumed to take the fully experimentally measured value of $a = 3.861$ Å with a compression on the z-axis leading to $c = 3.788$ Å [75]. A detailed description of this behaviour is left to future work.

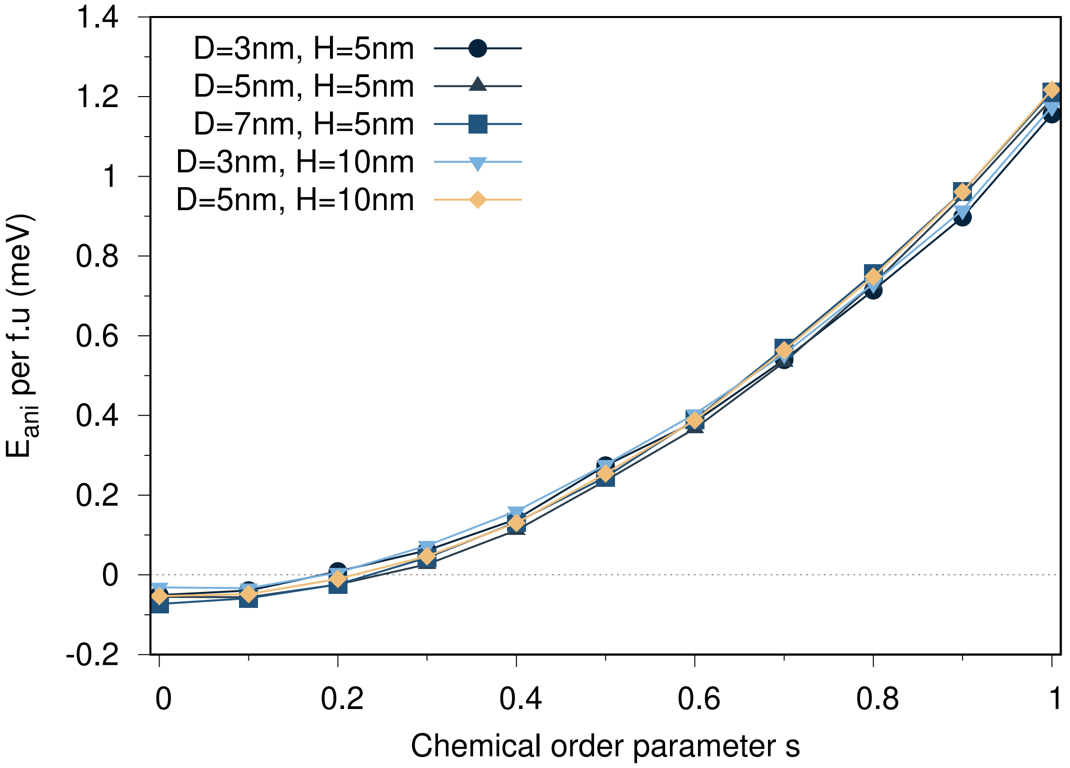

Fig. 6.1 Uniaxial anisotropy energy with respect to chemical ordering parameter s varied by grain dimensions. E_{ani} was computed as the difference between the anisotropy energies when all spins are parallel and perpendicular to the easy-axis. There is good agreement between the different system sizes.

6.3 Longitudinal fluctuations in magnetic switching

Single grain switching calculations rely on simulating a single isolated grain undergoing the HAMR recording process. This involves a temperature pulse thermally exciting the spins, and with a persistently acting write field of 1T in the [00-1] direction, the reduction of temperature-dependent anisotropy brought on by disordering causes a flip in the overall magnetisation direction of the grain. It is useful to demonstrate switching capabilities in the case of singular grains, as it allows for a more detailed look at the atomistic behaviour across the recording process, which inevitably informs the performance of the simulated full recording media. A grain of dimensions $D_{\text{grain}} = 5$ nm and $H_{\text{grain}} = 5$ nm was simulated across 600 ps, with timestep size $\Delta t = 1 \times 10^{-15}$ s. The time-dependent temperature pulse is defined by the function

$$T(t) = T_a + [T_{\text{peak}} - T_a]F(t), \tag{6.1}$$

where T_a describes the ambient temperature at 300 K, and T_{peak} is the peak temperature which in this case was 700 K. The Guassian function F(t) is then defined as

$$F(t) = \exp\left[-\left(\frac{t - 3t_{\text{pulse}}}{t_{\text{pulse}}}\right)^2\right], \tag{6.2}$$

which becomes maximal at $3t_{\text{pulse}}$, with standard deviation $\sqrt{2}t_{\text{pulse}}$. The Longitudinal Spin Fluctuations (LSF) model introduced in this thesis significantly bolstered capabilities of demonstrating its use in a fully atomistic model of FePt. The key factor of importance was the significant longitudinal fluctuations that Pt undergoes, due to the strongly polarising Fe exchange field, which effectively gives rise to its own moment and degrees of freedom. In HAMR, a key demonstration would be to investigate the behaviour of the Pt moment as changes in its moment size, as its participation in the overall switching process for FePt was not currently known. Figure 6.2 shows the switching calculations using the fully discretized FePt model, via the LSF-LLG integrator scheme.

The results of single grain switching show a trend that is clearly expected. Disordered systems lead to less efficient switching, as with an increasing value of s, more instability occurs. This is shown by the increased fluctuations in the magnetisation direction that tend to manifest around the peak of the pulse at approximately 300 ps. It is interesting to note, that the Pt $|S|$ understandably starts at $|S| \approx 1.4$, and quickly rises to $|S| \approx 1.6$ shortly after the pulse. This demonstrates that the maximal point of Pt's moment is not as the switching is occuring, but rather about 50 ps after. This can be attributed to Fe's sublattice magnetisation, which is minimal at the peak of the pulse.

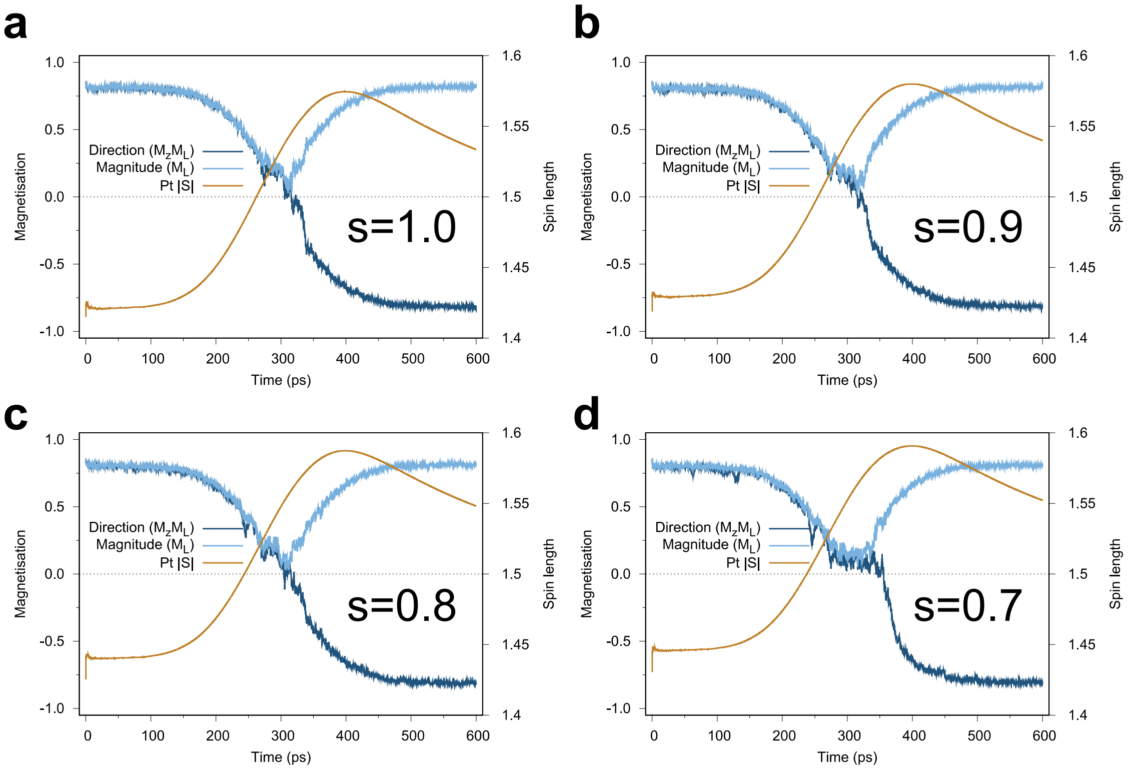

Fig. 6.2 A demonstration of the spin length changes undergone by Pt sites for a grain with $D_{\text{grain}} = 5$ nm and $H_{\text{grain}} = 5$ nm. The grains are simulated in a 300K environment, which increases via a Gaussian function to a peak of 700 K at 300 ps. The ability to switch efficiently is impacted with respect to increased disordering, as the Néel pair anisotropy interactions are reduced as disorder increases, leading to smaller uniaxial contributions at the peak temperature.

6.4 Easy-axis dispersion in disordered grains

A key property of magnetic recording media that must be kept minimised, is the dispersion of the individual grains' easy-axes. This is important, because in order to realise a fully perpendicular system with no in-plane magnetisation, the anisotropy fields must be as parallel to the z-axis as possible in order to have a clear readout signal. A primary cause for misaligned easy axes is disordering, whereby clustering of certain material species can interfere with the Fe and Pt stacking direction along z and cause diversions in the preferential uniaxial direction. The LSF model being able to model disordering has importantly been used in emulating different HAMR recording media under the effects of different levels of disordering to determine its relationship with the average easy-axis position seen across grains. By collating 229 grains of dimensions $D_{\text{grain}} \approx 6$ nm and $H_{\text{grain}} = 5$ nm with 0.5 nm spacing between them, a 200 nm by 50 nm recording medium was simulated. It is noted, that the average grain diameter will see some variance in diameter, as a random Voronoi tessellation function is used in this process. After generating the system, it is set to $T = 0$ K, while setting all initial spin positions to $\theta = 45°$ and $\phi = 0°$. The system is then allowed to relax under the LSF-LLG integrator, with damping parameter $\lambda = 0.1$, for a total of $t = 3$ ns with timestep size $\Delta t = 1 \ \times 10^{-15}$s. The result of the distributions of easy-axes is shown in figure 6.3, where it is evident, that an ordering parameter of $s = 0.4$ is almost fully aligned with the preferred easy-axis direction, while $s = 0.5$ has all grains configured with an easy-axis at the direction [001], within a 5° margin. This calculation shows, that disordering above $s = 0.5$ is already configured for a perpendicular easy-axis, with minimal in-plane contributions and thus would have no issues with producing a clear readout signal during the HAMR process. As for the grain distributions pertaining to $s < 0.5$, it is evident that a more distributed and in-plane configuration is preferred, which would heavily hinder the ability to use such systems in HAMR. It is interesting to note the rapid transition from a mostly in-plane easy axis to a mostly out-of-plane one between $s = 0.1$ and $s = 0.2$, although the large error margin in easy axes for these systems would still likely cause significant error while recording.

Overall, the easy-axis distribution calculations for grain ensembles demonstrates that using the information retrieved from these calculations, a value for $s > 0.5$ is shown to be viable in HAMR. A significant flaw of these calculations however is that it does not inform how likely it is that disordered grains switch at the intended conditions, but rather it shows how likely a grain is likely to be locked into a specific direction once influenced by a temperature pulse and write field. In addition to this, it would be useful to simulate variations in not only the grain diameter, but height as well. It is evident in practice that grains on HAMR media are not all of the same height [78].

6.5 Atomistic HAMR with Pt degrees of freedom

To fully realise the collective research presented in chapters 3, 4, and 5 of this thesis, fully atomistic HAMR simulations were done combining the LSF-LLG integrator, the Landau energies for FePt, the Néel pair anisotropy model for FePt, and the disordering calculations done for FePt systems. Firstly, grains of sizes 3 nm to 8 nm with height 5 nm were assembled with a spacing of 0.5 nm on 200 nm by 50 nm recording media. This is similar to the calculations conducted in chapter 3, although this time with both Fe and Pt degrees of freedom being simulated. It should be noted, that this first result is modelled using fully $\mathrm{L1_0}$ grains, with no disordering. A variable temperature pulse defined exactly as in the single-grain calculations of this chapter was applied in a sequential order to write a sample

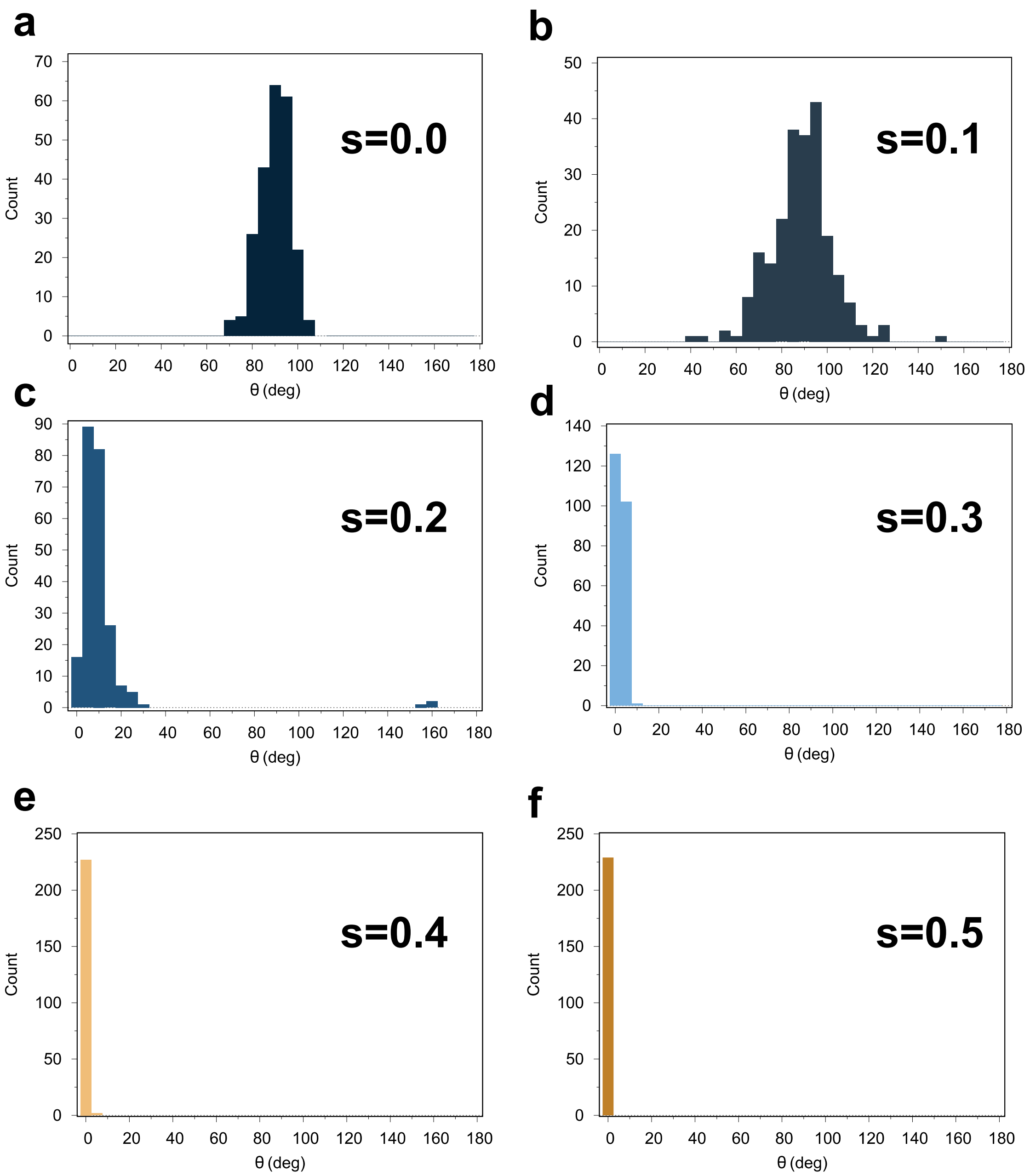

Fig. 6.3 The easy axis distributions are shown for fixed grain size $D_{\text{grain}} = 6$ nm and $H_{\text{grain}} = 5$ nm on a magnetic recording medium. The chemical order parameter s shows the simulated level of disordering present in the grains. It can be seen that at values of $s > 0.5$, a 5° tolerance from the z-axis can be obtained, while with $s < 0.5$, the easy axis dispersion quickly diverges to $\theta = 90°$.

series of bits, which switched the magnetisation state of grains via a 1T field in either the [001] or [00-1] directions. Figure 6.4 shows the culmination of the various grain sizes. It is clear that the LSF-LLG model recovers the expected bit patterns that were imprinted on the media, showing clearly the evolution of data clarity across grain sizes. For example, the 3 nm grains while containing a greater resolution per bit, they show much more areas where accidental switching has occurred, which would lead to error in attempting to read the magnetic field at a given region. Increasing the grain size to 8 nm also creates issues, whereby the increased T_{C} leads to more difficulty switching, which causes regions where it is unclear what the written bit was intended to be. Overall, the results shown for the LSF full HAMR simulation demonstrate similar trends to what was seen in chapter 3, whereby the 4 nm to 5 nm diameter grains are qualitatively the easiest to read back a bit sequence from for a fixed peak temperature.

Next, results are shown for the HAMR process with variable levels of grain disordering in figure 6.5. As a variation from the previous methodology of varying grain diameter, a fixed diameter of 6 nm and height of 5 nm was considered, with increasing levels of disordering from $s = 1.0$ down to $s = 0.7$. It can be seen that the moment some amount of disordering is added at $s = 0.9$, the bit pattern immediately ceases to form clear boundaries, and the writing process is greatly erroneous. At the $s = 0.8$ result, the bit clarity is almost non-existent, however surprisingly, some clarity is recovered in the final $s = 0.7$ system. The explanation for this is that as inherent disordering increases, counteracting the uniaxial easy-axis anisotropy energy to switch the grains becomes dramatically easier. This means, that while the earlier easy-axis dispersion result showed that the easy-axes are maintained significantly well at disorders of $s > 0.5$, the fluctuations exposed to the system erroneously cause switching to occur in unwanted grains. Referring back to the quadrilemma, This can be due to a number of factors, such as the temperature pulse affecting neighbouring regions causing spontaneous reversal of the overall grain magnetisation, or that after the data is written and the grain cools, it still has enough thermal energy to switch back to its original configuration. Regardless, this result obtained shows that even slight disordering at $s = 0.9$ causes drastic error in the writing of a sample bit pattern during HAMR.

To highlight the example discussed in the previous result, a close-up render of grains in the $s = 1.0$ and $s = 0.7$ systems is shown, whereby it is clear that a larger number of misaligned atoms exist within the grains themselves. This is denoted by the oppositely coloured spins within the grains, which shows that there is a significant amount of small clusters which are easily influenced by systematic fluctuations that are unavoidable in HAMR, which make spontaneous backswitching a definite possibility.

The LSF model shows great promise in being able to bridge the gap between what is possible to investigate theoretically using atomistic modelling for HAMR systems. The HAMR media simulated using the fully discretized FePt model have allowed for a preliminary

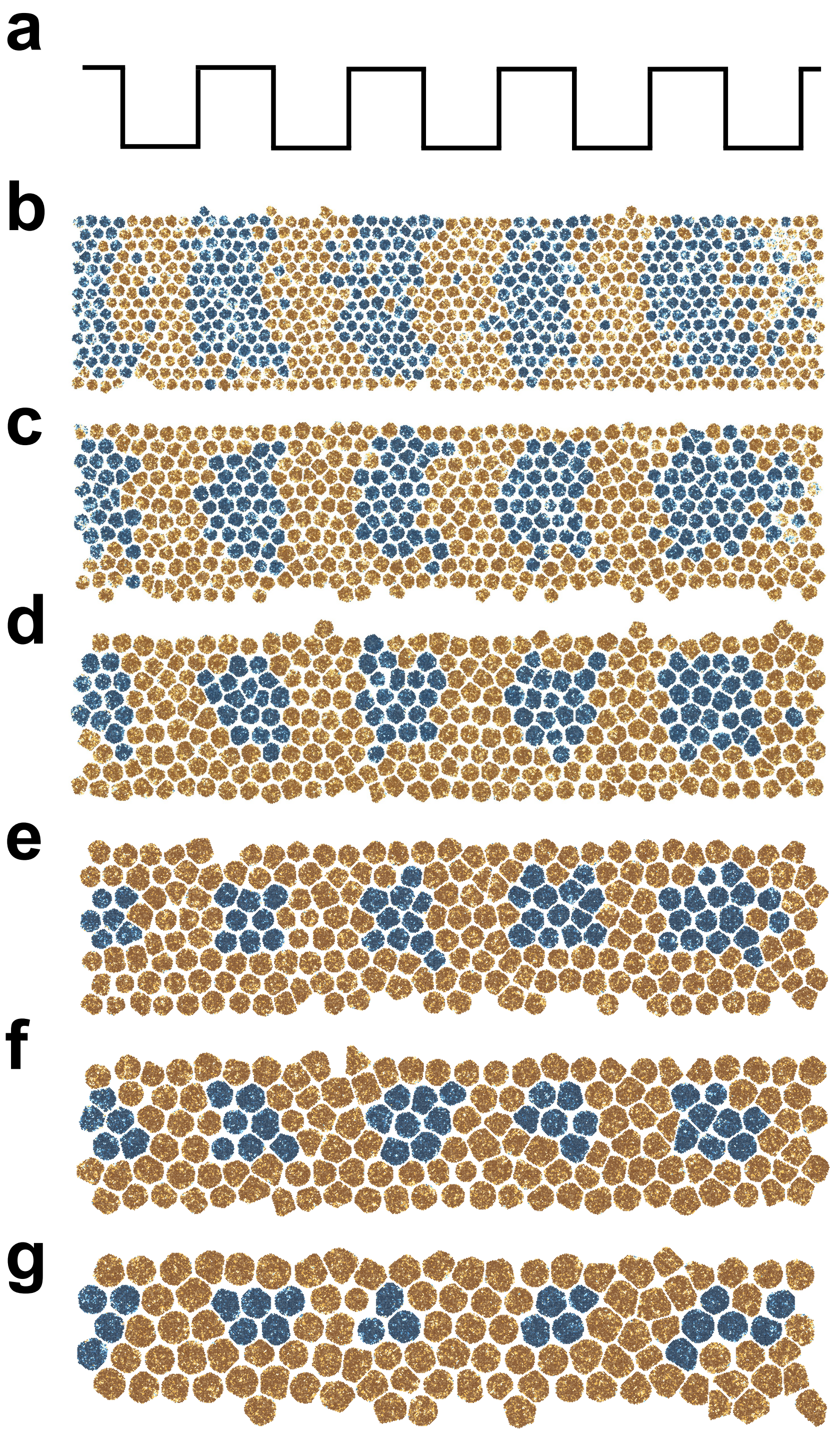

Fig. 6.4 A render showing the HAMR process for grains of fixed height 5 nm, with diameter varied from 3 nm in (b) to 8 nm in (g) in 1 nm increments. The magnetic recording trilemma is represented in these calculations, showing a clear trade-off between grain size and overall error in the definition of bits.

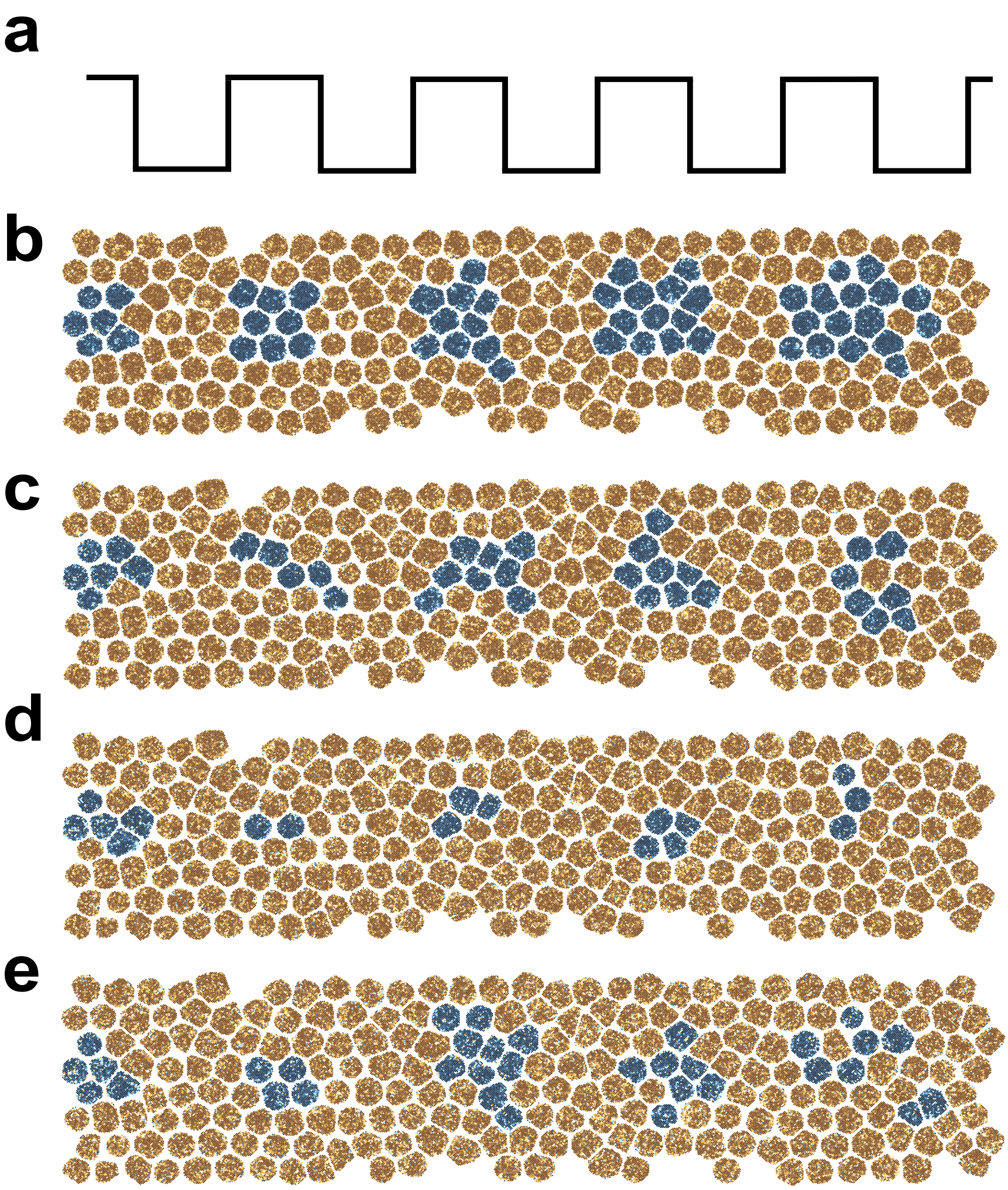

Fig. 6.5 Rendered bit pattern that is imprinted on HAMR media, with fixed grain dimensions of $D_{\text{grain}} = 6$ nm and $H_{\text{grain}} = 5$ nm. Inherent disordering is also added to the system at $s = 1.0$ in (b), $s = 0.9$ in (c), $s = 0.8$ in (d), and $s = 0.7$ in (e). It can be seen that even $s = 0.9$ creates a drastic reduction in the clarity of the bits due to a smaller energy barrier required to switch their magnetisation direction. This means that random thermal fluctuations can more easily induce unwanted reversal, leading to backswitching.

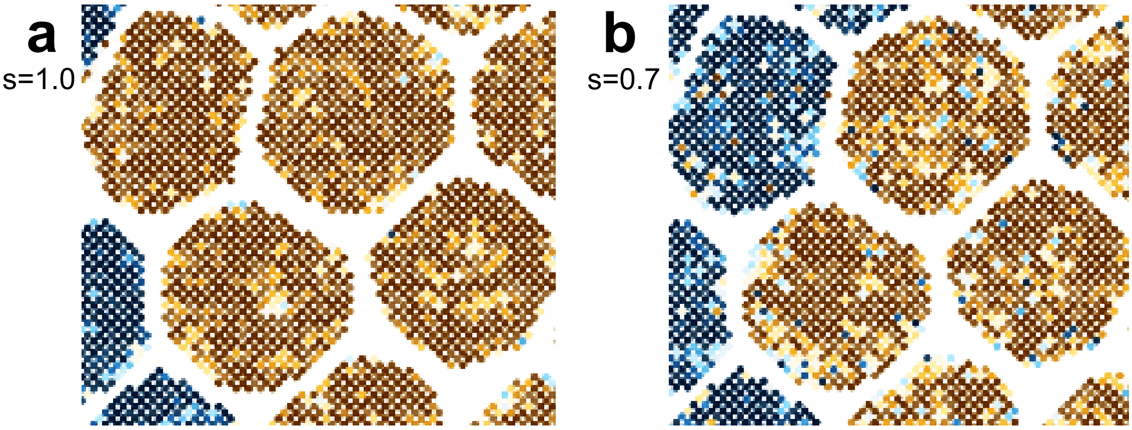

Fig. 6.6 A close up render of HAMR system with $s = 1.0$ in (a) and $s = 0.7$ in (b). The disordered grain systems create an environment which more easily accommodates for oppositely aligned spin sites, leading to more spontaneous magnetisation reversal, which significantly effects the reliability of the imprinted data being read.

investigation which used computational theoretical models as tools in understanding the nanoscale physics that govern underlying data recording processes. It is still challenging to establish the exact levels of disordering that a system can tolerate before HAMR becomes completely non-viable. For example, even in the disordered cases calculated, disordering with a different grain height might yield additional symmetries that did not manifest in the calculations shown in this chapter, yielding a different set of disordering expectations. Regardless, while the potential to investigate such issues is now possible, the results from the calculations have shown that even small deviations from $s = 1.0$ will cause significantly detrimental effects to the recording process, and thus disordering deviations should be minimised during the manufacturing process.

As an area of future work, the models implemented in this thesis would also allow for a full investigation into the composition dependence of HAMR processes, whereby moving away from the exact 50:50 ratio of Fe to Pt would most likely lead to significantly altered results. This would be an important classification to obtain, as from a practical standpoint obtaining a perfect margin of Fe and Pt is near impossible, and will naturally have some variance in the concentrations of both species.

6.6 Summary

This chapter highlighted the expectations brought on by HAMR under circumstances that were previously not greatly considered, namely inherent system disordering in FePt systems. The investigation done in this chapter successfully reproduced the adequate finite-size uniaxial anisotropy energy dependencies with respect to chemical ordering parameter s. Next, the single-grain calculations with the LSF model revealed the nature of the Pt moment length during the process of switching, which was qualitatively revealed to have a delayed reaction time when compared to the timing of the peak of the temperature pulse. The culmination of the previous chapters in this thesis has led to calculations about the effects that disordering has on the HAMR process, namely by computing the expected distribution of easy-axes in disordered grains. This was further iterated on by the results obtained for fully atomistic HAMR simulations using the LSF model, which showed conclusively that even the smallest amounts of disordering disturbs the applicability of such technologies.

7

Conclusions

Modelling the longitudinal degrees of freedom in spins is a necessity in appropriately treating moment size changes, while still enabling magnetisation calculations within a fully atomistic framework. For materials such as Pt (in FePt) and Ni, it can be concluded that the induced moment behaviour has thus far been disregarded as a fundamental degree of freedom, hindering the investigation towards the effects of disordered structures. This is especially applicable in the context of Heat Assisted Magnetic Recording (HAMR), where uncontrollable amounts of disordering can enter the manufactured recording media, and cause behaviour that was previously hard to magnify. The conclusions for each chapter are found to be the following:

Chapter 3 has highlighted the conventional atomistic treatment for FePt, and its capability to model the fully ordered $\mathrm{L1_0}$ phase via the 2-ion treatment of Pt, and the subsequent modification to the Fe parameters. The atomistic form of FePt implemented was able to appropriately reproduce the temperature-dependent anisotropy relationship seen in experimental measurements, alongside an expected calculated $T_\mathrm{C} \approx 700$ K. The T_C grain size dependence was demonstrated, showing clearly that the model reproduces qualitatively the finite-size scaling law (the law that a larger grain volume leads to a larger T_C). Additionally, larger grain sizes lead to more difficulty in the magnetic switching process, which determines the capability of a certain grain size to undergo the HAMR recording process. More specifically, all the grains with $H_\mathrm{grain} = 10$ nm showed significantly reduced chances of switching, due to the formation of more than one domain. Finally, the full HAMR calculations have shown the intricate balances brought on by the magnetic recording trilemma, however it is evident according to the results shown that grain sizes of $D_\mathrm{grain} \approx 4$ nm are certainly viable under the context of the simulated system.

Chapter 4 details the implementation of the Longitudinal Spin Fluctuations (LSF) model is shown to have been successful, as testing on Fe, Ni, Co, and Cr have retrieved the expected results. This comes with a proposed equilibrium correction of the spin length quantity, so as to ensure the material species tested have a spin length minima at $|S| = 1$. It was observed clearly that the moment size in Ni fluctuates significantly with respect to the system's exchange energy and temperature, inducing stronger longitudinal fluctuations than what is seen in a species such as Fe. This behaviour was further demonstrated in temperature dependent magnetisation calculations, whereby the increased temperatures induced longitudinal changes in Ni that were larger than that in Fe. The temperature dependent magnetisation calculations for the tested materials agree excellently with experimental results given a mandatory exchange constant adjustment, which was first discussed in longitudinal models by Ma *et al* [49]. The validity of the newly developed integrator schemes were also tested, using the Heun and fourth-order Runge-Kutta schemes which showed that the LSF-LLG converges within a reasonable amount of integration steps. Finally, the longitudinally dependent ultrafast demagnetisation dynamics of Ni were tested, showing a clear match in the trends of experimentally obtained data.

Chapter 5 shows the successful implementation of a fully atomistic FePt model via the Landau Hamiltonian to allow for Pt to gain a quantifiable induced moment. The results were able to reproduce qualitatively the induced moment nature of Pt in this system, as it can be seen in temperature dependent magnetisation calculations that the Pt spin length approximately doubles at $T = T_C^{\mathrm{FePt}}$. The validity of this result was also obtained via the longitudinal Boltzmann distributions, showing the significant moment length increase in Pt, while Fe's steep longitudinal potential well prevents drastic changes to $|S|$, and thus stays at $|S| \approx 1$. To localise the anisotropy energy calculations in this model, the Néel pair anisotropy model was successfully implemented for FePt. The fourth-order form allowed for the correct computation of the cubic symmetries observed in disordered FePt, while the second-order calculations computed a very similar anisotropy against disorder scaling relationship found in Okamoto *et al* [32].

Chapter 6 culminates the research and implementation shown in chapters 3 to 5, whereby the push for a fully localised atomistic description of FePt has allowed for calculations of the processes undergone to HAMR to be simulated using maximised atomistic degrees of freedom. The uniaxial anisotropy energy against disordering calculations show that there is no significant quantifiable difference in the anisotropy energies per functional unit between different grain sizes with respect to disorder. Interestingly, it was shown that the compressed lattice in the finite-size grain calculations of anisotropy against disorder exhibited the same behaviour identified in Staunton *et al.*, where DFT calculations reproduce the negative $E_{\mathrm{ani}}/\mathrm{f.u}$ value at $s = 0.0$ exactly as per the atomistic calculations done in this chapter. Finally, it can be seen that fully atomistic HAMR under the LSF model was successfully implemented, resulting in the reproduction within expectations of a custom bit pattern on the simulated magnetic recording media. To further develop the influence disordering has on these results, the calculations that fix grain diameter at $D_{\text{grain}} = 6$ nm and vary disordering show a clear loss of recorded data due to an overall loss of uniaxial anisotropy in the grains. Additionally, the easy-axis dispersion results show that for grains of $D_{\text{grain}} = 6$ nm, a value of $s > 0.5$ guarantees easy-axis dispersion to be within 5° of $\theta = 0^\circ$.

Overall, the results of this thesis have shown the viable implementation of the LSF model, which now allows for more detailed customisation in the types of systems that can be simulated undergoing HAMR. This aims to significantly aid the research process behind this technology, as the physical expectations of the model have shown to agree with what is expected to occur in experimental cases. The atomistic simulation of HAMR conducted in this thesis has the ability to better inform the research and development decisions of the future evolution of HAMR.

7.1 Further work

7.1.1 Split sampling scheme in the longitudinal Monte-Carlo

One of the main challenges in the implementation of the LSF-MC integrator scheme was its computational efficiency: it currently only achieves ergodicity when combining transverse and longitudinal sampling spaces, and further to this samples using a uniform distribution mechanism. This was also discussed in Pan *et al.* where it is mentioned that a further advancement is required in the implementation of such a scheme to achieve fully split transverse and longitudinal moves [31]. This would require a reworking of the probability evaluation function, and the overall architecture of the sampling mechanism.

Once achieved, the efficiency of the LSF-MC can be greatly improved. Firstly, the sampling width in both longitudinal and transverse changes can be tuned independently, thus the system would be able to reach equilibrium at independent rates. Secondly, there would be a much faster equilibration time overall, as the move from uniform to a Gaussian sampling process would eliminate a significant amount of rejected moves especially at low temperatures where spin moves are less likely to be taken. Being able to separate the equilibration times between both moves in general would be valuable to research and investigate.

7.1.2 Modelling further induced moments longitudinally

The LSF model implemented in this thesis (specifically in the context of chapter 4) paves the way for a significantly large number of future applications with regards to additional materials. In particular, elements or alloys with clear induced moment behaviour would be interesting to look at, as this model would be able to appropriately treat the instantaneous moment size via a custom Landau Hamiltonian. A current constraint to the currently implemented model is that it requires *a priori* knowledge of the simulated system to be able to determine the effective Landau parameters and exchange adjustment factor. By conducting research on further systems, a larger catalogue of understanding can be built for usage in future research. The exact dependence on the exchange correction factor introduced is also something to be investigated further, as no clear correlation was found with how large this value should be with respect to system parameters.

7.1.3 Composition dependent behaviour of HAMR systems

Chapters 5 and 6 focus specifically on the implementation of modelling a more discretised version of atomistic FePt, in order to pave the way for calculations relating to imperfect lattice structures. As a further to the calculations done in these chapters, a natural extension to this would be to look at the composition dependence of FePt, as this may greatly vary during the manufacturing process [24, 114]. The LSF model provides enough discretisation for such an investigation to take place, which would simply be a choice of swapping out more Fe or Pt lattice sites with the opposing species to diverge from the $50:50$ ratio seen in this thesis. HAMR research in general shows an interest in being able to compute the optimal material ratios for given alloys, and thus this would be a valuable investigation to conduct [114]. Additionally, to investigate the complete symmetries of the generated structures, the fourth-order form of the Néel pair anisotropy model would be valuable to investigate with regards to the fourth-order coefficient. Determining the calculation for this would allow its usage in larger scale atomistic HAMR simulations, whereby both uniaxial, and (although small) cubic contributions can be investigated with respect to each quantity.

7.1.4 Atomistic LSF-LLB

The discussions around transverse and longitudinal damping remain to be resolved in future work. In order to appropriately implement different damping parameters for both processes, the LSF-LLG equation of motion would revert back to the LLB one [65], from where the Heun or Runge-Kutta fourth-order solvers can be used to complete the integration scheme.

LSF dynamics can be included via the addition of the Landau Hamiltonian. Such a model would allow for a more intimate investigation into the relationship between $\lambda_{\text{longitudinal}}$ and $\lambda_{\text{transverse}}$, which would naturally lead into more thorough investigations into ultrafast demagnetisation calculations. As a further extension, the LSF-LLB integrator can then be extended to alloys such as FePt for magnetic recording research, whereby a different set of material damping parameters for both move types may be allocated. Such a model would in theory be able to replicate to a material specific resolution what is seen in Yamamoto *et al* [116].

References

[1] Valdemar Poulsen. Method of recording and reproducing sounds or signals., November 13 1900. US Patent 661,619.

[2] Geoffrey Bate. Magnetic recording materials since 1975. *Journal of Magnetism and Magnetic Materials*, 100(1):413–424, 1991.

[3] M. L. Lesser and J. W. Haanstra. The ramac data-processing machine: system organization of the ibm 305. In *Papers and Discussions Presented at the December 10-12, 1956, Eastern Joint Computer Conference: New Developments in Computers*, AIEE-IRE '56 (Eastern), page 139–146, New York, NY, USA, 1956. Association for Computing Machinery.

[4] Roger Wood. Future hard disk drive systems. *Journal of Magnetism and Magnetic Materials*, 321(6):555 – 561, 2009. Current Perspectives: Perpendicular Recording.

[5] Gordon E. Moore. Cramming more components onto integrated circuits, reprinted from electronics, volume 38, number 8, april 19, 1965, pp.114 ff. *IEEE Solid-State Circuits Society Newsletter*, 11(3):33–35, 2006.

[6] John F Gantz, David Reinsel, and John Rydning. The us datasphere: Consumers flocking to cloud. *White Paper*, 2019.

[7] Rekha Nachiappan, Bahman Javadi, Rodrigo N. Calheiros, and Kenan M. Matawie. Cloud storage reliability for big data applications: A state of the art survey. *Journal of Network and Computer Applications*, 97:35–47, 2017.

[8] Victor Chang and Gary Wills. A model to compare cloud and non-cloud storage of big data. *Future Generation Computer Systems*, 57:56–76, 2016.

[9] H J Richter. The transition from longitudinal to perpendicular recording. *Journal of Physics D: Applied Physics*, 40(9):R149, Apr 2007.

[10] R.H. Victora and X. Shen. Exchange coupled composite media for perpendicular magnetic recording. *IEEE Transactions on Magnetics*, 41(10):2828–2833, 2005.

[11] Shun ichi Iwasaki. Perpendicular magnetic recording—its development and realization. *Journal of Magnetism and Magnetic Materials*, 324(3):244–247, 2012. Selected papers of the 9th Perpendicular Magnetic Recording Conference(PMRC 2010).

[12] Y. Sonobe, K.K. Tham, T. Umezawa, C. Takasu, J.A. Dumaya, and P.Y. Leo. Effect of continuous layer in cgc perpendicular recording media. *Journal of Magnetism and Magnetic Materials*, 303(2):292–295, 2006. The 6th International Symposium on Physics of Magnetic Materials.

[13] H. J. Richter, A. Lyberatos, U. Nowak, R. F. L. Evans, and R. W. Chantrell. The thermodynamic limits of magnetic recording. *Journal of Applied Physics*, 111(3):033909, 2012.

[14] V Koji Matsumoto V Akihiro Inomata and V Shin-ya Hasegawa. Thermally assisted magnetic recording. *Fujitsu Sci. Tech. J*, 42(1):158–167, 2006.

[15] M.T. Kief and R.H. Victora. Materials for heat-assisted magnetic recording. *MRS Bulletin*, 43(2):87–92, 2018.

[16] Dieter Weller, Gregory Parker, Oleksandr Mosendz, Andreas Lyberatos, Dmitriy Mitin, Nataliia Y. Safonova, and Manfred Albrecht. Review article: Fept heat assisted magnetic recording media. *Journal of Vacuum Science & Technology B*, 34(6):060801, 2016.

[17] Samarth Bhargava and Eli Yablonovitch. Lowering hamr near-field transducer temperature via inverse electromagnetic design. *IEEE Transactions on Magnetics*, 51(4):1–7, 2015.

[18] Simon Greaves, Yasushi Kanai, and Hiroaki Muraoka. Magnetization switching in energy assisted recording. *IEEE Transactions on Magnetics*, 48(5):1794–1800, 2012.

[19] R. H. Victora and Sumei Wang. Simulation of expected areal density gain for heat-assisted magnetic recording relative to other advanced recording schemes. *IEEE Transactions on Magnetics*, 51(11):1–7, 2015.

[20] Eric Roddick, Mark Kief, and Akihiko Takeo. A new advanced storage research consortium hdd technology roadmap. In *2022 IEEE 33rd Magnetic Recording Conference (TMRC)*, pages 1–2, 2022.

[21] Mara Strungaru, Sergiu Ruta, Richard F.L. Evans, and Roy W. Chantrell. Model of magnetic damping and anisotropy at elevated temperatures: Application to granular fept films. *Physical Review Applied*, 14:014077, Jul 2020.

[22] Zengyuan Liu, Pin-Wei Huang, Ganping Ju, and R. H. Victora. Thermal switching probability distribution of L10 FePt for heat assisted magnetic recording. *Applied Physics Letters*, 110(18):182405, 05 2017.

[23] Xiaobin Wang, Kaizhong Gao, Hua Zhou, Amit Itagi, Mike Seigler, and Edward Gage. Hamr recording limitations and extendibility. *IEEE Transactions on Magnetics*, 49(2):686–692, 2013.

[24] D. C. Berry and K. Barmak. Effect of alloy composition on the thermodynamic and kinetic parameters of the A1 to L1 transformation in FePt, FeNiPt, and FeCuPt films. *Journal of Applied Physics*, 102(2):024912, 07 2007.

[25] R. F. L. Evans and W. J. Fan. Atomistic simulation of sub-nanosecond non-equilibrium field cooling processes for magnetic data storage applications. *Applied Physics Letters*, 105(19):192405, 11 2014.

[26] W Pantasri, A Meo, R W Chantrell, P Chureemart, and J Chureemart. Granular micromagnetic hamr model: investigation of damping dependence and parametric optimization for high performance. *Journal of Physics D: Applied Physics*, 57(8):085001, Dec 2023.

[27] A. Meo, W. Pantasri, W. Daeng-am, S. E. Rannala, S. I. Ruta, R. W. Chantrell, P. Chureemart, and J. Chureemart. Magnetization dynamics of granular heat-assisted magnetic recording media by means of a multiscale model. *Physical Review B*, 102:174419, Nov 2020.

[28] R F L Evans, W J Fan, P Chureemart, T A Ostler, M O A Ellis, and R W Chantrell. Atomistic spin model simulations of magnetic nanomaterials. *Journal of Physics: Condensed Matter*, 26(10):103202, 2014.

[29] Serban Lepadatu, George Mckenzie, Tim Mercer, Callum Robert MacKinnon, and Philip Raymond Bissell. Computation of magnetization, exchange stiffness, anisotropy, and susceptibilities in large-scale systems using gpu-accelerated atomistic parallel monte carlo algorithms. *Journal of Magnetism and Magnetic Materials*, 540:168460, 2021.

[30] O. N Mryasov, U Nowak, K. Y Guslienko, and R. W Chantrell. Temperature-dependent magnetic properties of FePt: Effective spin hamiltonian model. *Europhysics Letters (EPL)*, 69(5):805–811, Mar 2005.

[31] Fan Pan, Jonathan Chico, Anna Delin, Anders Bergman, and Lars Bergqvist. Extended spin model in atomistic simulations of alloys. *Physical Review B*, 95:184432, May 2017.

[32] S. Okamoto, N. Kikuchi, O. Kitakami, T. Miyazaki, Y. Shimada, and K. Fukamichi. Chemical-order-dependent magnetic anisotropy and exchange stiffness constant of fept (001) epitaxial films. *Physical Review B*, 66:024413, Jul 2002.

[33] Xueyang Li, Hongyu Yu, Feng Lou, Junsheng Feng, Myung-Hwan Whangbo, and Hongjun Xiang. Spin hamiltonians in magnets: Theories and computations. *Molecules*, 26(4), 2021.

[34] Sabine Wurmehl, Gerhard H. Fecher, Hem C. Kandpal, Vadim Ksenofontov, Claudia Felser, Hong-Ji Lin, and Jonder Morais. Geometric, electronic, and magnetic structure of co_2FeSi: Curie temperature and magnetic moment measurements and calculations. *Physical Review B*, 72:184434, Nov 2005.

[35] F. Wilhelm, P. Poulopoulos, G. Ceballos, H. Wende, K. Baberschke, P. Srivastava, D. Benea, H. Ebert, M. Angelakeris, N. K. Flevaris, D. Niarchos, A. Rogalev, and N. B. Brookes. Layer-resolved magnetic moments in Ni/Pt multilayers. *Physical Review Letters*, 85:413–416, Jul 2000.

[36] Stephan Geprägs, Sibylle Meyer, Stephan Altmannshofer, Matthias Opel, Fabrice Wilhelm, Andrei Rogalev, Rudolf Gross, and Sebastian T. B. Goennenwein. Investigation of induced Pt magnetic polarization in Pt/Y3Fe5O12 bilayers. *Applied Physics Letters*, 101(26):262407, 12 2012.

[37] VAMPIRE software package available from https://vampire.york.ac.uk/. 2024.

[38] Stephen Blundell. *Magnetism in condensed matter*. OUP Oxford, 2001.

[39] D. A. Garanin, R. Schilling, and A. Scala. Saddle index properties, singular topology, and its relation to thermodynamic singularities for a ϕ^4 mean-field model. *Physical Review E*, 70:036125, Sep 2004.

[40] D. A. Garanin. Self-consistent gaussian approximation for classical spin systems: Thermodynamics. *Physical Review B*, 53:11593–11605, May 1996.

[41] Sayani Majumdar, Himadri Majumdar, and Ronald Österbacka. Organic spintronics. 01 2010.

[42] David Jiles. *Introduction to magnetism and magnetic materials*. CRC press, 2015.

[43] Helmut Kronmüller. General micromagnetic theory and applications. pages 1–43, 2019.

[44] R Yanes and O Chubykalo-Fesenko. Modelling of the influence of the néel surface anisotropy on the enhancement of the magnetic anisotropy in co nanoparticle. *Journal of Physics D: Applied Physics*, 42(5):055013, Feb 2009.

[45] B Skubic, J Hellsvik, L Nordström, and O Eriksson. A method for atomistic spin dynamics simulations: implementation and examples. *Journal of Physics: Condensed Matter*, 20(31):315203, Jul 2008.

[46] Michael Uhl and Jürgen Kübler. Exchange-coupled spin-fluctuation theory: Application to fe, co, and ni. *Physical Review Letters*, 77:334–337, Jul 1996.

[47] N. M. Rosengaard and Börje Johansson. Finite-temperature study of itinerant ferromagnetism in fe, co, and ni. *Physical Review B*, 55:14975–14986, Jun 1997.

[48] A. L. Wysocki, J. K. Glasbrenner, and K. D. Belashchenko. Thermodynamics of itinerant magnets in a classical spin-fluctuation model. *Physical Review B*, 78:184419, Nov 2008.

[49] Pui-Wai Ma and S. L. Dudarev. Longitudinal magnetic fluctuations in langevin spin dynamics. *Physical Review B*, 86:054416, Aug 2012.

[50] Matthew O. A. Ellis, Mario Galante, and Stefano Sanvito. Role of longitudinal fluctuations in $L1_0$ fept. *Physical Review B*, 100:214434, Dec 2019.

[51] K Schwarz and P Mohn. Itinerant metamagnetism in yco2. *Journal of Physics F: Metal Physics*, 14(7):L129, Jul 1984.

[52] P. H. Dederichs, S. Blügel, R. Zeller, and H. Akai. Ground states of constrained systems: Application to cerium impurities. *Physical Review Letters*, 53:2512–2515, Dec 1984.

[53] P.M. Derlet and S.L. Dudarev. Million-atom molecular dynamics simulations of magnetic iron. *Progress in Materials Science*, 52(2):299–318, 2007. Modelling electrons and atoms for materials science.

[54] Lev Davidovich Landau and Evgenii Mikhailovich Lifshitz. *On the theory of the dispersion of magnetic permeability in ferromagnetic bodies*. Physikalische zeitschrift der Sowjetunion. 8, 153, 1935.

[55] Thomas L. Gilbert. A lagrangian formulation of the gyromagnetic equation of the magnetization field. *Physical Review D*, 100:1243, 1955.

[56] José Luis García-Palacios and Francisco J. Lázaro. Langevin-dynamics study of the dynamical properties of small magnetic particles. *Physical Review B*, 58:14937–14958, Dec 1998.

[57] Gideon P. Müller, Markus Hoffmann, Constantin Dißelkamp, Daniel Schürhoff, Stefanos Mavros, Moritz Sallermann, Nikolai S. Kiselev, Hannes Jónsson, and Stefan Blügel. Spirit: Multifunctional framework for atomistic spin simulations. *Physical Review B*, 99:224414, Jun 2019.

[58] W. Brown. Thermal fluctuation of fine ferromagnetic particles. *IEEE Transactions on Magnetics*, 15(5):1196–1208, 1979.

[59] A Lyberatos, D V Berkov, and R W Chantrell. A method for the numerical simulation of the thermal magnetization fluctuations in micromagnetics. *Journal of Physics: Condensed Matter*, 5(47):8911, Nov 1993.

[60] U. Atxitia, O. Chubykalo-Fesenko, R. W. Chantrell, U. Nowak, and A. Rebei. Ultrafast spin dynamics: The effect of colored noise. *Physical Review Letters*, 102:057203, Feb 2009.

[61] W. C. Kerr and A. J. Graham. Generalized phase space version of langevin equations and associated fokker-planck equations. *The European Physical Journal B - Condensed Matter and Complex Systems*, 15(2):305–311, May 2000.

[62] O. Chubykalo, R. Smirnov-Rueda, J.M. Gonzalez, M.A. Wongsam, R.W. Chantrell, and U. Nowak. Brownian dynamics approach to interacting magnetic moments. *Journal of Magnetism and Magnetic Materials*, 266(1):28–35, 2003. Proceedings of the 4th International Conference on Fine Particle Magnetism (ICFPM).

[63] Serban Lepadatu. Accelerating micromagnetic and atomistic simulations using multiple gpus. *Journal of Applied Physics*, 134(16):163903, 10 2023.

[64] D. A. Garanin. Fokker-planck and landau-lifshitz-bloch equations for classical ferromagnets. *Physical Review B*, 55:3050–3057, Feb 1997.

[65] R. F. L. Evans, D. Hinzke, U. Atxitia, U. Nowak, R. W. Chantrell, and O. Chubykalo-Fesenko. Stochastic form of the landau-lifshitz-bloch equation. *Physical Review B*, 85:014433, Jan 2012.

[66] U. Atxitia, P. Nieves, and O. Chubykalo-Fesenko. Landau-lifshitz-bloch equation for ferrimagnetic materials. *Physical Review B*, 86:104414, Sep 2012.

[67] U Atxitia, D Hinzke, and U Nowak. Fundamentals and applications of the landau–lifshitz–bloch equation. *Journal of Physics D: Applied Physics*, 50(3):033003, Dec 2016.

[68] Denise Hinzke, Ulrich Nowak, and DA Garanin. Uniform susceptibility of classical antiferromagnets in one and two dimensions in a magnetic field. *The European Physical Journal B-Condensed Matter and Complex Systems*, 16:435–438, 2000.

[69] R. Hornreich and S. Shtrikman. Susceptibility-derived sublattice magnetization in antiferromagnets. *Physical Review*, 159:408–410, Jul 1967.

[70] Yukiko Kubota, Yingguo Peng, Yinfeng Ding, Eric K. C. Chang, Li Gao, Florin Zavaliche, Timothy J. Klemmer, Sha Zhu, Xiaobin Zhu, Pin-Wei Huang, Alexander Q. Wu, Hassib Amini, Steven Granz, Tim Rausch, Chris J. Rea, Jiaoming Qiu, Huaqing Yin, Mike A. Seigler, Yonghua Chen, Ganping Ju, and Jan-Ulrich Thiele. Heat-assisted magnetic recording's extensibility to high linear and areal density. *IEEE Transactions on Magnetics*, 54(11):1–6, 2018.

[71] J.-U. Thiele, K. R. Coffey, M. F. Toney, J. A. Hedstrom, and A. J. Kellock. Temperature dependent magnetic properties of highly chemically ordered fe55xnixpt45l10 films. *Journal of Applied Physics*, 91(10):6595–6600, 2002.

[72] R. F. L. Evans, R. W. Chantrell, U. Nowak, A. Lyberatos, and H.-J. Richter. Thermally induced error: Density limit for magnetic data storage. *Applied Physics Letters*, 100(10):102402, 2012.

[73] M. Strungaru, B.T. Nguyen, K. Yuanmae, R.F.L. Evans, R.W. Chantrell, P. Chureemart, and J. Chureemart. Hamr switching dynamics and the magnetic recording quadrilemma. *Journal of Magnetism and Magnetic Materials*, 564:170041, 2022.

[74] P. M. Marcus and V. L. Moruzzi. Stoner model of ferromagnetism and total-energy band theory. *Physical Review B*, 38:6949–6953, Oct 1988.

[75] Gereon Meyer and Jan-Ulrich Thiele. Effective electron-density dependence of the magnetocrystalline anisotropy in highly chemically ordered pseudobinary $(\mathrm{Fe}_{1-x}\mathrm{Mn}_x)_{50}\mathrm{pt}_{50}$ $l1_0$ alloys. *Physical Review B*, 73:214438, Jun 2006.

[76] L. Szunyogh, L. Udvardi, J. Jackson, U. Nowak, and R. Chantrell. Atomistic spin model based on a spin-cluster expansion technique: Application to the irmn_3/co interface. *Physical Review B*, 83:024401, Jan 2011.

[77] Bing Zhou, B. S. D. Ch. S. Varaprasad, Zhengkun Dai, David E. Laughlin, and Jian-Gang Zhu. The effect of adding a magnetic oxide in the grain boundaries of hamr media. *Applied Physics Letters*, 113(8):082401, 08 2018.

[78] Bing Zhou, B. S. D. C. S. Varaprasad, Enbo Zhang, David E. Laughlin, and Jian-Gang Zhu. Microstructure analysis on size distribution during film growth in hamr media. *IEEE Transactions on Magnetics*, 54(11):1–4, 2018.

[79] P. Asselin, R. F. L. Evans, J. Barker, R. W. Chantrell, R. Yanes, O. Chubykalo-Fesenko, D. Hinzke, and U. Nowak. Constrained monte carlo method and calculation of the temperature dependence of magnetic anisotropy. *Physical Review B*, 82:054415, Aug 2010.

[80] R. F. L. Evans, U. Atxitia, and R. W. Chantrell. Quantitative simulation of temperature-dependent magnetization dynamics and equilibrium properties of elemental ferromagnets. *Physical Review B*, 91:144425, Apr 2015.

[81] H.B. Callen and E. Callen. The present status of the temperature dependence of magnetocrystalline anisotropy, and the l(l+1)2 power law. *Journal of Physics and Chemistry of Solids*, 27(8):1271 – 1285, 1966.

[82] J. Waters, D. Kramer, T.J. Sluckin, and O. Hovorka. Resolving anomalies in the critical exponents of FePt using finite-size scaling in magnetic fields. *Physical Review Applied*, 11:024028, Feb 2019.

[83] Binh Thanh Nguyen, Sergiu Ruta, Ondrej Hovorka, Richard. F. L. Evans, and Roy. W. Chantrell. Influence of the Finite-size Effects on the Curie Temperature of L10-FePt. *arXiv e-prints*, page arXiv:2207.11831, July 2022.

[84] M. O. A. Ellis and R. W. Chantrell. Switching times of nanoscale FePt: Finite size effects on the linear reversal mechanism. *Applied Physics Letters*, 106(16):162407, 04 2015.

[85] O. Hovorka, S. Devos, Q. Coopman, W. J. Fan, C. J. Aas, R. F. L. Evans, Xi Chen, G. Ju, and R. W. Chantrell. The Curie temperature distribution of FePt granular magnetic recording media. *Applied Physics Letters*, 101(5):052406, 08 2012.

[86] A. Lyberatos, D. Weller, G. J. Parker, and B. C. Stipe. Size dependence of the Curie temperature of L1o-FePt nanoparticles. *Journal of Applied Physics*, 112(11):113915, 12 2012.

[87] Jian-Gang Zhu and Yu Yan. Incoherent magnetic switching of l1 fept grains. *IEEE Transactions on Magnetics*, 57(3):1–9, 2021.

[88] J. Wang, H. Sepehri-Amin, Y.K. Takahashi, S. Okamoto, S. Kasai, J.Y. Kim, T. Schrefl, and K. Hono. Magnetization reversal of fept based exchange coupled composite media. *Acta Materialia*, 111:47–55, 2016.

[89] Razvan-V. Ababei, Matthew O. A. Ellis, Richard F. L. Evans, and Roy W. Chantrell. Anomalous damping dependence of the switching time in fe/fept bilayer recording media. *Physical Review B*, 99:024427, Jan 2019.

[90] Jung-Wei Liao, Unai Atxitia, Richard F. L. Evans, Roy W. Chantrell, and Chih-Huang Lai. Atomistic modeling of magnetization reversal modes in $l1_0$ fept nanodots with magnetically soft edges. *Physical Review B*, 90:174415, Nov 2014.

[91] Kun Xue and R. H. Victora. Dependence of hamr transition curvature on bit length. *IEEE Transactions on Magnetics*, 58(2):1–5, 2022.

[92] Oliver Gutfleisch, Matthew A. Willard, Ekkes Brück, Christina H. Chen, S. G. Sankar, and J. Ping Liu. Magnetic materials and devices for the 21st century: Stronger, lighter, and more energy efficient. *Advanced Materials*, 23(7):821–842, 2011.

[93] Liang Pan and David B Bogy. Heat-assisted magnetic recording. *Nature Photonics*, 3(4):189–190, 2009.

[94] Ganping Ju, Yingguo Peng, Eric K. C. Chang, Yinfeng Ding, Alexander Q. Wu, Xiaobin Zhu, Yukiko Kubota, Timothy J. Klemmer, Hassib Amini, Li Gao, Zhaohui Fan, Tim Rausch, Pradeep Subedi, Minjie Ma, Sangita Kalarickal, Chris J. Rea, Dimitar V. Dimitrov, Pin-Wei Huang, Kangkang Wang, Xi Chen, Chubing Peng, Weibin Chen, John W. Dykes, Mike A. Seigler, Edward C. Gage, Roy Chantrell, and Jan-Ulrich Thiele. High density heat-assisted magnetic recording media and advanced characterization—progress and challenges. *IEEE Transactions on Magnetics*, 51(11):1–9, 2015.

[95] Sergii Khmelevskyi and Peter Mohn. First-principle based simulations of longitudinal spin-fluctuations in metals and integration in classical space with variable spin amplitude. *AIP Advances*, 8(10), 10 2018. 101422.

[96] Sergii Khmelevskyi and Peter Mohn. Longitudinal fluctuations of co spin moments and their impact on the curie temperature of the heusler alloy co2fesi. *Journal of Magnetism and Magnetic Materials*, 560:169615, 2022.

[97] A. V. Ruban, S. Khmelevskyi, P. Mohn, and B. Johansson. Temperature-induced longitudinal spin fluctuations in fe and ni. *Physical Review B*, 75:054402, Feb 2007.

[98] A. Romeo, G. Finocchio, M. Carpentieri, L. Torres, G. Consolo, and B. Azzerboni. A numerical solution of the magnetization reversal modeling in a permalloy thin film using fifth order runge–kutta method with adaptive step size control. *Physica B: Condensed Matter*, 403(2):464–468, 2008.

[99] D. Böttcher, A. Ernst, and J. Henk. Temperature-dependent heisenberg exchange coupling constants from linking electronic-structure calculations and monte carlo simulations. *Journal of Magnetism and Magnetic Materials*, 324(4):610–615, 2012.

[100] A. Maghraoui, F. Fras, M. Vomir, Y. Brelet, V. Halté, J. Y. Bigot, and M. Barthelemy. Role of intersublattice exchange interaction in ultrafast longitudinal and transverse magnetization dynamics in permalloy. *Physical Review B*, 107:134424, Apr 2023.

[101] SI Anisimov, BL Kapeliovich, TL Perelman, et al. Electron emission from metal surfaces exposed to ultrashort laser pulses. *Journal of Experimental and Theoretical Physics*, 66(2):375–377, 1974.

[102] Zhibin Lin, Leonid V. Zhigilei, and Vittorio Celli. Electron-phonon coupling and electron heat capacity of metals under conditions of strong electron-phonon nonequilibrium. *Physical Review B*, 77:075133, Feb 2008.

[103] P. Muth. E. p. wohlfarth (ed.). ferromagnetic materials, vol. 2. north-holland publ. co. amsterdam 1980 592 seiten. *Kristall und Technik*, 16(1):127–127, 1981.

[104] Eric Fawcett. Spin-density-wave antiferromagnetism in chromium. *Reviews of Modern Physics*, 60:209–283, Jan 1988.

[105] Alexander B. Shick and Oleg N. Mryasov. Coulomb correlations and magnetic anisotropy in ordered $L1_0$ copt and fept alloys. *Physical Review B*, 67:172407, May 2003.

[106] Sarah Jenkins, Roy. W. Chantrell, and Richard F. L. Evans. Atomistic simulations of the magnetic properties of $\mathrm{ir}_x\mathrm{mn}_{1-x}$ alloys. *Physical Review Materials*, 5:034406, Mar 2021.

[107] Binh Nguyen. *Finite-size and surface effects in iron platinum nanograins for applications in heat-assisted magnetic recording media.* PhD thesis, University of York, 2022.

[108] P. Nieves, J. Tranchida, S. Nikolov, A. Fraile, and D. Legut. Atomistic simulations of magnetoelastic effects on sound velocity. *Physical Review B*, 105:134430, Apr 2022.

[109] L. Neél. Magnetic surface anisotropy and superlattice formation by orientation. *Journal de Physique et Le Radium*, 15, 1954.

[110] Till Burkert, Olle Eriksson, Peter James, Sergei I. Simak, Börje Johansson, and Lars Nordström. Calculation of uniaxial magnetic anisotropy energy of tetragonal and trigonal fe, co, and ni. *Physical Review B*, 69:104426, Mar 2004.

[111] M. Wolloch, D. Suess, and P. Mohn. Influence of antisite defects and stacking faults on the magnetocrystalline anisotropy of fept. *Physical Review B*, 96:104408, Sep 2017.

[112] C. Aas, Laszlo Szunyogh, Jingsheng Chen, and Roy Chantrell. Magnetic anisotropy of fept: Effect of lattice distortion and chemical disorder. *Applied Physics Letters*, 99, 08 2011.

[113] J B Staunton, S Ostanin, S S A Razee, B Gyorffy, L Szunyogh, B Ginatempo, and Ezio Bruno. Long-range chemical order effects upon the magnetic anisotropy of fept alloys from an ab initio electronic structure theory. *Journal of Physics: Condensed Matter*, 16(48):S5623, Nov 2004.

[114] Katayun Barmak, Bincheng Wang, Andrew T. Jesanis, David C. Berry, and Jeffrey M. Rickman. L1 $_0$ fept: Ordering, anisotropy constant and their relation to film composition. *IEEE Transactions on Magnetics*, 49(7):3284–3291, 2013.

[115] A Meo, P Chureemart, R W Chantrell, and J Chureemart. The role of interfacial intermixing on hamr dynamics in bilayer media. *Journal of Physics: Condensed Matter*, 34(46):465801, Sep 2022.

[116] Kohei Yamamoto, Yuya Kubota, Motohiro Suzuki, Yasuyuki Hirata, Karel Carva, Marco Berritta, Kou Takubo, Yohei Uemura, Ryo Fukaya, Kenta Tanaka, Wataru Nishimura, Takuo Ohkochi, Tetsuo Katayama, Tadashi Togashi, Kenji Tamasaku, Makina Yabashi, Yoshihito Tanaka, Takeshi Seki, Koki Takanashi, Peter M Oppeneer, and Hiroki Wadati. Ultrafast demagnetization of pt magnetic moment in l10-fept probed by magnetic circular dichroism at a hard x-ray free electron laser. *New Journal of Physics*, 21(12):123010, Dec 2019.